Title
Exploring the density of Earth’s interior: resolvability and constraints from normal modes

Author
Robson, Alexander

Publication Date
2020

Peer reviewed|Thesis/dissertation

Exploring the density of Earth's interior: resolvability and constraints from normal modes

By

Alexander J. S. Robson

A dissertation submitted in partial satisfaction of the

Requirements for the degree of

Doctor of Philosophy

In

Earth and Planetary Science

In the

Graduate Division

Of the

University of California, Berkeley

Committee in charge:

Professor Barbara Romanowicz, Chair
Professor Harriet Lau
Professor Michael Zaletel
Professor Nicholas Swanson-Hysell

Fall 2020

Abstract

Exploring the density of Earth's interior: resolvability and constraints from normal modes

by

Alexander J. S. Robson

Doctor of Philosophy in Earth and Planetary Science

University of California, Berkeley

Professor Barbara Romanowicz, Chair

Mapping Earth's density structure is crucial for understanding how our planet, and others like it form and evolve. When accompanied by existing images of seismic wave-speed structure, and inferences about possible compositions and pressure-temperature conditions, density constraints can help to reveal some of the most fundamental properties of Earth's interior. However, despite major advances in the resolution of seismic velocity structure, and a growing bank of geochemical and experimental reference points, the density structure of the Earth remains comparatively poorly constrained.

Estimates on Earth's radial (depth dependent, or "1D") structure have remained much the same as that proposed nearly 40 years ago, despite significant improvements in computational resources and a much larger catalogue of geophysical data. We map onto this radial structure lateral (or "3D") heterogeneity, which drives the dynamics of mantle circulation. The largest such 3D structures in the Earth, the two so-called LLSVPs (Large Low Shear Velocity Provinces) situated below Africa and the Pacific Ocean, extend laterally for thousands of kilometers and extend 100s of kilometers upwards from the mantle's base. Yet, even the most recent studies that have utilized exceptional datasets, cannot agree on whether LLSVPs are denser or less dense than their surroundings. One recent study found observed deformation due to Earth's body tides required LLSVPs be significantly denser than their surroundings (Lau et al., 2017). Meanwhile, that same year, a study of Stoneley mode splitting functions favored they were buoyant (Koelemeijer et al., 2017). Unable to find consensus on the signs of density heterogeneity, let alone amplitude, dynamicists and experimentalists struggle to uniquely constrain the compositions and exact pressure-temperature conditions of some of the largest 3D structures in Earth's interior.

To address both issues of 1D and 3D density structure, in this thesis, we exploit a part of the seismic response that is most sensitive to density: Earth's free oscillations, or normal modes. Earth's long-wavelength normal modes offer the strongest constraint on Earth's density variations. Herein we revisit constraints on 1D density profile of the poorest constrained region – the inner core using modern catalogues of mode observations and utilizing increased computational resources. Additionally, we explore the viability of a new dataset of normal modes with unique sensitivity to the region containing the LLSVPs, i.e., the core-mantle boundary Stoneley modes. We explore: (1) the errors introduced by common approaches from their theoretical formulation; (2) the uncertainties introduced by other properties assumed when simulating their response; and

(3) the expected magnitude of signal associated with proposed density heterogeneity in the lowermost mantle. Finally, we revisit constraints on LLSVP density. Using conceptual density models, we demonstrate that seemingly contrasting images of LLSVP density from previous Stoneley mode and body tide studies can be reconciled, by a unifying model of a thermal, buoyant LLSVP, underlain by a very dense, thin (~100km), compositionally distinct, base – to which Stoneley modes are largely insensitive.

I dedicate this thesis to my parents, Janet and Robert Robson, and my siblings Chris and Jess Robson, for helping foster a sense of wonder and determination, and without whom I certainly wouldn't have made it this far.

Acknowledgements

I would like to thank: My advisor Professor Barbara Romanowicz for her help, support and input throughout my PhD; Professor Harriet Lau for her help, advice, and support through my final years and for lessening my dislike for Manchester United; The department staff for all their tireless work to help make mine and others research possible; and all my office mates and friends, especially: Nate Lindsey, Yuem Park, Allison Sharrar, Erin Redwing, Sevan Adourian, Daniel Frost, Sam and Hannah Horsfield, and Matthew Stott, for their support, input, and for making me smile more than I otherwise might have. Most of all, I would like to thank my Partner, Winter Martin, without whom I would have probably given up a long time ago – thanks for keeping me going.

Many thanks to all those outside Berkeley EPS who helped make my research possible, including: Gabi Laske for putting together the REM website; Raj Moulik for sharing his new mantle model in advance of publication; Hsin Ying Yang and Jeroen Tromp for sharing their code for the generation of fully-coupled synthetic seismograms; and Paula Koelemeijer for her contributions to my work on Stoneley modes. Finally, my deep thanks to my qualifying exam and thesis committee members: Professor Nick Swanson-Hysell, Professor David Brillinger, Professor Bruce Buffet, and Professor Mike Zaletel.

Table of Contents

Chapter 1

Introduction

Distribution of Earth's Mass

While the distribution of mass within Earth is itself a fundamental property, it also offers some of the most consequential constraints on other properties of the Earth system, such as composition, temperature, and dynamics, each representing an important component for understanding how our planet formed and evolves. However, despite its importance to understanding our planet, the distribution of mass within Earth's interior is still a topic of much debate (e.g. Koelemeijer et al., 2017; Lau et al., 2017).

Known within 1% of modern values since 1798, and with modern estimates boasting an uncertainty of <0.001% (Chambat and Valette, 2001), Earth's total mass represents the earliest and most rudimentary constraint on our planet's density structure. Earth's moments of inertia are similarly very well-measured from astronomical constraints and provide information on the distribution of mass with depth – Earth's 1D density profile. However, density structure solutions for both total mass and Earth's moment of inertia are highly non-unique.

Earth's 1D density profile has been further, and more uniquely constrained using seismological observations paired with the Adams-Williamson equation (Equation 1.1). First derived theoretically in 1923 (Poirier, 2000), this methodology involves propagating observed density from Earth's surface, ρ_0, towards its center, using a series of concentric, homogeneous spherical shells. Within each shell, estimates of compressional and shear seismic velocities, V_p and V_s - which are relatively readily measured compared to density – are used for the propagation.

$$\frac{d\rho}{dr} = -\frac{\rho(r)g(r)}{v_p(r)^2 - \frac{4}{3}v_s(r)^2} \tag{1.1}$$

However, the Adams-Williamson approach has some important drawbacks: (1) it assumes the process of compression within the Earth is purely adiabatic (i.e. thermal expansion does not contribute to density variations) (Fowler, 2005); and (2) that the Earth is spherically symmetric, and in hydrostatic equilibrium (not accounting for ellipticity due to rotation). Both these assumptions, while good to first order, introduce some level of error, which is compounded and propagated at each step, making estimates of the density profile at depth particularly uncertain.

Other constraints on the distribution of Earth's mass come from indirect sources, such as mineral physics experiments and *ab-initio* modelling. In the case of mineral physics, one starts with a sample of a proposed composition and applies pressures and temperatures spanning those expected in the region of the Earth being explored. Simultaneously, seismic velocities and other properties are measured for the sample. These observations can then be used to make inferences centered on the experiments' ability to match observations, primarily of V_p and V_s. However, such experiments have large uncertainties, are highly expensive, and time-consuming to perform, and as such it is impractical to explore the model-space fully. Moreover, most such experiments can only simulate pressure and temperature conditions for the upper mantle, with lower mantle experiments providing few datapoints and even greater uncertainties than those for the upper mantle. Lastly, matching seismic velocities in such experiments is non-unique due to imprecise constraints on other properties such as temperature, and so, direct observational constraints on density are highly coveted.

Earth's geoid – the height of Earth's equipotential coincident with the sea surface – also provides insight into how density varies within the planet. However, solutions to the underlying gravity and flow equations are also highly dependent on viscosity structure (Hager and O'Connell, 1981), which is similarly poorly constrained to density – particularly at great depth (Rudolph et al., 2015). These constraints on Earth's density structure are aided by observations of Earth's normal modes.

Normal Modes

Observational Background

The observational study of normal modes (also known as free oscillations) first began after the great Chilean earthquake of May 22nd 1960 (estimated Mw 9.5) (Widmer-Schnidrig and Laske, 2007). Normal modes are standing wave patterns that form across Earth's surface and radius and represent a key part of Earth's dynamical response to both external and internal forces. Their relatively low frequency and long-wavelengths give them significant sensitivity to density through self-gravitation effects induced during long wave-length deformation.

When earthquakes large enough (Mw >7) to excite normal modes occur, peaks associated with Earth's normal modes are routinely observed at very long periods (3000-200s) in the resulting frequency spectra (hereon called 'spectra') (Figure 1.1), provided available clean seismograms are sufficiently long.

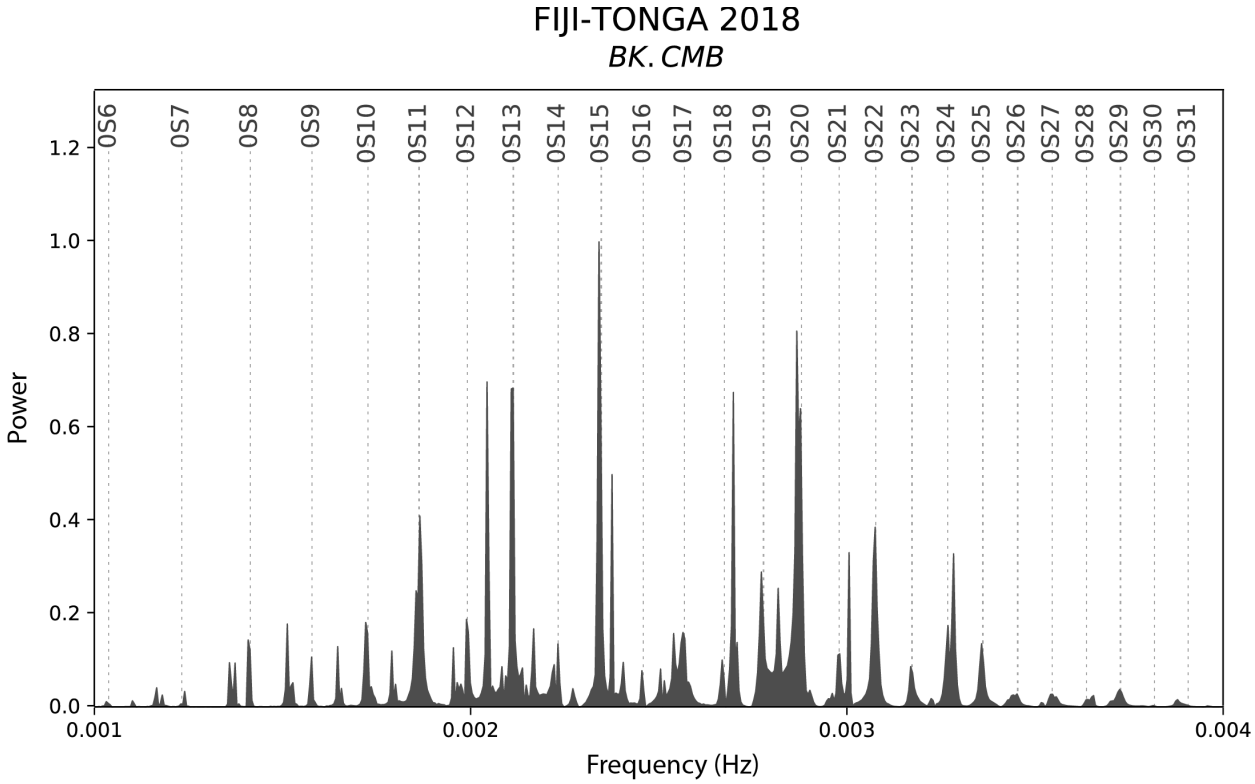

Figure 1.1 | Example normal mode spectra from a Streckeisen broadband STS-1 seismometer at station CMB, Columbia College, Columbia, CA, USA (Berkeley Digital Seismic Network). Fundamental modes are marked and labelled. This spectrum was computed using the vertical component of surface acceleration for 2-96h after the magnitude (Mw) 8.2, August 9th, 2018 Fiji-Tonga deep (600km) earthquake.

In a theoretical approximation, where the Earth is spherical, non-rotating, elastic, and isotropic (SNREI), Earth's normal modes are each uniquely characterized by a radial order, n, describing the number of nodes along Earth's radius, and an angular order, l, indicative of the pattern of motion at the surface (where $n \geq 0$ and $l \geq 0$). For a fixed l, the overtone number n indexes the modes with increasing frequency. Theoretically, these modes form an infinite series, although practically, we observe only hundreds due to issues relating to amplitude, attenuation, and noise. Given the finite size of the planet, each of these modes occurs at a discrete frequency, its so-called "eigenfrequency" (Figure 1.1), which is dependent on the 1D profile of different elastic parameters such as V_p, V_s, and density.

There are two primary types of modes, distinguished by their style of motion. Spheroidal modes, have P-SV style motion (best observed on the Z-component of a seismogram) and are written in the form ${}_n S_l$. Their counterpart, toroidal modes, are characterized by SH style motion, best observed on the noisier, horizontal transverse component of motion, and are written in the form ${}_n T_l$. Herein we focus on the former for two primary reasons: (1) the shear motion of toroidal modes cannot traverse the liquid outer core, making them of little use for studying core structure (Chapter 2); (2) CMB Stoneley modes, the focus of chapters two and three are spheroidal in nature.

For any 1D model of the Earth's elastic and density properties, the eigenfrequency of each mode can be calculated, as can its sensitivity to each elastic parameter with depth (Figure 1.2). These sensitivity kernels indicate the sign and magnitude of the eigenfrequency shift we theoretically expect to result from a perturbation to parameters at given depths. Although, the theoretical

assumptions involved (first order perturbation theory) break down if perturbations are not small. These kernels and computations may be used to study Earth's 1D structure by attempting to match observed center frequencies, which can be catalogued most simply by averaging over spectra (akin to Figure 1.1) from many earthquakes at many stations.

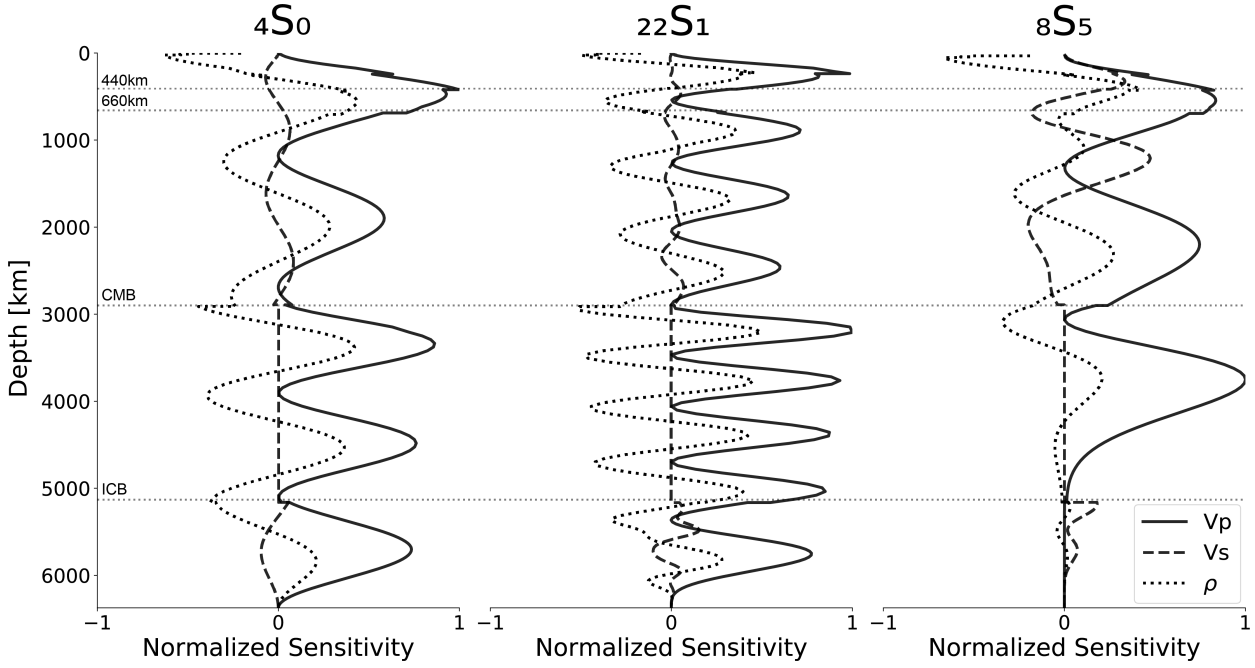

Figure 1.2 | Example normal mode sensitivity kernels for isotropic V_p, V_s, and density (ρ) as a function of depth, computed in the radially anisotropic Preliminary Reference Earth Model (PREM) (Dziewonski and Anderson, 1981) for a modes $_4S_0$, $_{22}S_1$, and $_8S_5$.

However, the real Earth is not SNREI. In reality, each mode (or multiplet) is composed of $2l + 1$ singlets, each denoted by a third value, azimuthal order, m ($-l \leq m \leq l$), which in combination with l entirely describes the pattern of motion at the surface (Figure 3). In an SNREI Earth, these different patterns of motion (singlets), are degenerate, occurring at exactly the same frequency. However, in reality due to ellipticity, rotation, anelasticity, anisotropy, lateral heterogeneity, and topography of internal boundaries of the Earth – each singlet expresses at slightly different frequencies, a phenomenon known as *splitting* (Figure 1.4). A mode multiplet k of a given type (toroidal or spheroidal) is thus defined by 3 indices: angular order l, azimuthal order m and radial order n.

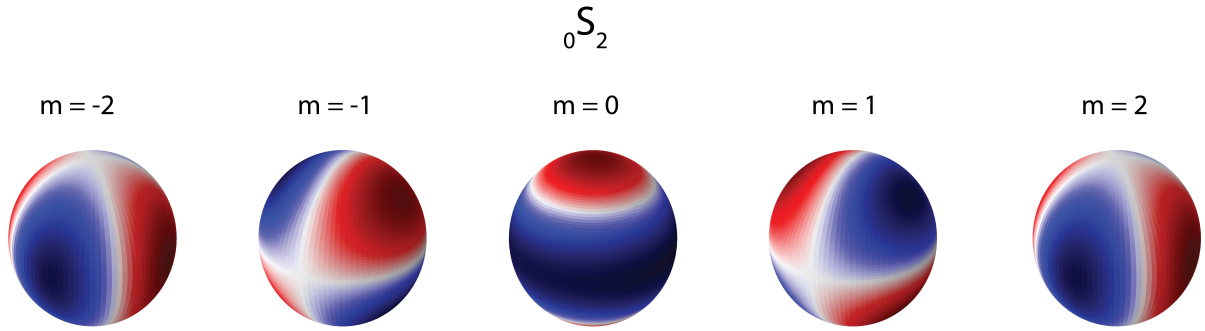

Figure 1.3 | Example normal mode patterns of motion for each of the $\boldsymbol{2l+1 = 5}$ singlets of ${}_0S_2$. Note that $\boldsymbol{|m|}$ represents the number of nodes in longitude, while $\boldsymbol{|l-m|}$ represents the number of nodes in the latitudinal direction.

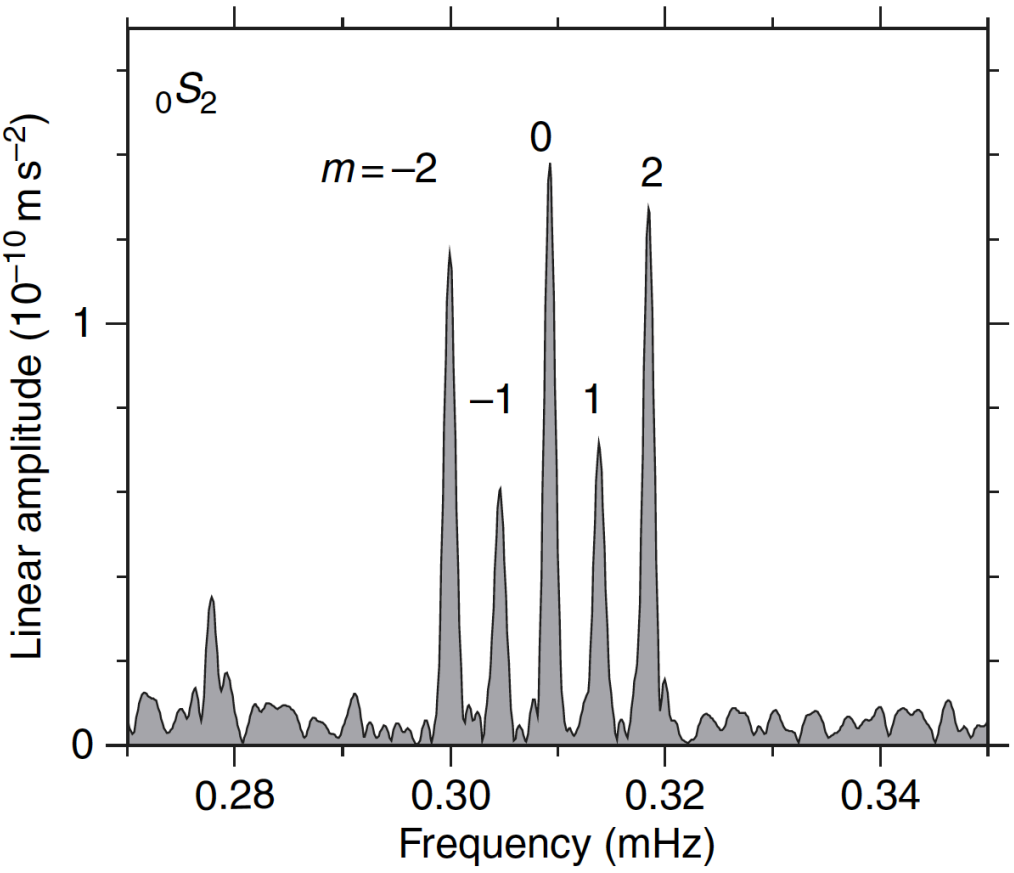

Figure 1.4 | Exceptional example of normal mode splitting of the 'football mode', ${}_0S_2$ following the 2004, Sumatra earthquake, recorded using a 500-hour long record from a superconducting gravimeter in Strasbourg, France. After Rosat (2005). See Figure 3 to visualize how each singlet's pattern of motion varies.

Splitting results in a series of $2l + 1$ tightly clustered peaks (Figure 1.4). However, commonly these peaks are smeared together, due to their proximity in frequency, the effect of peak broadening, attenuation, and processing choices necessary to enhance the signal- to-noise ratio. Practically, this smearing exhibits itself via altering the shape and amplitude of the combined multiplet which otherwise (in an SNREI Earth) might be expected to be symmetrical with respect to the center frequency.

Importantly, this means that observed modal spectra contain information on numerous facets of the planet's nature, including 3D density structure. While ellipticity and rotation are already well-known from astronomical observations (and calculations - hydrostatic shape of figure), anelasticity and lateral variations in elastic parameters such a seismic wave-speeds and, *particularly* density, remain an active field of research. This information has been commonly explored via "splitting functions" which represent a local radial average of the effect of Earth's 3D structure on the mode frequencies and can be visualized as a map (Figure 1.5) (Woodhouse and Giardini, 1985) (see Theoretical Background).

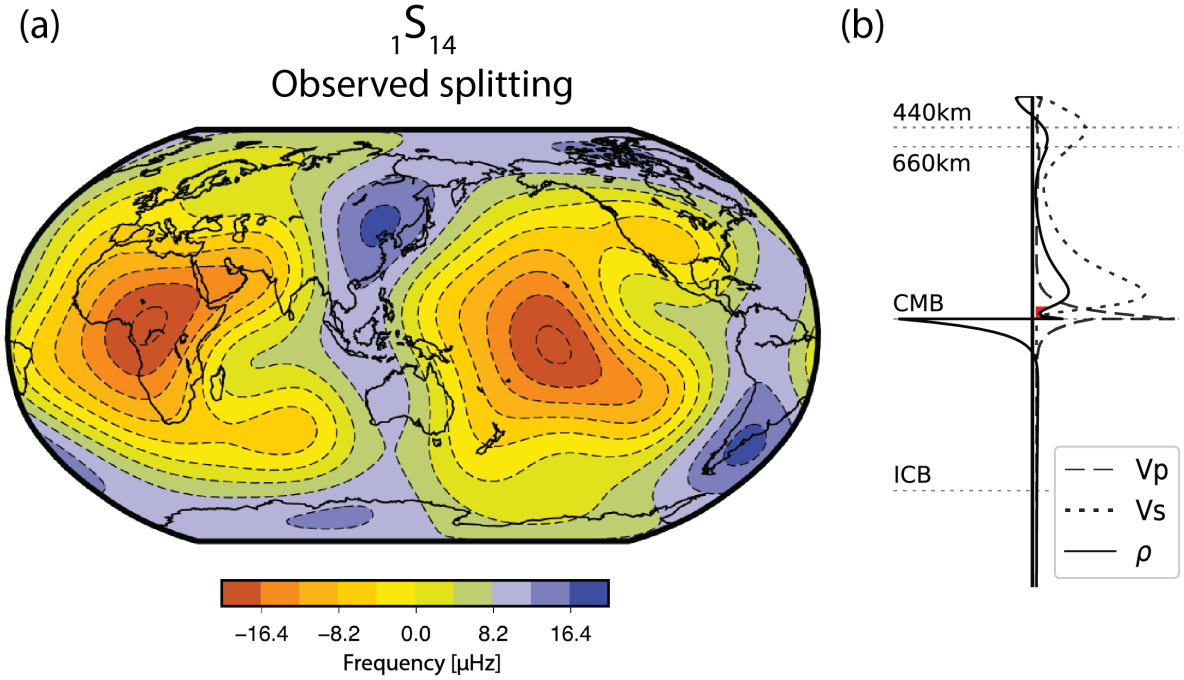

Figure 1.5 | Observed splitting function maps. (**a**) Observed splitting for mode $_1S_{14}$ plotted up to maximum structural degree s=6 (**b**) Associated sensitivity kernels for density (solid), shear wave-speed (dotted) and compressional wave-speed (dashed).

Splitting functions can be used to generate synthetic spectra (Equations 1.4-1.9). In fact, 'observed' splitting functions are constructed by iteratively generating synthetic spectra and inverting to fit observed spectra. While the resulting 'observed' splitting functions are commonly used as an observation, their generation requires the computation of synthetic spectra for many different source-station geometries. As such, the theory utilized to generate these synthetics is limited due to computational constraints, meaning, resulting splitting functions contain significant errors (Akbarashrafi et al., 2018).

Theoretical Background

The governing equation, the so-called elasto-dynamic equation of motion, is given by

$$\mathbf{H}(\omega)\mathbf{u} + 2i\omega\mathbf{\Omega} \times \mathbf{u} - \omega^2\mathbf{u} = \mathbf{0} \tag{1.2}$$

where **u** is the displacement.

The eigensolutions to this homogeneous equation, i.e., Earth's normal modes, are labeled $\mathbf{u}_k$ and the associated eigenfrequency is ω_k, where k now denotes the triplet $\{n,l,m\}$ for notational brevity (though we will make these indices explicit where required). **H** is an integro-differential operator which includes all the effects of gravity, anelasticity, and centrifugal effects, and **Ω** is the angular velocity of Earth's rotation. This equation makes no assumption about the structure of the Earth, but for the simplest case, the so-called SNREI Earth model, $\mathbf{\Omega} \rightarrow \mathbf{0}$, and and the operator **H** becomes independent of frequency and purely real. We denote these solutions with an over-bar (e.g., $\bar{\mathbf{u}}_k$).

For a non-SNREI model of the Earth, **H** contains the effects of 3D structure and ellipticity, due to rotation, $\mathbf{\Omega} \neq 0$, and mode frequencies, ω_k, are now complex, where the imaginary component contains the effect of attenuation. Herein, to incorporate more complexity into the Earth model (i.e., lateral heterogeneity, anelasticity etc.), the formulation applied is the Rayleigh-Ritz method

$$\mathbf{u}_k = \sum_{k=1}^{N} q_k \bar{\mathbf{u}}_k \tag{1.3}$$

where the vector of coefficients **q** are determined by first order perturbation theory. Equation (1.2), and the associated coefficients **q**, are solved for by the software we use (Yang & Tromp, 2015) under different approximations, which we will describe. In such an approach, we can account for the effects of ellipticity, rotation, anelasticity, anisotropy, lateral heterogeneity, and topography of internal boundaries of the Earth.

Mode Coupling

When modelling the real Earth, with complexities such as rotation and 3D structure, we must address mode *coupling*. To first order, modes which are closest in complex frequency and/or have similar physical patterns of oscillation couple most strongly, while modes far apart couple very weakly. This coupling has two primary effects. Firstly, coupled modes cause a shift in one another's m and m' singlet frequencies ($-l \leq m \leq l; -l' \leq m' \leq l'$). Secondly, coupling between certain modes provides sensitivity to odd degree structure within the Earth, to which modes would otherwise be insensitive.

Coupling also effects a modes' rate of attenuation. Different materials and conditions cause waves (including normal modes) to attenuate at different rates at different places within the earth, where this change varies most strongly with depth. Due to different modes' differing sensitivities to different depths (Figure 1.1), they experience different rates of attenuation, described by the imaginary part of their complex eigenfrequencies. However, when coupled, the bleeding of energy between modes affects this attenuation rate such that a more rapidly attenuating mode may persist longer due to coupling with a mode that decays more slowly.

Below we outline theory for simulating normal modes response to an earthquake, focusing on how different extents of coupling can be accounted for and the practical effects of these choices.

When an earthquake is triggered, the displacement may be described by an appropriate summation of the normal modes and associated forcing (the earthquake). The form of this displacement at a seismic station *j* is expressed as

$$\mathbf{u}_j(t) = \sum_{k=1}^{N} \mathbf{R}_{jk}\mathbf{a}_k(t)e^{i\bar{\omega}_k t} \tag{1.4}$$

where the summation is performed over *N* singlet modes of degenerate eigenfrequency $\bar{\omega}_k$ and **R** is a matrix which describes the motion of each singlet mode at the *j*-th station. The source and its associated excitation of any given mode is contained within the term **a**, where

$$\mathbf{a}(t) = e^{\mathbf{i}\mathbf{H}t} \cdot \bar{\mathbf{a}}(0) \tag{1.5}$$

where $\bar{\mathbf{a}}(0)$ is a vector of excitation coefficients computed for the source. **H** contains the effects of ellipticity, rotation, 3D structure and anelasticity, and its complexity depends on the complexity of the Earth model we consider. The elements for the so-called *splitting matrix* **H** are given by

$$H_{kk'}^{mm'll'} = \bar{\omega}_k \left[(a_{\text{ell}} + mb_{\text{rot}} + m^2 c_{\text{ell}})\delta_{mm'} + \sum_{s,t} \gamma_{st}^{ll'mm'} + i \sum_{s,t} \gamma_{st}^{ll'mm'} \right] \tag{1.6}$$

where *s* and *t* denote spherical harmonic degree and order, respectively, for the given structural perturbation of a material parameter *c* and dissipative perturbation due to anelasticity *d*. Within each mode pair *k* and *k*', we have $-l \leq m \leq l$, $-l' \leq m' \leq l'$, and $t = m - m'$. The effects of ellipticity and rotation are contained in the first term, where a_{ell} and c_{ell} are the ellipticity splitting coefficients, and b_{rot} is the rotational splitting coefficient (which are known; Dahlen, 1968). The $\gamma_{st}^{ll'mm'}$ are integrals over three spherical harmonics (the Wigner 3-*j* symbols; Edmonds, 1960) and ensure the term is only non-zero in specific circumstances.

For an SNREI Earth, many terms in equation 1.6 reduce to zero and **H** is simply a diagonal matrix of the singlet, degenerate eigenfrequencies of the modes. However, with added complexity such

as rotation (which induces ellipticity) and lateral structure**, H** becomes non-diagonal and modes couple via off-diagonal terms.

In the cases where $\gamma_s^{mm'} \neq 0$ the second and third terms contain splitting due to elastic and anelastic structure respectively via the structure coefficients c_s^t and d_s^t

$$c_s^t = \int_0^a \mathbf{M}_s(r) \cdot \delta\mathbf{m}_s^t(r)\, r^2 dr \tag{1.7}$$

where $\mathbf{M}_s(r)$ is a matrix of sensitivity kernels to the parameters of interest **m** (Woodhouse & Dahlen, 1978), while the coefficients $\delta\mathbf{m}_s^t(r)$ are the expansion coefficients of the 3D structure of parameters: ρ, V_p, V_s, or the radius of a discontinuity. This 3D structure is expressed by

$$\delta\mathbf{m}(r,\theta,\phi) = \sum \delta\mathbf{m}_s^t(r) Y_s^t(\theta,\phi) \tag{1.8}$$

Where $Y_s^t(\theta,\phi)$ are Laplace's spherical harmonics, θ is colatitude and ϕ is longitude.

Deciding the degree to which modes couple becomes a trade-off between the accuracy of the resulting seismogram and computational efficiency. We describe the different levels of how **H** (Eq. 1.6) is populated for a Earth-like model (non-SNREI) next.

(1) '**Self-coupling**' approximation – in which singlets are only allowed to couple with the singlets within their multiplet (same *n* and *l*). In this case, the spitting matrix for a group of modes would only contain non-zero values within square sub-blocks on its diagonal. Each sub-block of shape N-by-N where $N = 2l + 1$ (for the l of the mode associated with the sub-block) representing how each singlet within the multiplet will affect each other singlet – hence, self-coupling (Figure 1.6a). All other elements of the splitting matrix **H** (Eq. 1.6) are zero, indicating that no cross-coupling is accounted for between multiplets. Self-coupling is also the most common level of theory used in the calculation of splitting functions. While appealingly simple and very fast to compute, this style of coupling has been shown to introduce errors on the order of many of the effects researchers are looking to study, such as density anomalies (Akbarashrafi et al., 2018).

(2) '**Group-coupling**' – in which numerous multiplets are grouped and each of their singlets coupled to all singlets of all the multiplets within that group. These discrete groups vary in size from 2 modes to many and are commonly defined over frequency bands (e.g. 1.1-1.3 mHz). This is also known as 'narrow-band' coupling or wide-band in the case of a group spanning a large range in frequency. In this case, values are still non-zero outside of diagonal subblocks. However, each square sub-block is now of width $N = \sum_k 2l + 1$, where k is the index of modes in the group (Figure 1.6b).

(3) '**Full-coupling**' – here, all modes from 0 Hz up to some truncation frequency (the modes are theoretically infinite) are allowed to couple with all other modes below this frequency. That is, each of their $2l + 1$ singlets couples with *every* other modes' $2l' + 1$ singlets (Figure 1.6c). While this theory is the most accurate, it requires the computation of a very large square matrix, making it currently impractical for iterative inversions such as those used in the generation of splitting functions.

Splitting Functions

While in Chapters 3 and 4 we will mainly be exploring seismic spectra (the Fourier transform of equation 1.4), splitting functions will remain a significant part of the discussion, and we will briefly describe their construction here. Referring back to eq. (1.4), the sum of each structure coefficient multiplied by its accompanying harmonic function over all degrees and orders yields a function which varies over the surface of the earth – a splitting function map, f (Figure 1.5):

$$f(\theta, \phi) = \sum_{s,t} c_s^t \, Y_s^t(\theta, \phi) \tag{1.9}$$

where a similar expression can be written for the spatial pattern of splitting due to anelastic structure, using the anelastic structure coefficient d_s^t. Typically, this is performed using the self-coupling approximation, though recently, this has included pair-of-mode coupling (Koelemeijer et al., 2013).

There are many appealing features of using splitting functions. Since calculation of these 'observed' splitting functions is done across numerous stations and events, they destructively sum any random error in the seismic sources. They are also easily visualizable and fast to evaluate predictions against. However, in each construction, numerous iterations are required in order to fit observations. For each iteration, the forward computation of spectra, at each station, for each event, for each mode is performed. As a result, the theory used for this forward computation is often limited to that which is computationally feasible, most often achieved by applying self-coupling approximations. Such approximations have been shown to introduce non-negligible errors in the construction of splitting functions (Akbarashrafi et al., 2018; Al-Attar et al., 2012).

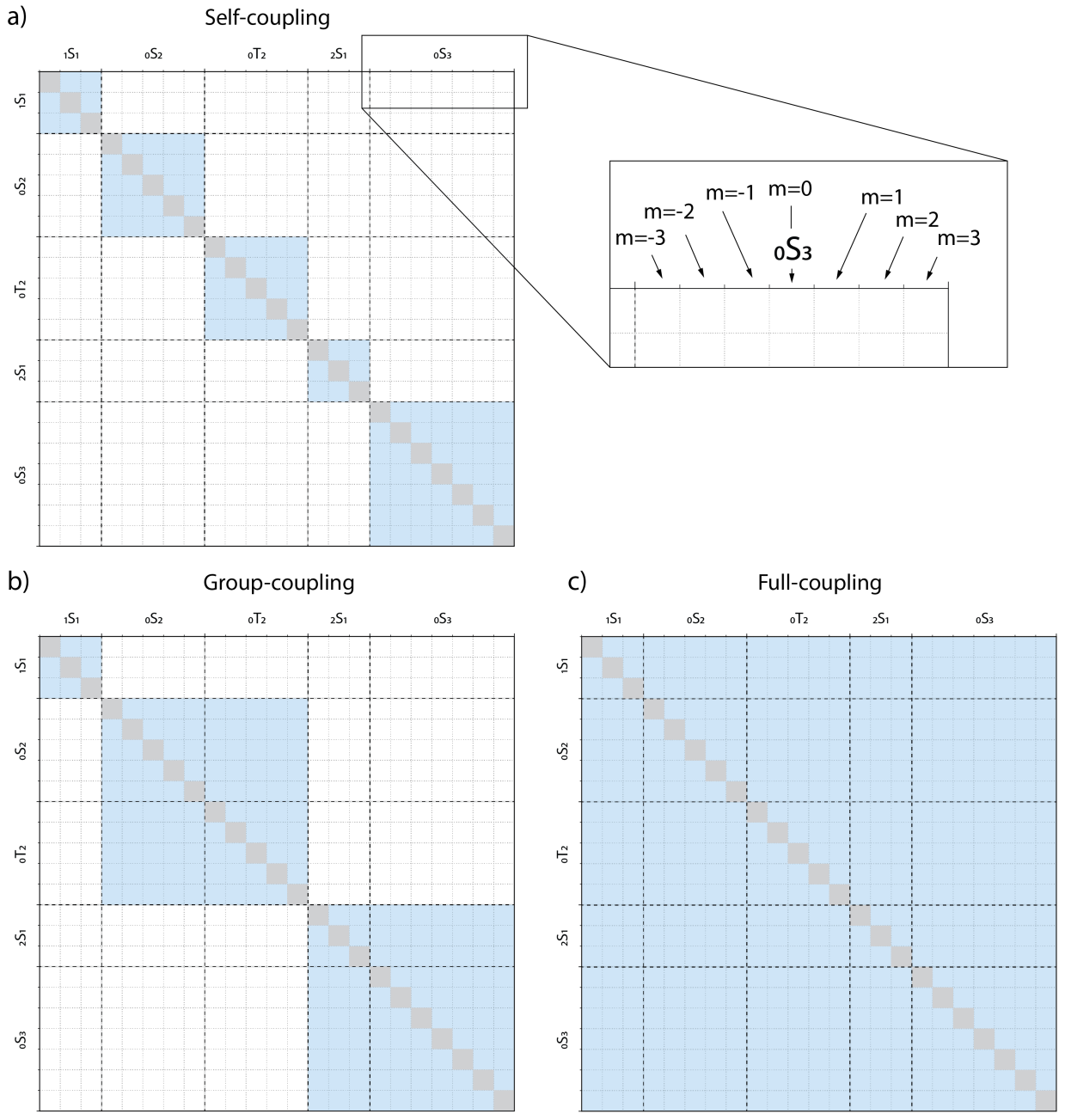

Figure 1.6 | Visualization of the coupling matrix for modes below 0.5 mHz. White space represents null values where blue shows the regions of the matrix in which coupling values are present. While coupling to 0.5 mHz results in a square matrix with dimensions 23 by 23, modes become increasingly closely spaced at higher frequencies resulting in intense computations for higher level of coupling.

Prelude

In the following chapters, we will first revisit normal mode constraints on the 1D Earth, focusing on the region with highest uncertainty, the inner core. Spanning from the center of the planet to ~ 1,220 km radius, the inner core still holds many unanswered questions, such as, when did it form, and what is its exact composition. Furthermore, the magnitude of the density contrast between the liquid outer and solid inner core is thought to offer strong constraints on the energy available to power Earth's geodynamo (Masters and Gubbins, 2003). However, estimates of its density are still largely referenced from the 1D Preliminary Reference Earth Model (PREM), constructed nearly 40 years ago (Dziewonski and Anderson, 1981). While providing stronger constraints on inner core density and seismic wave-speed structure cannot individually answer the questions above, they offer vital constraints for experiments and modelling. Using a grid-search methodology and a modern catalog of observed inner-core-sensitive normal mode center frequencies, we provide new constraints on the bulk elastic and density parameters of the inner core. We find that PREM's values are correct to within ~1-2%, with possible reductions on that order for density and V_s. Meanwhile, finer variations with depth are poorly constrained, especially near Earth's center. Finally, we conclude that a recently proposed model of inner core shear velocity (V_s) structure derived from body-wave cross-correlograms (Tkalčić and Pham, 2018) is incompatible with normal mode constraints.

Chapter 3 focuses on core-mantle boundary (CMB) Stoneley modes, which exhibit sensitivity uniquely concentrated near the CMB. First observed in 2013 (Koelemeijer et al., 2013) these modes potentially represent our strongest observational constraints on the density of the uppermost outer core and at the very base of the mantle. However, they have only been applied thus far in the form of splitting functions, assuming pair-of-mode coupling theory in their construction. We assess the magnitude of theoretical error introduced by this assumption and other levels of truncated theory by comparison to full-coupled synthetics. Simultaneously, we assess the magnitude of uncertainty introduced by other *a-priori* choices such as the velocity model, source solution, attenuation structure, and CMB topography. Finally, we contrast the magnitude of these errors and uncertainties against the magnitude of the signal expected in the case of differing conceptual models of deep mantle density structure in Earth's large low shear velocity provinces (LLSVPs). We conclude that pair-of-mode coupling is likely insufficient to resolve lower mantle density, and that improved models of mantle velocity structure will be vital for tighter constraints of the density structure of the lower mantle and uppermost outer core.

Finally, in chapter 4 we reconcile seemingly contrasting results of two recent studies on LLSVP density. The two LLSVPs below Africa and the Pacific represent the largest heterogeneities in Earth's mantle and are thought to play a key role in its evolution and dynamics. A vital ingredient to determining their dynamical nature is whether these LLSVPs are purely thermal structures (which acts to increase their buoyancy) or are partly the result of compositional heterogeneity (which, for the most likely candidates of heterogeneity, would decrease their buoyancy). Constraints on their density are highly important to resolving this question. To address the differing pictures of deep mantle density structure from these recent studies, we generate four conceptual models of LLSVP density to assess the hypothesis that these results may be explained by each dataset's differing depth sensitivity. Using the two studies original methodologies, we assess the new conceptual model's ability to explain each dataset. Additionally, we simultaneously explore

fit to a new dataset of Stoneley mode spectra, which avoids errors introduced by the pair-of-mode theory used in the generation of the splitting functions. We find that we can reconcile all three datasets via a largely thermal model of LLSVPs with a very dense base. These results represent a significant step towards a new and consistent view of LLSVP density structure.

Chapter 2

New normal mode constraints on bulk inner core velocities and density

A version of this chapter was published with Barbara Romanowicz in Physics of the Earth and Planetary Interiors, vol 295, art. no. 106310, 2019. doi.org/10.1016/j.pepi.2019.106310

Introduction

Seismological observations are central to our understanding of the Earth's core composition dynamics, and evolution. The fluid core was first discovered using seismic observations in 1906 (Oldham, 1906), by 1936 the existence of an inner-core (IC) was established (Lehmann, 1936), and its solidity finally confirmed in 1970 (Dziewonski Adam M. and Gilbert, 1971). Meanwhile, Birch established the core's primary composition: an Iron-Nickel alloy (Birch, 1952) with about ~10 wt% light-elements (LE) (Birch, 1964).

It is thought that as the outer core (OC) cools and solidifies, light elements (LEs) partition, preferentially remaining in the fluid (Birch, 1964; Jephcoat and Olson, 1987; Poirier, 1994), leaving the solid IC depleted (~3-5wt%). The resulting compositional heterogeneity is generally believed to be the driving force for the compositional convection that powers the geodynamo at present (Gubbins et al., 1979; Loper, 1978).

In the years since Birch first proposed the presence of light elements in the earth's core, numerous candidates have been suggested, including Si, O, S, H and C (Antonangeli et al., 2010; Bazhanova et al., 2012; Belonoshko et al., 2007; Caracas, 2015; Hirose et al., 2017; Martorell et al., 2013; Sakamaki et al., 2016; Tagawa et al., 2016; Vočadlo, 2007). However, both ab-initio and laboratory studies have struggled to reconcile these proposed compositions with seismic observations, consistently recovering incompatibly high velocities, even when matching density (ρ) (Li et al., 2018). This has led to various proposed mechanisms to lower V_s, such as anelasticity, premelting conditions (Martorell et al., 2013) and multiple LEs (Li et al., 2018).

Body wave travel time measurements provide strong constraints on IC V_p, since PKIKP, the inner-core compressional phase, is routinely observed. However, its V_s equivalent, PKJKP, remains elusive. Of five published observations (Cao et al., 2005; Deuss et al., 2000; Julian Bruce R.; Davies, 1972; Okal and Cansi, 1998; Wookey and Helffrich, 2008), two are thought to be in the wrong frequency band (Deuss et al., 2000), while a recent paper demonstrated the phase may be

too low amplitude to observe (Shearer et al., 2011). Body waves provide even less constraint on IC density, though amplitude ratios can provide information on the relative density jump across the ICB. As a result, constraining bulk V_s and ρ in the IC relies primarily on core-sensitive normal mode observations.

The spherically symmetric Preliminary Reference Earth Model (PREM, Dziewonski and Anderson, 1981) was constructed with constraints from normal mode center-frequency measurements, as well as body wave travel times, Earth's mass/moment of inertia, and from the Adams-Williamson equation. PREM is still widely used as a reference for the average V_s, ρ, and quality factors ($Q\mu$ and $Q\kappa$) in the inner core.

Since PREM was developed, 38 years ago, the database of observed normal mode center-frequencies has grown significantly larger and more accurate, with the addition of data from recent large earthquakes, and theoretical improvements in the measurements, such as including mode splitting and coupling due to 3D structure. Additionally, increases in computation power have made more computationally intensive methodologies accessible.

In the last 20 years, several studies have revisited normal mode constraints on IC density and velocity structure. Masters and Gubbins (2003) used a Backus-Gilbert inversion method to isolate the inner-core density signal, examining bulk IC density, and the density jump ($\Delta\rho$) across the inner core boundary (ICB). The latter is an important parameter, indicative of the degree of LE partitioning between the IC and the outer core, and thus the energy available to power the geodynamo by such a mechanism.

On the other hand, Deuss (2008) fixed inner core density to that of PREM and searched for the average shear and compressional velocities in the inner core using a grid-search forward modeling scheme, finding average velocities remarkably close to that of PREM when assuming PREM's average density. Another study utilized artificial neural networks (de Wit et al., 2014) to explore normal mode constraints on Earth's 1D structure, though its broad focus and large modal dataset predominantly emphasized sensitivity to mantle structure.

As normal mode studies were consistently finding bulk IC parameters (V_p, V_s and ρ) within 0.5% of PREM (de Wit et al., 2014; Deuss, 2008), an ab-initio study suggested for the first time that these observations could be matched simultaneously, utilizing multiple LE components (Li et al., 2018). However, within months, two papers called bulk core parameters into doubt. A recent Reversible-jump Markov chain Monte Carlo study in the outer core favored a model with increased OC density, drawing into question the robustness of PREM's density structure in the outer core (Irving et al., 2018). Soon after, Tkalcic et al. (2018) attempted to enhance PKJKP signals using a novel coda-wave correlation technique, proposing that V_s in the IC may be lower than that of PREM by ~2.5%. Yet, their best fitting model appears non-unique, and, as we will show, it does not predict the normal mode center-frequency data better than PREM, in general, and provides very poor fits to several specific modes. Additionally, as with other IC studies (Deuss, 2008), density is kept fixed to that of PREM, in spite of known tradeoffs.

Here, we utilize multiple recent normal mode catalogues, a variety of weighting and error schemes, and computational advances, to better constrain the elastic structure of the IC. We simultaneously explore V_p, V_s, and ρ via a Monte Carlo parameter-space search for models composed of a homogeneous IC (i.e. with no depth dependence), overlain by structure in the OC and mantle, which is fixed to a published 1D background model. We explore multiple background mantle models and discuss the possible influence of mantle and outer core structure on our results.

Data

Catalogues

For this study we consider two sets of observed modal center-frequencies:

- **REM (2001)** a collection of observations from numerous authors and methodologies ("Reference Earth Model," n.d.)
- **DR (2013)** observations from Deuss et al. (2013), with the addition of radial mode observations from Roult et al. (2010). Unlike REM, Deuss et al. (2013) accounts for coupling between certain modes and was generated with the addition of data from some recent large events.

Mode selection

From each of these datasets a subset of IC-sensitive modes were selected. Initially, a list of IC-sensitive modes was compiled from the existing literature (Andrews et al., 2006; Beghein and Trampert, 2003; Deuss, 2008; Deuss et al., 2013; Durek and Romanowicz, 1999; He and Tromp, 1996; Irving and Deuss, 2011; Laske and Masters, 1999; Mäkinen et al., 2014), and 23 modes not present in both REM and DR were discarded ($_1S_7$, $_2S_2$, $_3S_8$, $_5S_3$, $_6S_0$, $_6S_1$, $_6S_2$, $_7S_3$, $_7S_4$, $_7S_5$, $_{10}S_2$, $_{11}S_1$, $_{13}S_6$, $_{15}S_7$, $_{17}S_8$, $_{18}S_2$, $_{18}S_4$, $_{18}S_6$, $_{20}S_2$, $_{20}S_4$, $_{21}S_8$, $_{22}S_2$, $_{27}S_1$,) . Remaining modes were assessed on their theoretical proportion of total sensitivity within the IC. This resulted in the following 41 modes, used in the present study:

$_1S_0$, $_2S_0$, $_2S_3$, $_3S_0$, $_3S_1$, $_3S_2$, $_4S_0$, $_5S_3$, $_6S_3$, $_7S_5$, $_8S_1$, $_8S_5$, $_9S_2$, $_9S_3$, $_9S_4$, $_{11}S_4$, $_{11}S_5$, $_{11}S_6$, $_{13}S_1$, $_{13}S_2$, $_{13}S_3$, $_{14}S_4$, $_{15}S_3$, $_{15}S_4$, $_{16}S_5$, $_{16}S_6$, $_{16}S_7$, $_{17}S_1$, $_{18}S_3$, $_{18}S_4$, $_{20}S_1$, $_{20}S_5$, $_{21}S_6$, $_{21}S_7$, $_{22}S_1$, $_{23}S_4$, $_{23}S_5$, $_{25}S_1$, $_{25}S_2$, $_{27}S_2$.

Mode classification

Each normal mode presents different frequency sensitivity kernels for each of the three elastic parameters (V_s, V_p, ρ) as a function of depth (Figure 2.1).

Here, we group modes into 3 groups: "radial", "PKIKP-equivalent" or "PKJKP-equivalent" (Figure 2.2). The latter two were separated according to the relative proportion of IC sensitivity to V_p and V_s.

Observational uncertainty

Accounting for observational uncertainty is important for assessing the physical interpretability of our results. However, published uncertainty values vary by orders of magnitude between different center-frequency catalogues. Therefore, we make a conservative approach by using the measurement variability, i.e. the differences ($\Delta\omega$) between observed center-frequencies in our chosen catalogues, REM and DR (Figure 2.3), as an estimation of uncertainty. The corresponding uncertainty estimates are on average an order of magnitude larger than the published estimates in DR, though still significantly smaller than those of REM (Appendix Figure - A1). Each mode is then assigned a grouping based on the magnitude of the corresponding difference. The estimated observation uncertainty, σ_{est}, is calculated as the median difference, $\overline{\Delta\omega}$, scaled by a factor assigned to each group, G.

$$\sigma_{est} = G\overline{\Delta\omega} \tag{2.1}$$

Here we assign low (Group 1), intermediate (Group 2) and high Δω (Group 3) modes scaling factors of 1, 2 and 3 respectively. However, we note that the choice of these factors has little effect on results within reasonable limits (results are stable until the denominator of the cost function varies by a factor of ~750 between group 1 and 3).

Background models

To explore the effects of assumed mantle and OC structure on recovered IC structure, we utilize two background models, PREM (Dziewonski and Anderson, 1981) and NREM (Moulik, personal correspondence, 2019 based on Moulik and Ekström, 2016). Both models were independently constructed to fit normal mode observations, using different datasets and assumptions. These models were used here to provide all elastic and anelastic structure outside of the IC, and for IC quality factors.

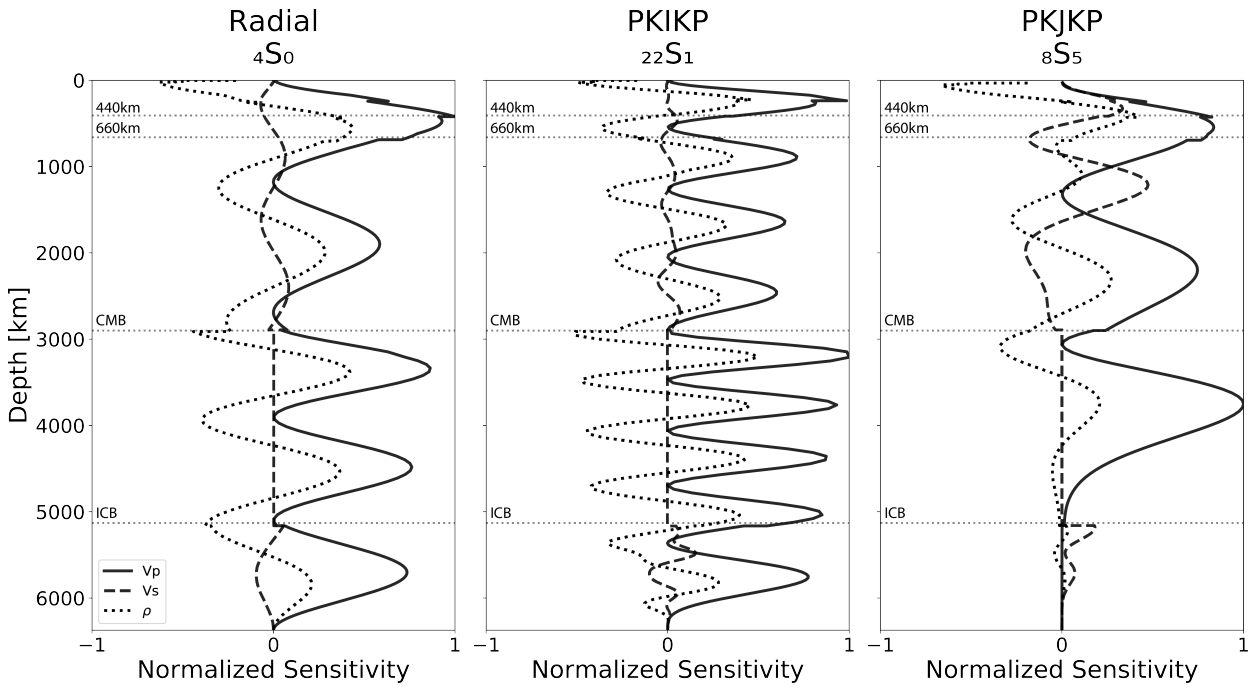

Figure 2.1 | Normalized sensitivity kernels of IC-sensitive modes: $_4S_0$, $_{22}S_1$, $_8S_5$ (calculated in PREM), showing the relative predicted center-frequency shift expected for a perturbation in the model in V_p, V_s and ρ, respectively.

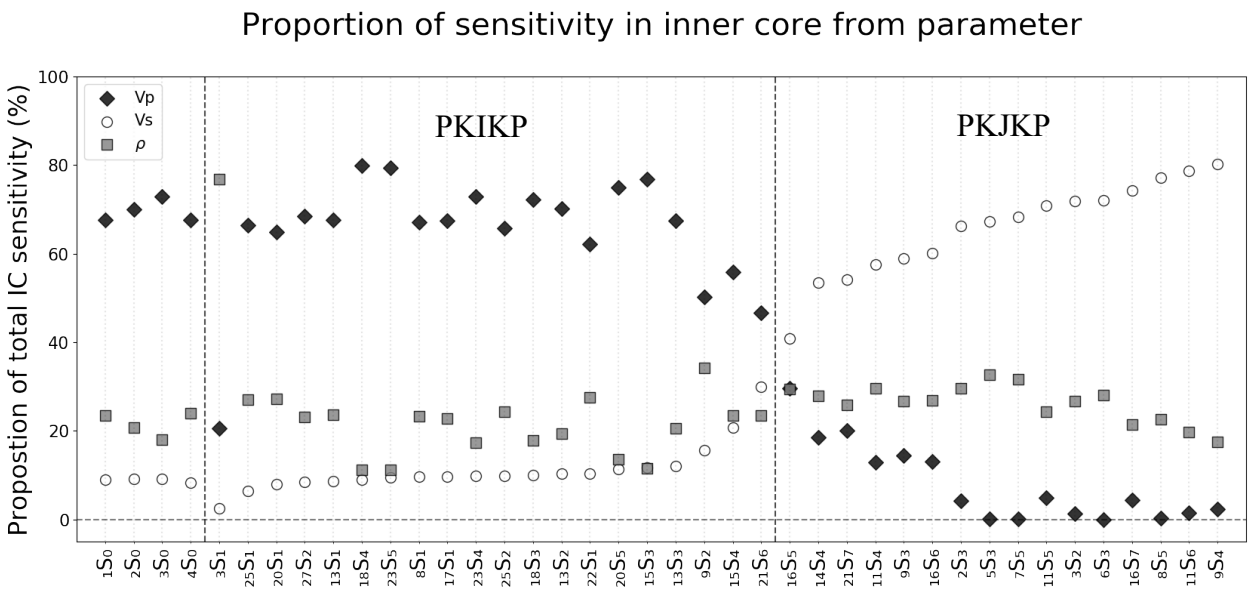

Figure 2.2 | The relative proportion of IC-sensitivity to V_p, V_s and ρ for each mode considered. Values represent the percentage of the sum of the integrals over depth in the IC of each parameter's sensitivity kernel (Figure 2.1). Dashed vertical lines separate modes characterized as radial, PKIKP and PKJKP.

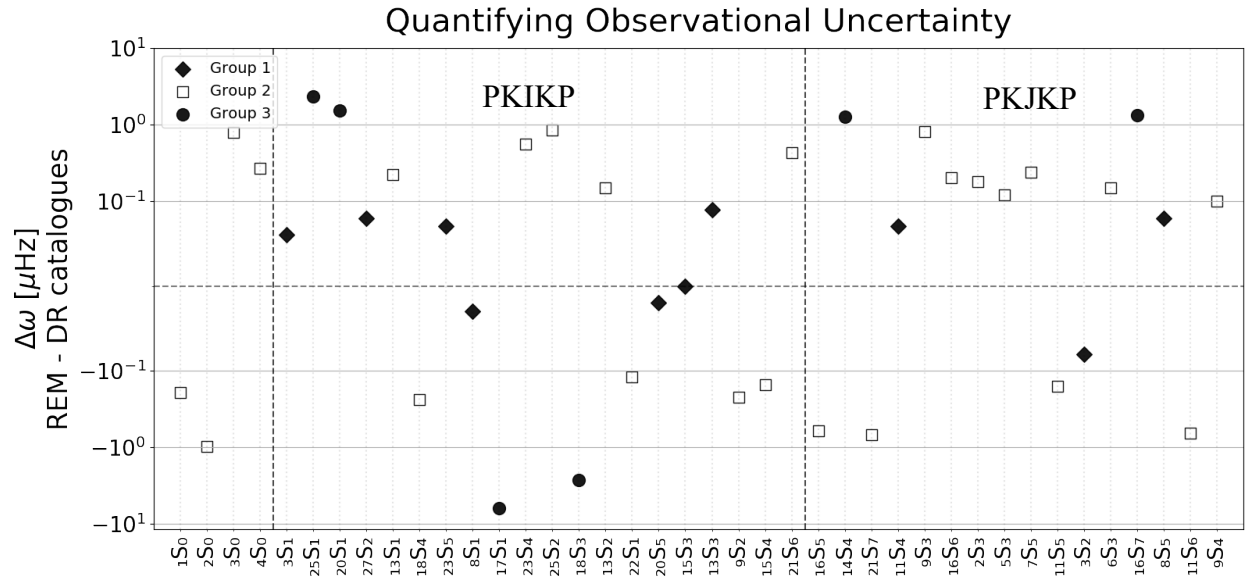

Figure 2.3 | Observational uncertainty grouping. For each mode the signed difference in observed frequency between REM and DR is plotted (Δω). Different symbols denote the corresponding uncertainty grouping. e.g. circles are Group 3, the observations with poorest agreement between catalogues, resulting in a $\boldsymbol{\sigma_{est} = 3\bar{\sigma}}$, where $\bar{\boldsymbol{\sigma}}$ is the median Δω across all modes (0.21 μHz). Horizontal broken lines separate the different groups.

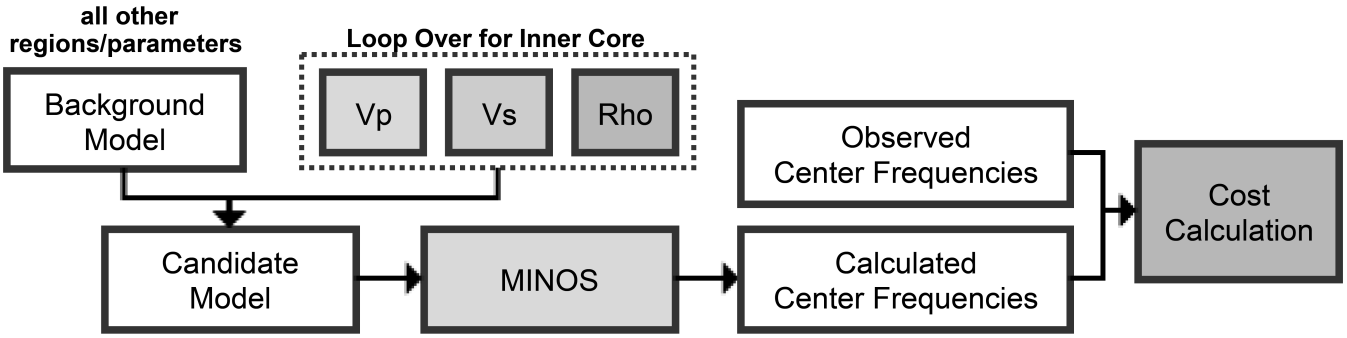

Figure 2.4 | Parameter-space search methodology. A suite of models is generated, each with a unique homogeneous inner core in V_p, V_s and ρ. All other parameters and regions are set to the background model. For each of these unique models, center-frequencies are calculated via MINOS and the cost function evaluated (Equation 2.2)

Methodology

We consider average, homogeneous inner core models, ignoring any depth-dependence in V_p, V_s and ρ. Since these parameters vary slowly within the IC, this is a good first-order approximation of IC structure and helps mitigate computational limitations. We explore this 3-dimensional parameter-space via a grid-search, following the procedure outlined in Figure 2.4.

Within some a-priori bounds, containing all proposed seismological and experimental estimates, we generated a suite of 1D models, each composed of a homogeneous IC in V_p, V_s and ρ, overlain by a published background model (e.g. PREM or NREM). IC quality factors were also fixed to those of the background model, as preliminary testing showed multiple orders of magnitude higher sensitivity to changes in V_p, V_s and ρ, than in Qκ or Qμ. This also limited the dimensions of the problem, further reducing computations. Parameter spacing within the grid search was kept constant across runs, with velocities and ρ varying in increments of 10m/s and 10kg/m^3, respectively.

For each model, normal mode center-frequencies were predicted for our selection of IC-sensitive normal modes using MINOS (Woodhouse, 1998). A sum of squared differences was computed against a catalogue of observed center-frequencies and a cost assigned to each model (Equation 2.2).

$$\phi = \sum_{i=1}^{N} \frac{\left(\omega_i^{obs} - \omega_i^{calc}\right)^2}{\sigma_i^2} \frac{1}{C_i} \tag{2.2}$$

Here N is the total number of modes, and ω denotes mode frequency. Each mode's contribution to the cost function is weighted by two factors, observational error, σ_i, and mode character, $\mathbf{C}_i$ (e.g. Figure 2.1, PKIKP, PKJKP or radial mode). **W**e consider two different C-weighting schemes:, (a) where all modes have equal weights – "**all-equal**" (C_i=N for all i's) and the other and (b) "**PPR"**, which accounts for the different number of modes in each mode group (PKIKP,PKJKP, radial). In scheme (b) $C_i=3M_i$ where M_i is the number of modes within i-th mode's mode group. Normalizing by sensitivity groupings can help improve the strength of constraints provided by IC-sensitive normal modes on bulk IC parameters (Deuss, 2008).

The methodology outlined (Figure 2.4) was repeated 16 times, for each permutation of 1) our two C-weighting schemes: PPR and all-equal 2) different observational catalogues: REM and DR 3) different background models: PREM and NREM and 4) different σ values: with our estimation of

observation uncertainty $\sigma = \sigma_{est}$, as described earlier, and using normalization by observed frequency, $\sigma = \omega_{obs}$. The latter ensures that differences are not unintentionally upweighted for high frequency modes i.e. a 1% difference will be weighted the same at all frequencies.

Results

The bulk IC velocities are found to be consistent across all 16 runs (Table 2.1). V_p values vary between 11,160 - 11,180 m/s, with a standard deviation of just 8 m/s, and are in good agreement with Deuss's proposed 2008 value (11,150 m/s) as well as PREM's IC average (11,183 m/s). V_s values are similarly well-constrained (3,560 - 3,590 m/s with a standard deviation of 10 m/s) and exhibit a minor reduction of ~1% with respect to PREM (34 m/s) and are in better agreement with Deuss (3,550 m/s). N.B. Unless otherwise stated, reference averages computed in the reference PREM model are linear averages, as volumetric averages overly emphasize the outermost inner core's effect on modal frequencies. While we also acknowledge linear averages underemphasize this contribution, we believe the context of our results are largely independent of this decision. Though for clarity, volumetric averages are marked alongside the linear averages in Figure 2.5.

Our results provide looser constraints on IC density, with values ranging from 12,720 – 12,880 kg/m^3(+/- 54 kg/m^3) (Figure 2.5). Still, the results show a reduction in average IC density with respect to PREM on the order of 1.3%, with a mean density of 12,801 kg/m^3

The level of constraints on each of these variables can be seen in a different way by visualizing the cost function across the parameter-space (Figure 2.6). The cost function exhibits a steeper gradient and thus greater sensitivity in V_s while showing less stringent constraints on V_p and relatively weak constraints on ρ. Still, the V_p remains the closest to PREM.

Background Model	NREM								Mean	S.D.	PREM Min.	PREM Max.	PREM's Linear Average
Observations	DR				REM								
C-weighting	PKIKP:PKJKP:Radial		All-equal		PKIKP:PKJKP:Radial		All-equal						
σ-weighting	ω_{obs}	σ_{est}	ω_{obs}	σ_{est}	ω_{obs}	σ_{est}	ω_{obs}	σ_{est}					
Vp	11180	11170	11170	11160	11180	11160	11170	11160	11169	8	11028	11262	11183
Vs	3570	3570	3570	3570	3560	3570	3570	3570	3569	4	3504	3668	3612
ρ	12760	12820	12750	12790	12720	12790	12720	12770	12765	35	12764	13089	12979
Model Name	A	B	C	D	E	F	G	H					

Background Model	PREM								Mean	S.D.	PREM Min.	PREM Max.	PREM's Linear Average
Observations	DR				REM								
C-weighting	PKIKP:PKJKP:Radial		All-equal		PKIKP:PKJKP:Radial		All-equal						
σ-weighting	ω_{obs}	σ_{est}	ω_{obs}	σ_{est}	ω_{obs}	σ_{est}	ω_{obs}	σ_{est}					
Vp	11170	11170	11160	11160	11180	11170	11160	11160	11166	7	11028	11262	11183
Vs	3580	3590	3590	3590	3580	3590	3590	3590	3588	5	3504	3668	3612
ρ	12810	12880	12830	12880	12750	12870	12800	12860	12835	46	12764	13089	12979
Model Name	I	J	K	L	M	N	O	P					

Table 2.1. The homogeneous IC parameters associated with the lowest cost models for each of the 8 runs using NREM in the mantle and OC (top) and those using PREM (bottom). Mean and standard deviation values are also shown for each subset, as are PREM's linear averages, maximum and minimum values for comparison. A reduction in V_s and ρ with respect to PREM can be seen across all runs and is particularly pronounced in the runs with NREM in the outer core and mantle. The distribution of these models can be visualized in Figure 2.5.

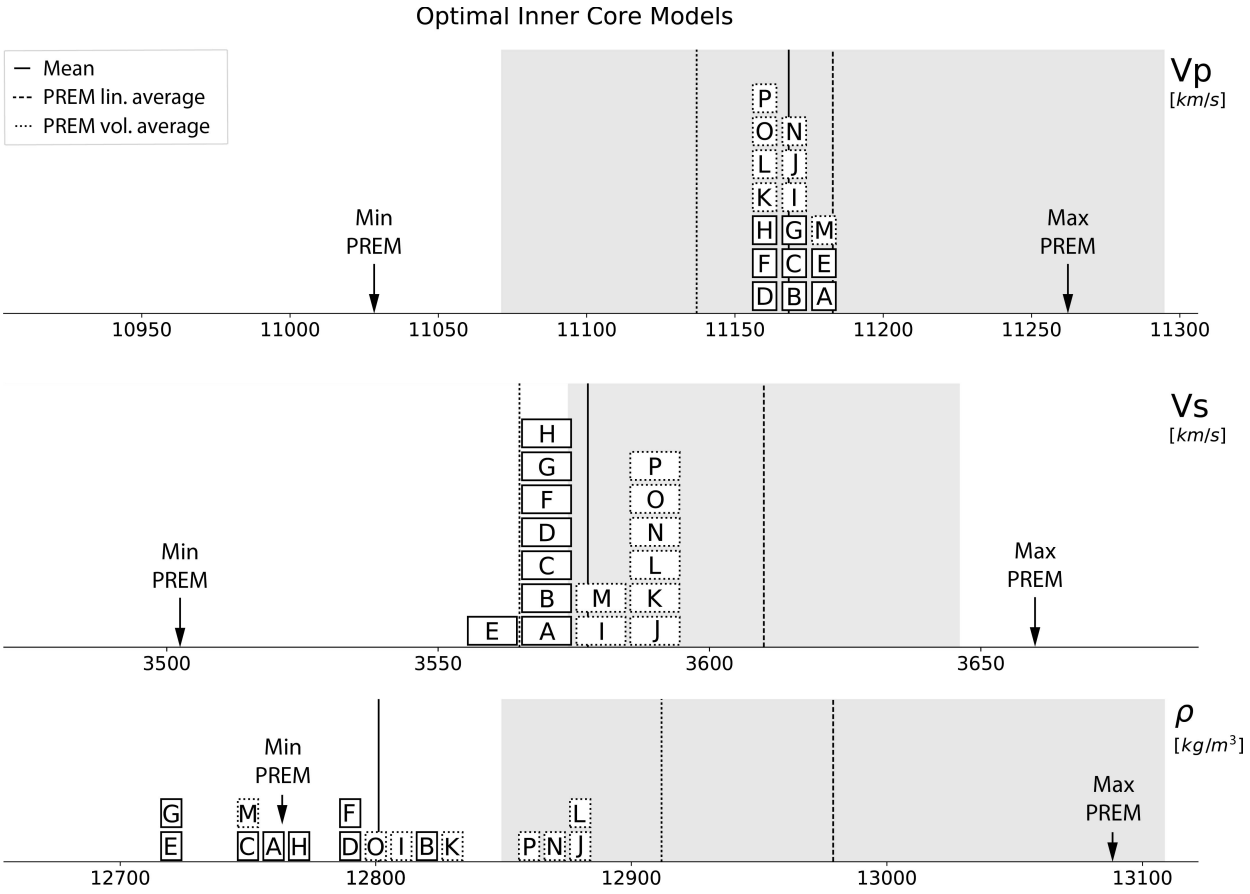

Figure 2.5 | Histogram showing the distribution of parameters in the 16 best-fitting models. Letters correspond to the final letter of the model names shown in Table 2.1. The grey box represents a 1% variation in PREM's linear average for each parameter. Models using NREM's mantle and outer core (solid outlines) are distributed towards lower values in V_s and ρ than PREM's (dotted outlines), while there is no clear difference between the two background models in V_P.

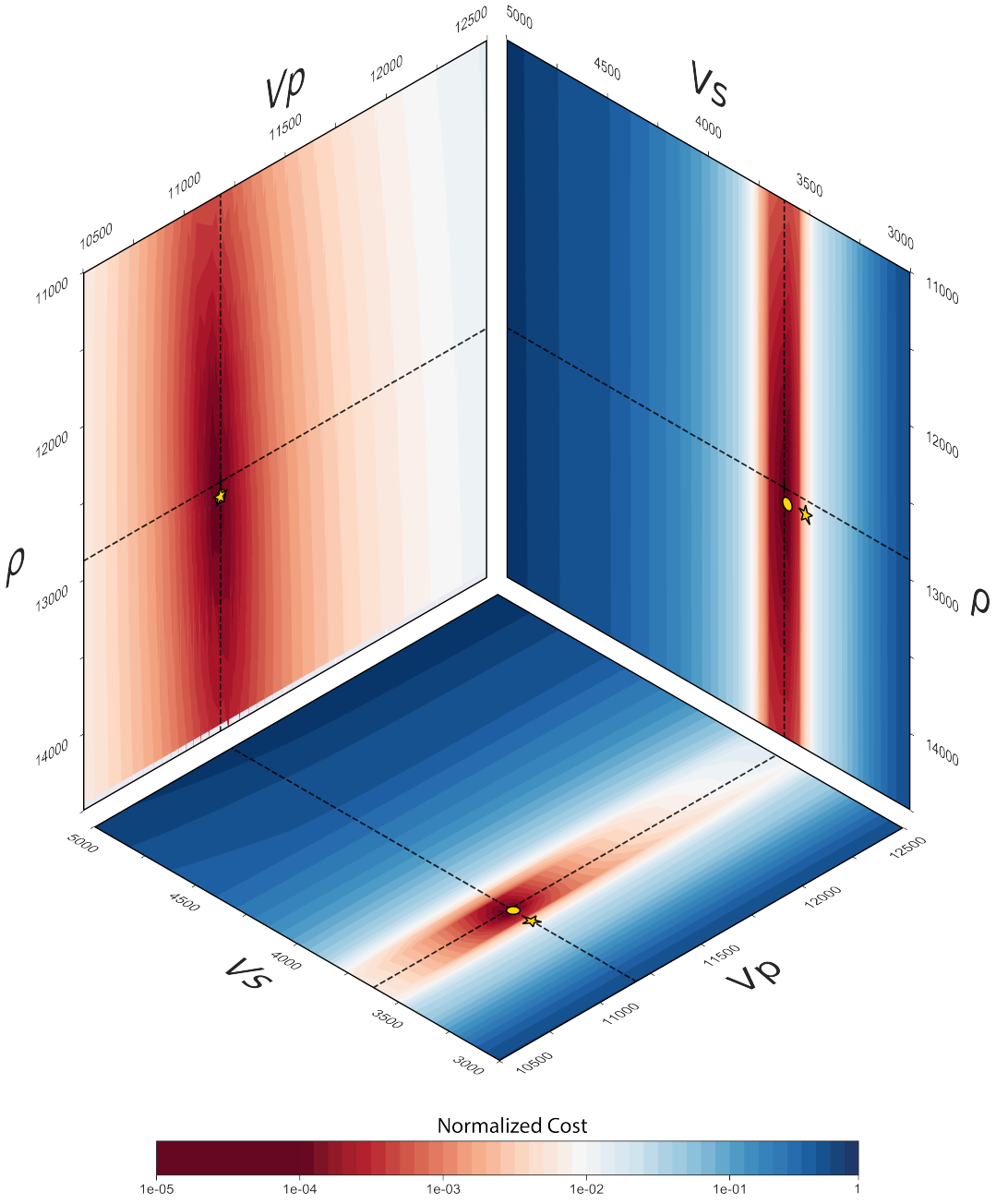

Figure 2.6 | The normalized cost function across the parameter space (Run A, in Table 2.1). Dashed lines represent where the three panes intersect, and the lines cross at the minima. The location of a model with -2.5% V_s in the inner core is marked with a star, showing an increase in cost of 2.5 orders of magnitude, with respect to the best-fitting model, while PREM's average IC values (marked with a yellow circle; note: circle and star overlap in ρ/Vp space) are associated with roughly 157% the cost of the best fitting model. V_s exhibits the steepest gradient in the cost function, indicating it is the best constrained parameter when holding run parameters such as the background model, and dataset, constant. V_p is still well-constrained and in very good agreement with PREM, V_s favors a minor reduction (1.1%) with respect to PREM, while the best-fitting density is ~219kg/m^3 lower than PREM (~1.7%). The location of a model with -2.5% V_s in the inner core is marked, showing an increase in cost of 2.5 orders of magnitude, with respect to the best-fitting model.

Discussion

We have shown that the recent normal mode center-frequency catalogs considered provide constraints on bulk IC V_p, V_s and ρ that are largely independent of the dataset, data uncertainty, and to some extent on the choice of reference OC and mantle model.

Additionally, to explore the effects of a deviation from PREM's IC radius, proposed by a recent normal mode study (de Wit et al., 2014), we performed tests (not shown), finding results were insensitive to changes in IC radius within reasonable bounds (±20km). We did not explicitly explore the effect of inner core anisotropy (Woodhouse et al., 1986) on the center frequencies, ignoring the effects of cross-coupling due to IC anisotropy and 3D mantle structure in our simulations. However, in contrast to the construction of PREM, developed before the discovery of anomalous mode splitting, recent normal mode measurements are based on extracting the constant, "00" term in a spherical harmonic expansion of mode splitting functions, while the anisotropy signature is in the higher order terms. Also, since we compare the results based on two different catalogs, constructed from measurements by different authors, using different techniques, we may assume that any hidden effect of anisotropy may be reflected in the conservative errors we have assigned to the data.

We note that a recently proposed reduction in V_s of 2.5% in the IC, keeping V_p and ρ fixed at the PREM values (Tkalčić and Pham, 2018), is incompatible with normal mode observations, exhibiting orders of magnitude higher cost than best-fitting models (Figure 2.6). Additionally, while most mode center-frequencies in our catalog are arguably fit no worse than by other existing models (Figure 2.7), several modes stand out: predictions for modes ${}_{27}S_2$, ${}_{22}S_1$ and ${}_{18}S_6$ are particularly poor (considerably outside observational uncertainty, e.g. Figure 2.3), and predictions for at least two additional PKJKP modes (${}_8S_5$ and ${}_9S_4$) are also outside of error bounds. The effects of this V_s perturbation vary (Figure 2.7) across modes with similar IC sensitivity proportions (Figure 2.2), emphasizing the importance of parameter trade-offs and the need for a simultaneous search. While Tkalcic et al. (2018) did additionally explore V_p and Qμ, these where separate steps keeping other parameters fixed while they varied, leaving trade-off effects unexplored

Density values are less well-constrained than velocities. However, our results consistently favor a significant reduction in average density with respect to PREM (0.7-1.9%). This reduction may result from differences in the observed center-frequencies in our catalog, compared to those used in the construction of PREM. It may also result from the additional constraints used in PREM, such as the Adam-Williamson equation, and Earth's Mass and moment of inertia. Clearly, normal mode observations alone offer poorer constraints for IC density than for other parameters (Figure 2.6), and while mass and moment of inertia are well known, these parameters do not help to constrain IC density, given uncertainty in shallower density structure (Irving et al., 2018). We note that slightly lower V_s and ρ values are obtained when fixing structure in the mantle and outer core to that in NREM (Figure 2.5) , which presumably is an improved 1D model over PREM. Considering the values obtained with NREM, the data require a reduction of 1.1% in V_s and 1.3% in ρ with respect to PREM.

Finally, we acknowledge that mode sensitivity to V_p, V_s and ρ reduces to zero at the Earth's center (Figure 2.1). As a result, on average, normal modes have greater sensitivity at shallower depths, so that best-fitting bulk IC parameters may be more representative of the top part of the IC.

It is clear that normal modes favor a reduction in IC density with respect to PREM, though the magnitude of such a reduction is weakly constrained (Figure 2.5/2.6). This reduction may have important implications for our understanding of the driving mechanism of the geodynamo. When considered with PREM's outer core, best-fitting models reduce the magnitude of the density jump ($\Delta\rho$) at the ICB in PREM (603kg/m^3) by between 89 and 242 kg/m^3. This is significant given the magnitude of the density jump due to solidification alone can be estimated to be about 210kg/m^3 (Alfè et al., 2000). As such, our density reduction may reduce the jump associated with light element partitioning by over half, having significant implications for the ability of that mechanism to power the geodynamo. This issue is potentially compounded when considering the results of another recent mode study in the outer core (Irving et al., 2018), which favored an increase in average OC density. This would bring the mode-derived value close to the lower end of the values obtained from recent PKiKP/PcP amplitude ratio measurements, which span a range of 300 to 1200 kg/m^3 for $\Delta\rho$ (e.g. Cao and Romanowicz, 2004; Koper and Dombrovskaya, 2005; Shen et al., 2016; Tkalčić et al., 2009; Waszek and Deuss, 2015), although the higher values obtained in some of these studies may be due to amplification due to focusing by topography on the inner-core boundary.

While we present results for the simplest possible parameterization of IC parameters, attempts were made to explore depth dependence via both linear and quadratic forms. However, when using center-frequencies alone, the higher order terms – and so the gradients – were unstable and highly dependent on the choice of grid-search points for the zeroth order term. Introduction of additional independent constraints from mineral physics, such as a Birch type V_p-ρ relation (Birch, 1961; Sakamaki et al., 2016), or assuming hydrostatic equilibrium is necessary to stabilize results and reduce the dimensions of the problem.

Overall, our results reaffirm PREM's average IC V_p, suggest a slight reduction in V_s (~1%) and a larger reduction in density (~0.7-1.9 %), while acknowledging limitations in constraining IC ρ based on normal mode center-frequency data alone.

Conclusions

Using a catalog of well-characterized IC-sensitive normal mode center-frequencies based on recent measurements, and exploring variations in average V_s, V_p and ρ in the IC simultaneously, we have shown that IC velocities are well-constrained by these data, independent of choice of: dataset, mantle model, data uncertainty and IC radius. We find V_p is in good agreement with PREM and a minor reduction in V_s with respect to PREM is favored (~1%). We show that a more significant reduction of 2.5% in V_s , while fixing ρ to PREM as proposed by Tkalcic et al. (2018), is incompatible with normal mode center-frequency observations. Meanwhile, normal mode center-frequency data favor a reduction in average ρ in the IC of between 0.7 and 1.7%, although data-sensitivity to ρ is significantly lower than to V_p and V_s.

While normal modes alone struggle to constrain the elastic parameters' depth-dependence within the IC, these best-fitting average values and their associated standard deviations may be useful for laboratory and ab-initio studies aiming at constraining IC composition. If confirmed, the slight density reduction favored by our models may have important implications for the energy available to power the geodynamo, potentially reducing the magnitude of the ICB density jump associated with light element partitioning by over half, compared to the PREM value.

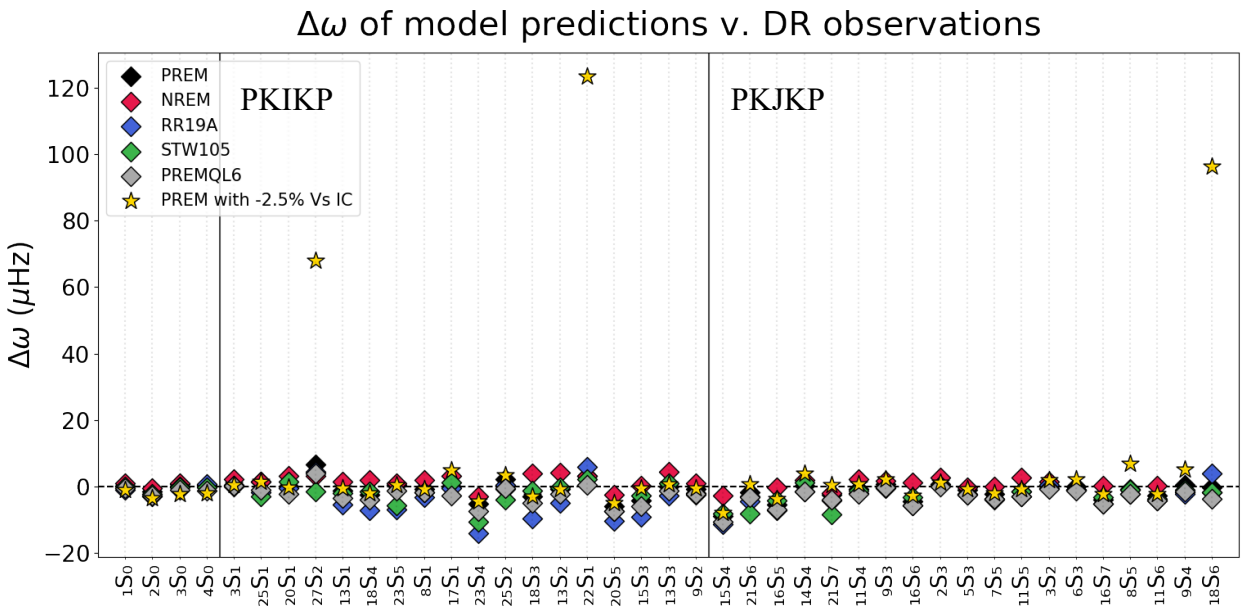

Figure 2.7 | Comparison of center-frequency predictions to DR observations. For each IC-sensitive mode the difference between its predicted eigenfrequencies and observed (DR) eigenfrequencies is shown. Models include: PREM, NREM, PREMQL6 (Durek and Ekström, 1996; Dziewonski and Anderson, 1981), STW105 (Kustowski et al., 2008), and the best-fitting model from Figure 2.6 – Model A. Notably, a reduction of 2.5% in IC shear velocity (stars) is associated with increased misfits for many IC-sensitive modes, particularly ${}_{8}S_{5}$, ${}_{9}S_{4}$, ${}_{18}S_{6}$, ${}_{22}S_{1}$ and ${}_{27}S_{2}$. Note, ${}_{18}S_{6}$ (far right) was not used to generate our models as it was not present in REM. However, it is a PKJKP-like mode with high IC-sensitivity to V_s. Please note, all models are depth dependent in the IC other than RR19A (Model A – Table 2.1) which has a homogeneous IC.

Chapter 3

Constraining density with core-mantle boundary Stoneley modes: An analysis of sensitivity and sources of uncertainty

Introduction

Resolving the properties of the mantle is a fundamental goal of deep Earth seismologists. Tomographic images, a powerful seismological tool that illuminates structures present in the mantle, provide observational constraints for modelling mantle dynamics, and insights on how our planet might have evolved over geological times. Tomographic images of the lowermost mantle have become increasingly consistent at long wavelengths, imaging structures similarly across a variety of methodologies, parameterizations, and with quasi-independent datasets (e.g. Lekic et al., 2012). While exact amplitudes of velocity anomalies somewhat differ even at the longest wavelengths, and resolution of smaller structures and their boundaries remain an active area of research, large scale tomographic seismic velocity structure in the lowermost 500 km of the mantle is by now well constrained up to ~degree 16 in a spherical harmonics expansion (Figure 3.1).

While tomography provides ever-increasing resolution of the velocity structure of the lower mantle, 3D density structure is still poorly constrained. In most cases it is scaled directly from models of shear velocity (V_s) (e.g. Kustowski et al., 2008; Moulik and Ekström, 2014; Ritsema et al., 2011), assuming a linear relation based upon laboratory experiments. Fundamentally, this relation imposes that density must share the same pattern of heterogeneity as shear velocity and assumes seismic anomalies are purely thermal in origin (e.g. Karato, 1993). However, we have increasing cause to believe certain regions of the mantle may be compositionally distinct. Geochemical studies of tungsten (Mundl et al., 2017; Rizo et al., 2016) and helium (Jackson et al., 2017) isotopes suggest the presence of an unmixed, primordial, compositionally distinct reservoir within the mantle. Among the candidates proposed to house these chemically distinct reservoirs are the Large Low Shear Velocity Provinces (LLSVPs), two antipodal mantle regions of anomalously low shear wave velocity beneath Africa and the central Pacific Ocean (Figure 3.1 and Appendix Figures B1,2) (e.g. Jackson et al., 2018; Williams et al., 2019).

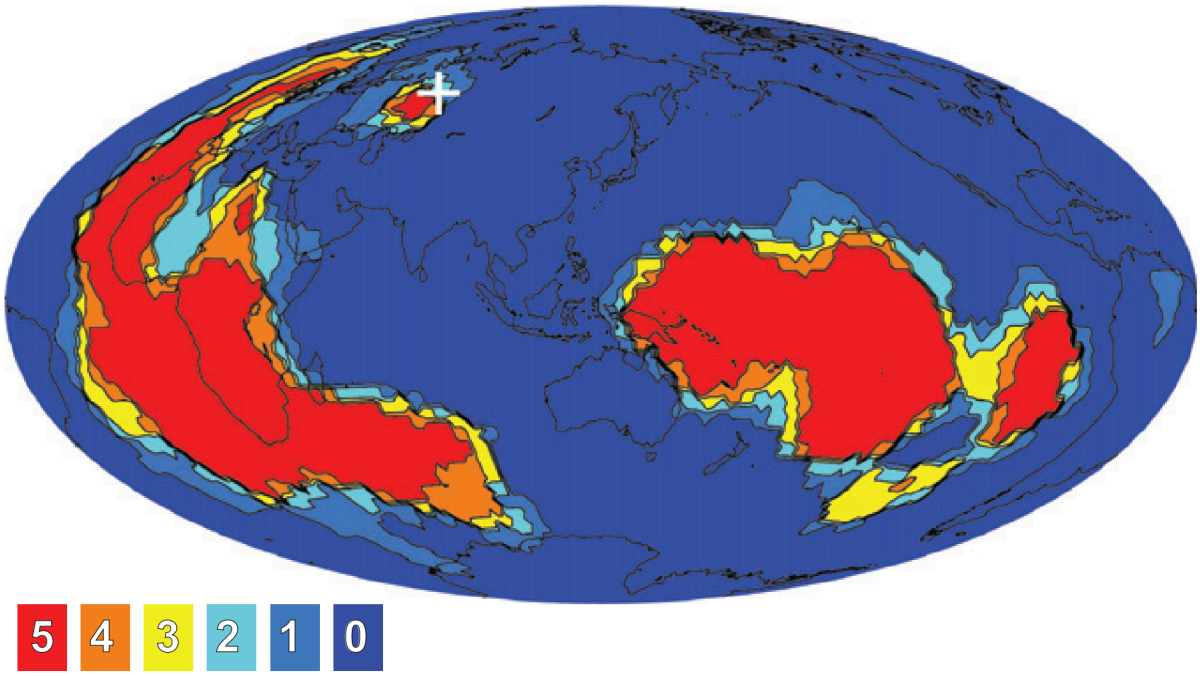

Figure 3.1: **Lower mantle shear velocity vote map** showing a cluster analysis of shear velocity (V_s) profiles from five global tomographic models (Megnin and Romanowicz, 2000; Houser et al., 2008; Kustowski et al., 2008; Simmons et al., 2010; Ritsema et al., 2011) in the 1000–2800 km depth range. Colors indicate the number of models which showed lower the average shear velocity in a given pixel, such that red indicates all 5 models show reduced velocities. Two regions are clearly separable with geographic extents consistent across all 5 models, outlining the African and Pacific LLSVPs, as well as a single, globally continuous, faster-than-average region. The models are spatially filtered to exclude power at spherical harmonic degrees >12, while the white cross represents a reconstructed center of the Siberian Traps eruptions which coincides with an isolated low shear velocity anomaly detected in all models. Taken from Lekic et al. (2012)

Numerous seismological observations also indicate that the LLSVPs are compositionally different from their surroundings. First, negative correlations between bulk sound and shear wave velocity variations have been found within the LLSVPs which is inconsistent with a purely thermal cause of shear wave speed reduction (Kennett et al., 1998; Koelemeijer et al., 2016; Masters et al., 2000; W. J. Su and Dziewonski, 1997). Second, normal mode studies find a ratio of shear to compressional wave speeds in the lower mantle that exceeds realistic values for purely thermal observations (Robertson and Woodhouse, 1995; Romanowicz, 2001; Moulik and Ekström, 2016). Finally, the boundaries of LLSVPs represent the highest lateral seismic velocity gradients present within tomographic models (Garnero et al., 2014; Thorne et al., 2004) and have been shown to be very sharp by other methods such as forward modeling of waveforms and the study of scattered waves (Frost and Rost, 2014; He and Wen, 2012; Helmberger and Ni, 2005; Ni et al., 2002; Ni and Helmberger, 2003; Ritsema et al., 1998, 1997; To et al., 2005; Wang and Wen, 2007, 2004). This cannot be explained by purely thermal effects (unless one invokes a very unusual rheology).

While there are indications that LLSVPs may be, at least in some part, compositionally distinct from the ambient mantle, the matter is far from settled with some studies arguing that not only can V_s anomalies be explained by a purely thermal origin but that compositionally varying models

consistently over predict the amplitude of observed V_s anomalies (Davies et al., 2012). The key to resolving this issue is density. When density is combined with observed velocities, results from laboratory experiments can confirm whether observed parameters are feasible via thermal variation alone, or whether they indeed necessitate compositional heterogeneity, and if so, provide constraints on composition.

As such, it is vital to offer stronger constraints on the density of regions such as LLSVPs. While there are a variety of constraints of the 1D density structure of the Earth, (e.g. absolute mass, moment of inertia) there are few observables which provide information on Earth's 3D density structure. Dynamic topography and the Earth's geoid provide non-unique constraints and require knowledge of mantle viscosity which is not well-known (Rudolph et al., 2015). Furthermore, such observations are also sensitive to the structure of the upper mantle. Meanwhile, body waves can only provide very limited information on relative density via the amplitudes of reflections at boundaries with strong impedance contrasts. Better constraints are provided by Earth's normal modes which have significant sensitivity to density through self-gravitation effects induced during their associated deformation of the Earth.

Numerous normal mode studies have attempted to resolve the density of the lower mantle (Ishii and Tromp, 1999; Resovsky and Trampert, 2003; Trampert et al., 2004a). However, some of the resulting solutions were found to be highly non-unique (Romanowicz, 2001) or overly dependent on the starting velocity model imposed (Kuo and Romanowicz, 2002). By relying on a collection of mantle modes sensitive to structure in the whole mantle, such studies also suffer from a lack of depth resolution, because the mode datasets used also have sensitivity to regions outside of the lower mantle, with the risk of mapping some of the model uncertainties in the crust and upper-mantle into structure in the region of interest.

A recent study (Koelemeijer et al., 2017) utilized a new normal mode dataset with unique sensitivity to the lowermost mantle, CMB Stoneley modes (Figure 3.2). CMB Stoneley modes, which have most of their energy trapped around the CMB, offer great sensitivity to the uppermost outer core and the lowermost mantle, where the LLSVPs are observed. Furthermore, they have little sensitivity to other depth ranges in the Earth. However, due to their lack of energy near the Earth's surface (Figure 3.2), they are only observed via coupling, primarily to nearby fundamental modes. As a result, the coupling theory used in their analysis becomes especially important. Thus far Stoneley modes have only been used in the context of splitting functions, accounting only for coupling between the Stoneley mode and nearby fundamental mode (i.e. ${}_1S_{11}$-${}_0S_{15}$ and ${}_1S_{12}$-${}_0S_{17}$). Such truncated theory is known to introduce significant error in other modes (Akbarashrafi et al., 2018; Al-Attar et al., 2012) while the effect on Stoneley modes has never been fully explored.

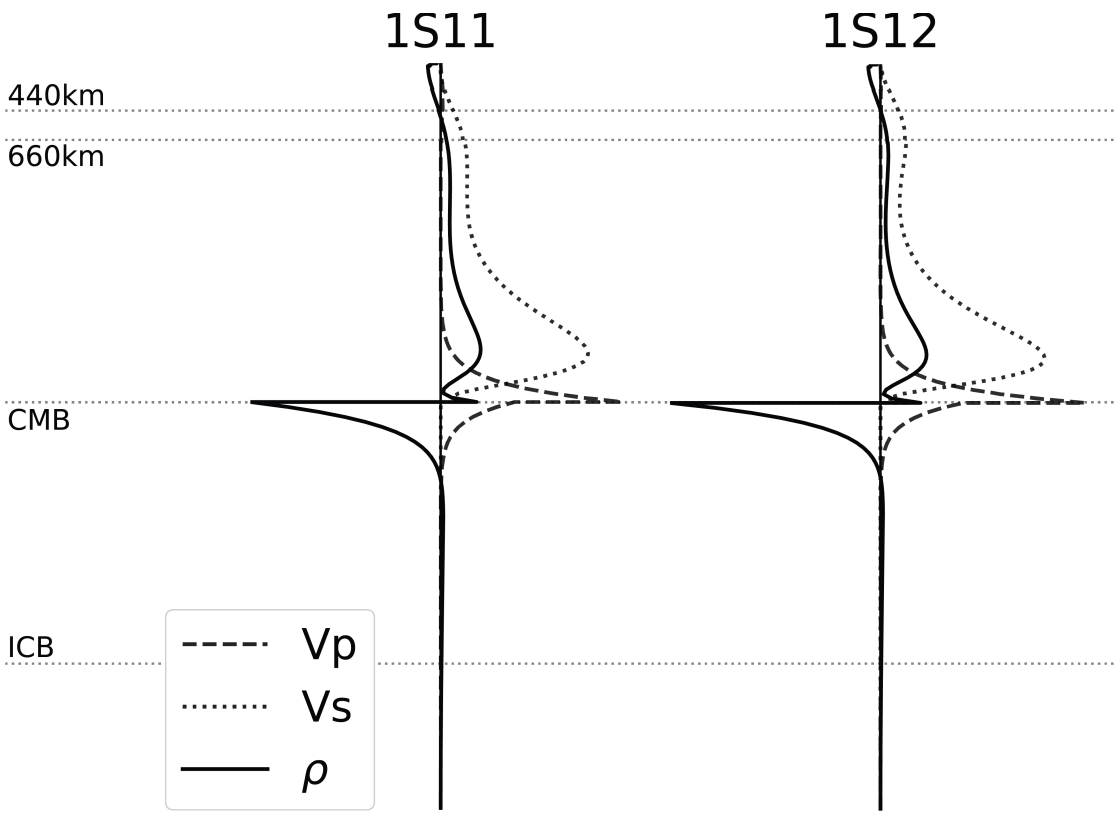

Figure 3.2: **Spherically symmetric sensitivity kernels** for isotropic V_p, V_s, and density (ρ) as a function of depth, computed in the radially anisotropic Preliminary Reference Earth Model (PREM) (Dziewonski and Anderson, 1981) for Stoneley modes 1S11 and 1S12. The y-axis indicates depth with major discontinuities marked by a horizontal dotted line, while the x-axis is the modes' normalized sensitivity. Note the lack of sensitivity in the upper mantle and below the uppermost outer core.

Unfortunately, the expression of Stoneley modes is expected to be of relatively low amplitude and the signal of density structure within that is likely even smaller. To further complicate the use of Stoneley modes to infer deep mantle density structure, additional uncertainty in computations is added via other *a-priori* choices in inputs, such as the choice of whole mantle velocity model, earthquake source parameters, attenuation model, and assumed CMB topography. Herein, we use fully coupled synthetics as a reference to assess the error on the amplitude spectra introduced by various levels of truncated coupling theory. We also assess the magnitude of these errors due to the uncertainties introduced by the above choices (velocity model, etc.). Finally, we visually and statistically compare the magnitude of all these effects against the magnitude of the signal generated by conceptual models of LLSVP density. We conclude that (1) Stoneley modes can indeed offer strong constraints on LLSVP density; (2) the use of pair-of-mode coupling theory introduces significant errors, often larger than the signal being studied; and (3) in order to better resolve the strength and spatial extent of density anomalies, improved models of mantle velocity structure must be constructed.

Methodology

Utilizing the normal mode full-coupling code of Yang and Tromp (2015) synthetic spectra for Stoneley modes ${}_1S_{11}$ and ${}_1S_{12}$ are generated. This is first performed for the reference case, computed in the seismic tomographic model S40RTS (Ritsema et al., 2011) using full-coupling theory up to 3.1 mHz. For this reference case, we impose a purely thermal density scaling ($\ln\rho/\ln V_s$ = 0.3 as per Ritsema et al., 1999), no CMB topography, the attenuation model QL6 (Durek and Ekström, 1996), and we use the Harvard CMT source solution (Ekström et al., 2012). These reference spectra and all others presented, are computed for the May 24th, 2013 Sea of Okhotsk (Mw 8.3) deep earthquake (~598 km) at 151 broadband Streckeisen STS-1 stations. Both the event and stations selected would be well-suited for use in an observation-based study.

Next, a variety of synthetics are generated to explore the effects of changing individual parameters within each simulation. We first explore the effects of progressively truncating the coupling theory used. Second, we apply full-coupling theory and tested the effect of: (1) using a different 3D mantle model; (2) choosing another source solution (3) adding CMB topography; and (4) changing the 1D attenuation model. Finally, we generate full-coupled synthetics for a selection of conceptual models for proposed LLSVP density structures.

Residuals between the resulting spectra and the reference spectra are then computed for each varied parameter. The integral under the absolute value of these residual is calculated as a percentage of the integral under the reference spectra. This provides a numerical measure that assesses the error introduced by each *a-priori* assumption with respect to the reference spectra.

Theory

Firstly, we explore the effects of different levels of coupling theory to assess the degree of coupling required to balance accuracy and speed. Full-coupling to 3.1 mHz is considered the ground-truth, coupling a total of 122 modes for the reference spectra, ensuring coupling to a minimum of all modes within 0.5 mHz of each Stoneley mode's center frequency. The width of the coupled frequency band around the Stoneley mode being studied is then progressively shrunk to ±0.5 mHz (60 and 61 modes for ${}_1S_{11}$ and ${}_1S_{12,}$ respectively), ±0.1 mHz (14 and 12 modes), and finally pair-of-mode coupling (2 modes) (Figure 3.3).

Mantle velocity model

SP12RTS (Koelemeijer et al., 2016) is chosen as the alternative velocity model. Differences between SP12RTS and the reference model (S40RTS) are small in V_s at lower-degrees (Appendix Figure B1,2) due to some similarity in the data and methods used in their construction. However, in V_p these differences are more pronounced (Appendix Figure B1,2) as, unlike S40RTS, in SP12RTS V_p was inverted for independently. As a result, in addition to exploring the effects of uncertain V_s structure, this comparison simultaneously addresses errors due to assuming constant and fixed scaling between Vp and Vs which is common in tomographic models.

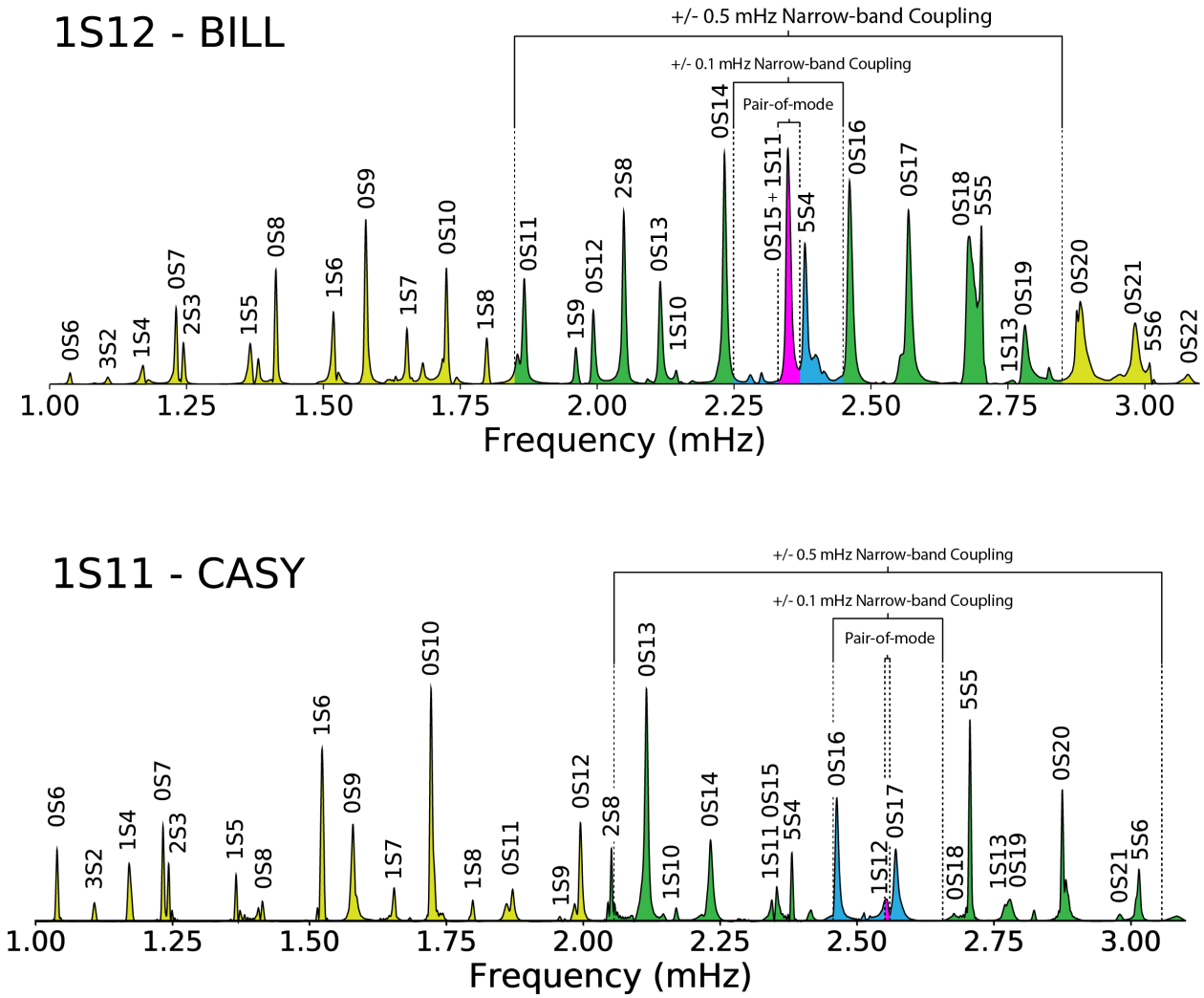

Figure 3.3: **Synthetic full-coupling spectra with differing considered coupling levels marked** for ${}_1S_{11}$ at station CASY, Casey, Antarctica and ${}_1S_{12}$ at station, BILL, Bilibino, Russia, computed for the May 24th, 2013 Sea of Okhotsk (Mw 8.3) deep earthquake (~598 km). Color bands mark the extent of the differing levels of coupling considered in this study (labelled), while the list of labelled modes is non-exhaustive, only indicating some of the more prominent modes expressed.

Source

In addition to our reference Harvard CMT source solution (Ekström et al., 2012) we test that of the US Geological Survey (USGS, 2013) and another published solution (E35; Abubakirov et al., 2015). The two former solutions are broadly similar in their construction, both utilizing teleseismic body waves alongside intermediate to long-period surface waves to compute a centroid moment tensor. Meanwhile, E35 is computed using only regional waveforms (epicentral distance 8°–25°) between 125–250 s. For exact source parameters see Appendix Table B1.

CMB topography

In the absence of a consensus on CMB topography (Koelemeijer, 2020), we opt to invoke dynamical arguments and generate a conceptual model. We require that the spatial pattern of the topography matches that of density at the base of the mantle (Appendix Figure B1,2) using a linear

scaling factor. This assumes that a buoyant lowermost mantle will rise, resulting in an upward deflection of the CMB and that the reverse is true for dense regions This scaling is defined such that the largest absolute amplitude of topography is ±3 km, and so consistent with observations of topography at long wavelengths (Koelemeijer, 2020). We apply this scaling factor to our reference case, S40RTS, to generate the topography explored here (Appendix Figure B3).

Attenuation structure

In addition to the reference attenuation model, QL6 (Durek and Ekström, 1996), we test QM1 (Widmer et al., 1991) and the Q structure of PREM (Dziewonski and Anderson, 1981), representing the most commonly utilized radial attenuation models, all of which are broadly consistent (e.g. Cammarano and Romanowicz, 2008)(Appendix Figure B4).

LLSVP density

The reference model (S40RTS) can be thought of as a purely thermal, buoyant LLSVP density model, with reductions in V_s mapped to reductions in density. As such, the LLSVPs of our reference model represent regions of thermal upwelling. In addition to this thermal reference case, we also explore two additional models of LLSVP density: (1) a dense LLSVP model, "Dense Tall", and (2) a buoyant, thermal LLSVP model with a ~100 km thick, dense base – "100km Dense". These models are identical to the reference model starting 600 km and 100 km above the CMB for "Dense Tall" and "100km Dense", respectively. Below these heights the -0.65% lnVs contour is used to define the LLSVP (Torsvik et al., 2006; L2017). Within the LLSVP, density is scaled via a scaling factor determined such that the total excess mass of Lau et al.'s (2017) preferred model is contained within the LLSVP. Meanwhile density outside the LLSVPs is defined by a balancing scaling factor to ensure mass is conserved in this depth range.

Results

Coupling modes within ±0.5 mHz generally introduced negligible error in the context of other uncertainties (Figures 3.3 and 3.4; Table 3.1). Even the truncated ±0.1mHz narrow-band coupling (14 and 12 modes for 1S11 and 1S12, respectively) results in relatively accurate spectra. Meanwhile, Pair-of-mode coupling consistently produces significant inaccuracies (Figures 3.3 and 3.4). Figures 3.4 and 3.5 clearly illustrate this trend for increasing errors as the level of coupling decreases, while Table 3.1 shows this trend is broadly consistent across all stations and both modes.

Aside from pair-of-mode coupling, the largest source of discrepancy among those explored is the choice of velocity model (Orange, Figures 3.4 and 3.5), with the use SP12RTS representing a median uncertainty of ~23% (Table 3.1). Perhaps expected given the known differences between the model structure (Appendix Figure B1,2). Meanwhile, differences due to the choice of attenuation model and the addition of CMB topography were very small, and likely negligible in the context of other uncertainties.

The uncertainty due to the source varies significantly between station to station (Figure 3.6). For example, in Figure 3.4 the amplitude of error due to the Abubakirov et. al. solution is ~16% and greater than that of the USGS solution (~11%), while in Figure 3.5, the error associated with Abubakirov et. al.'s source is ~4% while the USGS source now has the larger error (~9%). Overall, the USGS source produces a significantly smaller difference from the reference CMT source than that of Abubakirov et. al. (2015). The similarity between the USGS and Harvard CMT synthetic spectra is likely due to the similar methodologies and datasets used to construct the source

solutions. Each used both short-period body waves and intermediate-period surface waves from teleseismic records. Meanwhile, Abubakirov et al.'s E35 solution is computed using only regional waveforms between 125–250 s. The exact differences in source solutions can be seen in (Appendix Table B1).

Finally, the signal due to a very dense 100 km basal layer within the LLSVPs has the overall smallest effect (Table 3.1), implying that it is unlikely to be resolvable given the current magnitude of other uncertainties. This can be visualized in Figures 3.3 and 3.4 where the associated signal is <2% in both cases. Meanwhile, a tall (~600 km) dense LLSVP produces a strong signal which is likely resolvable in the context of a carefully selected mantle model and full-coupling theory.

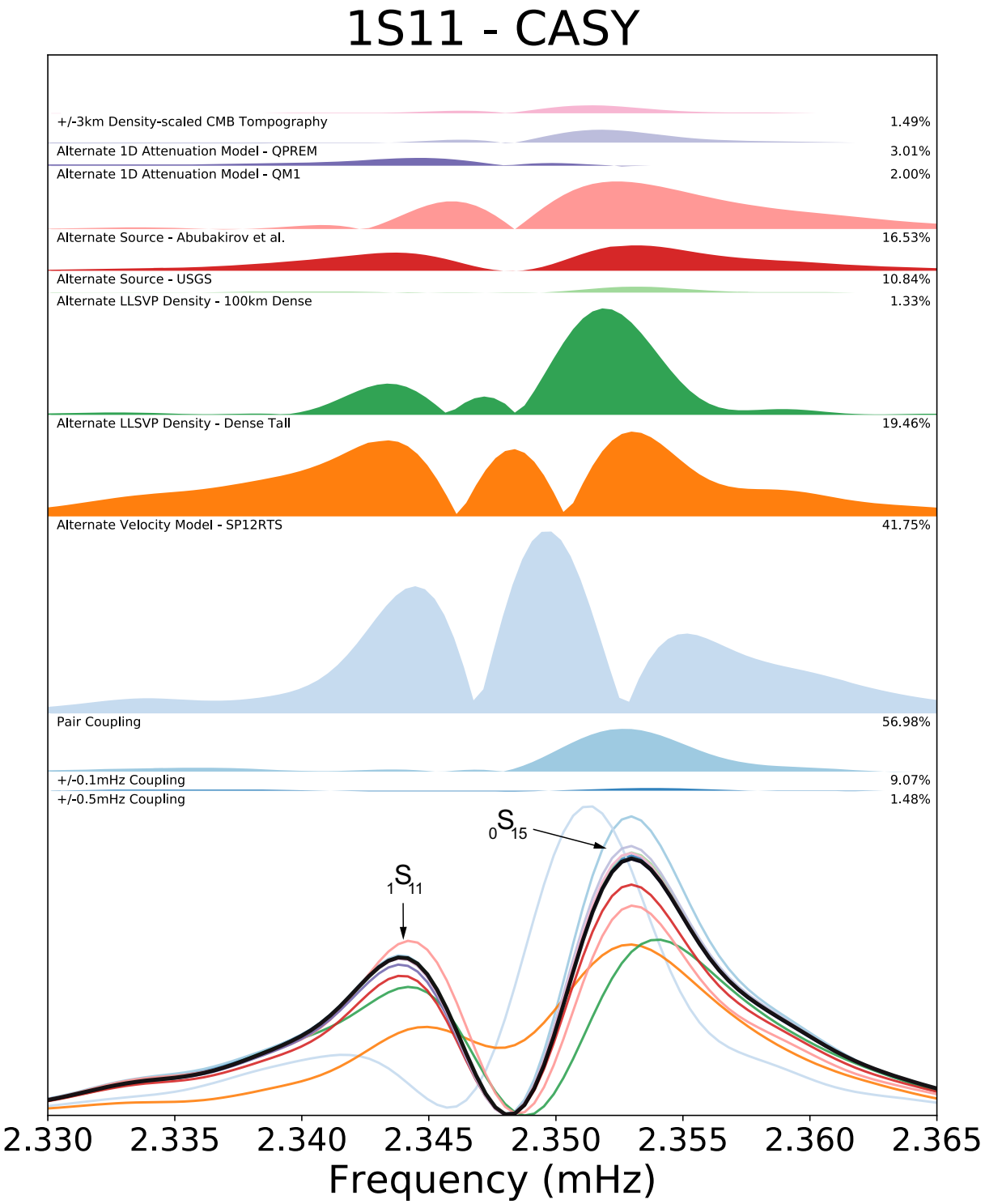

Figure 3.4: **Example Stoneley mode spectra and residuals** a comparison of test cases to the full-coupling ground truth (black line) for ${}_1S_{11}$ at station CASY, Casey, Antarctica. Other synthetics are shown, while absolute values of the residual between each test and the ground truth are shown filled, with a label and a percentage describing the integral under the absolute residual relative to that of the ground truth. For more examples see Appendix figures B5-10.

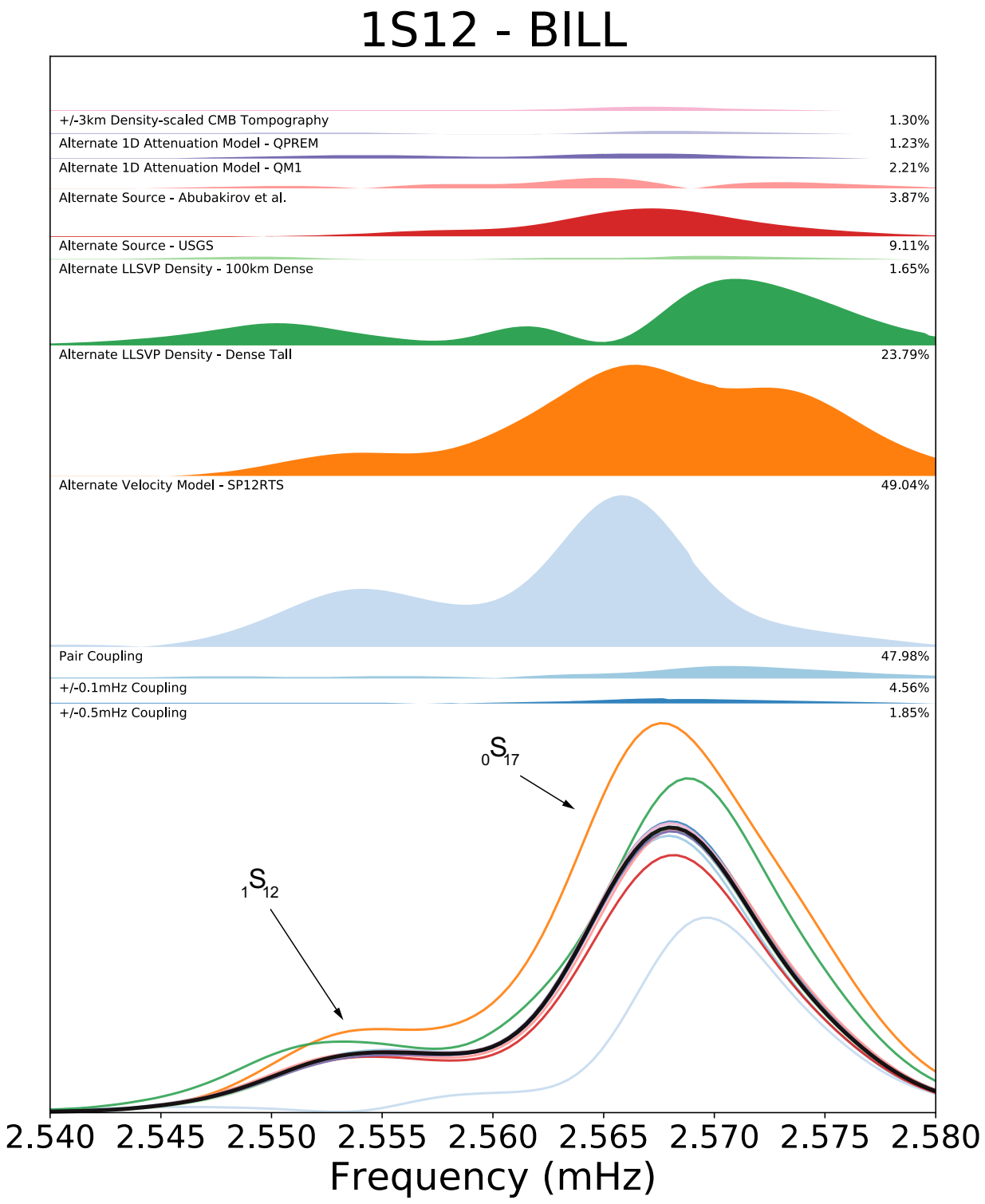

Figure 3.5: **Example Stoneley mode spectra and residuals** a comparison of test cases to the full-coupling ground truth (black line) for $_1S_{12}$ at station BILL, Bilibino, Russia. Other synthetics are shown, while absolute values of the residual between each test and the ground truth are shown filled, with label and a percentage describing the integral under the absolute residual relative to that of the ground truth. For more examples see Appendix figures B5-10.

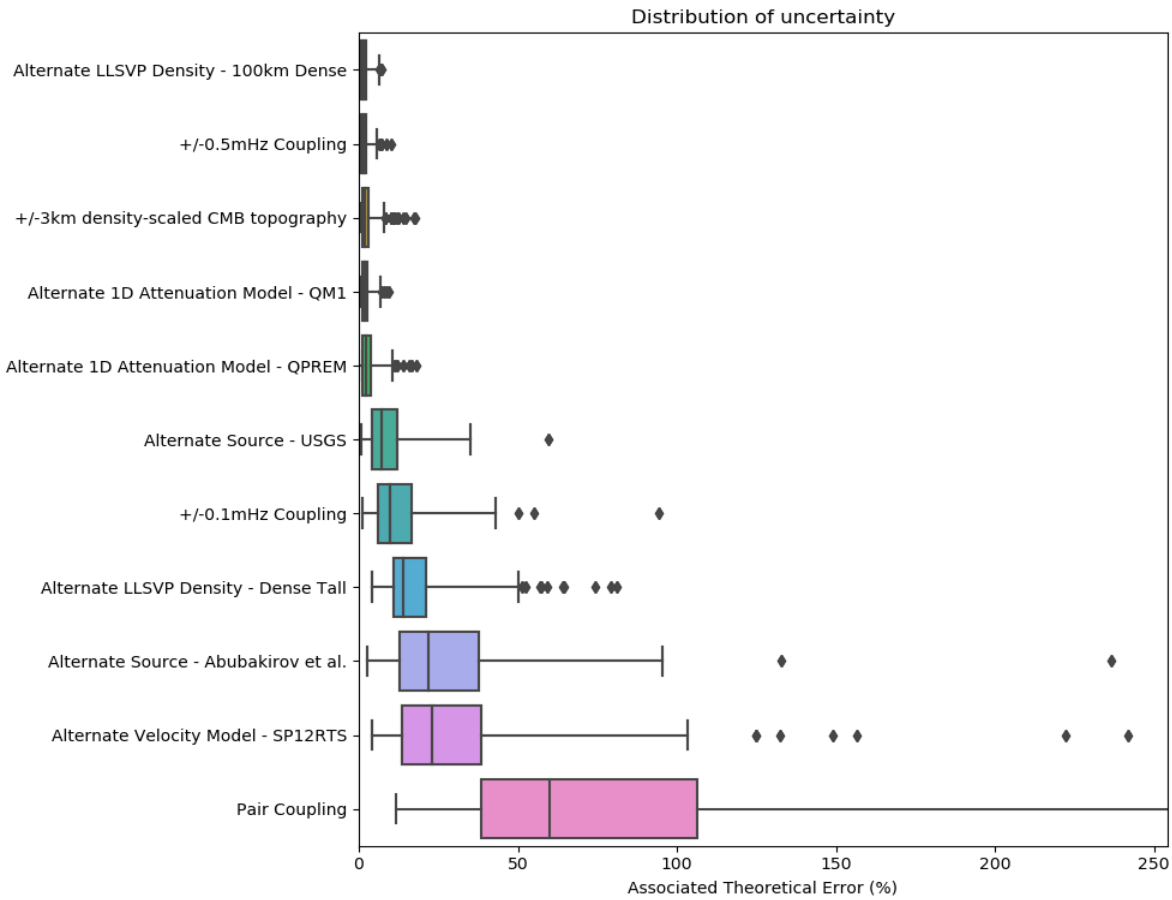

Figure 3.6 | **Box and whisker diagram of the distribution of residuals** associated with each test case. Diamonds are outliers greater than five interquartile ranges from the median value. The full range of the pair-of-mode coupling values is truncated too improve readability – the original full plot can be found in the appendix B11.

Name	Changed property	Median Uncertainty (%)	Mean Uncertainty (%)
Alternate LLSVP Density - 100km Dense	LLSVP Density	1.34	1.72
+/-0.5mHz Coupling	Coupling	1.45	1.83
+/-3km density-scaled CMB topography	CMB Topography	1.87	2.62
Alternate 1D Attenuation Model - QM1	Attenuation Model	2.03	2.19
Alternate 1D Attenuation Model - QPREM	Attenuation Model	2.33	2.97
Alternate Source - USGS	Source Solution	7.00	9.01
+/-0.1mHz Coupling	Coupling	9.78	12.79
Alternate LLSVP Density - Dense Tall	LLSVP Density	13.93	18.01
Alternate Source - Abubakirov et al.	Source Solution	21.96	28.99
Alternate Velocity Model - SP12RTS	Velocity Model	23.14	31.50
Pair Coupling	Coupling	60.05	99.02

Table 3.1: **Magnitude of effects** the mean and median values of normalized absolute residuals.

Discussion

The synthetic Stoneley mode spectra explored for the May 24th, 2013 Sea of Okhotsk (Mw 8.3) deep earthquake (~598 km) demonstrate that pair-of-mode coupling theory introduces significant errors, with a median residual of ~60% across all 302 spectra. This finding is in agreement with other recent studies focused on mantle modes (Akbarashrafi et al., 2018; Al-Attar et al., 2012). The error found here for pair-of-mode coupling (~60%) is significantly larger than the signal of the lower mantle density structures explored. The change from a purely thermal LLSVP (reference case), to a ~600 km tall, dense LLSVP ("Dense Tall") only produced a signal which was on average (median) one quarter the size (~14%) of the theoretical error introduced by pair-of-mode coupling. This implies one should avoid the use of splitting functions for Stoneley mode studies of LLSVP density (such as in Koelemeijer et al., 2017). However, we do note that in principle splitting functions may still be useful if constructed using coupling theory involving a larger bandwidth than is currently employed, with results suggesting that simply coupling modes ±0.1 mHz from the mode of interest decreases median residual theoretical error to around 10%. Ultimately, full-coupling theory is preferable and would be utilized in future Stoneley mode studies to further minimize errors and maximize the resolvability of density structure.

Most important aside from the level of coupling theory used was the choice of mantle model, with SP12RTS exhibiting a median error of ~23%, of similar order to that associated with the signal of a tall dense LLSVP. As a result, in future studies we suggest that multiple models might be explored to assess the robustness of results and their dependence on the chosen mantle model. In addition, it is clear that the pursuit of improved mantle models is ultimately necessary to further resolve the amplitude and spatial distribution of any non-thermal density heterogeneity in the mantle (and indeed the uppermost outer core). With this goal in mind, scaling factors should be avoided such that V_p, V_s, and density are simultaneously and independently inverted for (Moulik and Ekström, 2016).

Errors due to the chosen source solution are also significant. The median error associated with the solution of Abubakirov et al. (2015) is significant (~21%) and is approximately three times that of using the USGS solution (~7%). This is as expected given the similarities between the USGS solution and the CMT reference case, and the significant difference between the reference case and the Abubakirov et al. (2015) solution. We also note that Abubakirov et al.'s solution is available specifically for this event, and generally most studies would utilize one of the former, which appear to be able to be used interchangeably without introducing prohibitive amounts of error (median ~7%). However, a study across a larger number of events would be necessary to confirm this.

Other sources of error can be treated as negligible in the context of other effects, such as using different attenuation models and the introduction of CMB topography, all with median residuals of <2.5%. The former may be expected due the similarities between radial attenuation models. However, the small effect of CMB topography is more noteworthy, given its seemingly important role as a parameter in a recent Stoneley mode splitting function study (Koelemeijer et al., 2017).

Meanwhile, we ackowledge that all parameters explored in some cases exhibited very large uncertainties (Figure 3.6). However, upon further investigation, these high uncertainties are associated with the spectra with the low amplitudes (Appendix Figure B12). This implies these anomalously high uncertainties are likely large due to the low ampltude signal of the mode itself.

Therefore, if only spectra with large amplitudes are selected, one might expect that the values presented here for median and especially mean errors (%) are upper limit estimates.

Overall, Stoneley modes do indeed show much promise for isolating and constraining density structure adjacent to the CMB. In particular, this study has shown that if a sufficient level of coupling theory is employed, and a mantle model carefully chosen, the signal of lower mantle density structure should be sufficiently strong to be resolved, if it extends high enough above the CMB. However, we note that Stoneley modes are effectively insensitive to structure in the lowermost 100 km (See "Alternate LLSVP Density – 100km Dense", Table 3.1).

Finally, while we have not directly explored the signal of the uppermost outer core distinct region – the so-called E' layer. We note that Stoneley modes have a significantly higher sensitivity to the density structure in this region than in the lowermost mantle (Figure 3.2). Several seismic studies (e.g. Lay and Young, 1990; Souriau and Poupinet, 1991; Kohler and Tanimoto, 1992; Garnero et al., 1993b; Tanaka and Hamaguchi, 1993b, 1993a; Tanaka, 2007; Helffrich and Kaneshima, 2013, 2010; Kaneshima and Matsuzawa, 2015; Tang et al., 2015; Irving et al., 2018; Kaneshima, 2018; van Tent et al., 2020; Wu and Irving, 2020) and geomagnetic studies (Buffett, 2014; Lesur et al., 2015; Whaler, 1980) have proposed that the E' layer is ~100 km thick and of lower velocity that the bulk outer core (Brodholt and Badro, 2017). The relatively low density of this layer that sits at the top of the liquid outer core suggests that it may be chemically distinct from the bulk outer core, with a higher concentration of light elements lowering its density (Brodholt and Badro, 2017; Buffett and Seagle, 2010). However, *ab-initio* studies predict that a concentration of light elements would result in increased seismic velocities, opposite to what is observed. As a result, understanding the nature of E' is highly dependent on strong observational constraints on its density, which are currently lacking. Therefore, we propose future normal mode and other studies should aim to simultaneously resolve the density structure of both the lower mantle and E' layer, since (1) the sensitivity of Stoneley modes to density in both of these regions will lead to non-uniqueness in any effort to determine deep mantle density, and (2) the resulting constraints on E' are independently highly valuable to the study of the deep Earth and more broadly, rocky planet cores.

Conclusions

To explore the potential of new observations of core-mantle boundary Stoneley modes in the study of deep mantle density structure, synthetic tests were performed to assess their sensitivity to various theoretical approximations and mantle structure. For the former, we constrain the magnitude of errors introduced in the computation of Stoneley mode spectra via different levels of coupling theory, including the errors associated with the pair-of-mode coupling theory used in the generation of Stoneley mode splitting functions (Koelemeijer et al., 2013). In regard to the latter, we compare the magnitude of errors that may be introduced in the prediction of Stoneley mode spectra from *a-priori* inputs such as 3D mantle structure, source solution, CMB topography, and radial attenuation model.

We conclude that significant theoretical error is introduced by truncated theory, especially the pair-of-mode coupling theory commonly applied in the generation of splitting functions. Additionally, to better resolve the amplitude and spatial distribution of any chemical heterogeneity, we conclude that it is highly important that new, more accurate mantle models be constructed, with particular emphasis on independently constraining V_p, V_s, and density.

Finally, it is our belief that Stoneley modes show much promise for resolving key questions around a chemically distinct layer proposed at the top of the outer core (E'), and recognize that in order to accurately determine density anomalies on either side of the CMB, it is important that parameters both sides of the CMB are considered simultaneously in future Stoneley mode studies.

Chapter 4

Determining LLSVP density: reconciling Stoneley modes and Earth tides

A version of this chapter is in preparation for publication in Geophysical Journal International

Introduction

The presence of two, large, antipodal low wave-speed structures at the base of Earth's mantle beneath Africa and the Pacific Ocean was first observed in seismic tomography over 30 years ago (Dziewonski, 1984). The existence of these two "large low shear velocity provinces" (LLSVPs) has subsequently proven robust, consistently observed using a variety of datasets and methodologies (e.g. Lekic et al., 2012). With a shear wave-speed (V_s) reduction reaching 2-3%, these LLSVPs cover roughly one quarter--- of the core-mantle boundary's (CMB) surface area, and in some models, extend ~1000 km above the CMB. However, their origin, detailed morphology, stability over time, composition, and role in mantle circulation, remain open questions (e.g. Forte and Mitrovica, 2001; Mulyukova et al., 2015; Zhong and Rudolph, 2015). In order to answer these questions, it is important to determine their density relative to ambient mantle, a topic of lively debate (e.g. Forte and Mitrovica, 2001; Ishii and Tromp, 1999; Koelemeijer et al., 2017; Kuo and Romanowicz, 2002; Lau et al., 2017). Some studies favor wave-speed reductions due to increased temperatures alone, while others suggest that the presence of compositionally distinct material plays a role (e.g. McNamara, 2019).

Despite being crucial for determining whether the LLSVPs are dominantly thermal or thermo-chemical in nature, resolving their density via seismological observations remains difficult. With the exception of reflection at impedance contrasts, body waves offer little sensitivity, making longer-period normal modes the best tool to resolve the density structure of the deep mantle. Over 20 years ago, Ishii and Tromp (1999) first utilized this sensitivity in combination with free-air gravity constraints, inverting for seismic wave-speeds and density, proposing a density increase of a few percent within the LLSVPs. Shortly after, Romanowicz (2001) showed that the result of this inversion was highly non-unique and heavily dependent on the initial wave-speed model (Kuo and Romanowicz, 2002). Subsequent studies utilized probabilistic forward modelling approaches, again finding that normal mode observations favored an increase in density within the LLSVPs

(Resovsky and Trampert, 2003; Trampert et al., 2004b). Recent splitting measurements of ${}_0S_2$ show significantly smaller splitting compared to that expected from the well constrained Vs structure (Moulik and Ekström, 2016). These authors showed that this could be explained by anticorrelation between Vs and density, and therefore excess density within the LLSVPs. A variety of recent tomographic models generated to fit seismic observations and/or geodynamical constraints have also favored LLSVPs with increased densities, though the height, extent, and magnitude of the density excess vary (Mosca et al., 2012; Moulik and Ekström, 2014; Simmons et al., 2010; Yu et al., 2020).

Meanwhile, some geodynamical studies have disputed the view of LLSVPs as dense, compositionally distinct, stable structures. For example, Davies et al. (2012) generated a variety of thermal and thermo-chemical mantle convection models and concluded that purely thermal, buoyant, LLSVP models were sufficient to explain travel times of teleseismic S waves, while thermo-chemical LLSVPs regularly over-predicted deep mantle shear wave-speed anomalies.

Recently, Koelemeijer et al. (2017) (hereafter, K2017) utilized new splitting function measurements of CMB Stoneley modes, a group of modes whose sensitivity is uniquely focused around the CMB. A model-space search explored V_s-to-density scaling factors within the LLSVPs, as well as the amplitude and sign of CMB topography. The authors reported two groups of equally well-fitting models: one group, favoring dense LLSVPs, and the other, favoring buoyant ones. The buoyant LLSVP models were preferred due to dynamical arguments about the sign of the associated underlying CMB topography. Meanwhile, Lau et al. (2017) (hereafter, L2017) utilized GPS measurements of Earth's body tides for the first time, performing a similar model-space search for a V_s-to-density scaling factor within the LLSVPs, finding best-fitting models required a density excess.

While there are small differences between the Stoneley mode and body tide approaches (e.g., the background tomography model, details of LLSVP discretization), these seemingly contrasting results have raised questions about the current resolvability of deep mantle density structure. However, these two datasets have distinct sensitivity to lowermost mantle structure. The body tides sensitivity to density in the lower mantle (similar to that of the gravest normal mode, ${}_0S_2$) monotonically increases with depth toward the CMB. Meanwhile, all the Stoneley modes have maximum sensitivity to density ~300 kilometers above the CMB, with sensitivity decreasing significantly in the last 200 km of the mantle, i.e., a 'blind spot' for density (Appendix Figure - C1). Additionally, Stoneley modes have significant sensitivity to the density structure of the uppermost outer core, where tides have no sensitivity. Therefore, the results of K2017 and L2017 need not be incompatible. It has been suggested that, in particular, these datasets may be reconciled by a model of LLSVPs in which a dense basal structure, no more than ~200 km thick, is overlain by a buoyant thermal structure, perhaps in the form of bundled plumes (Romanowicz, 2017).

Such a dense basal layer (DBL) had been proposed over 20 years ago as a mechanism to stabilize the position of upwelling domes and plumes in laboratory experiments (Davaille, 1999; Jellinek and Manga, 2002). Other observational constraints may also point toward a DBL model of LLSVPs. Via dynamical simulations Jones et al. (2019) demonstrated that in order to satisfy observed Tungsten-isotopic differences between large igneous provinces (interpreted as originating from plume heads), and ocean island basalts (interpreted as originating from plume tails), a compositionally distinct, dense reservoir in the lowermost mantle is required. In particular, such a reservoir had to be restricted to the bottom 200 km of the mantle. Moreover, it has been

shown that ultra-low-velocity-zones (ULVZs), regions characterized by extreme reductions in shear wave-speeds reaching ~30% (e.g. Garnero and Helmberger, 1998), are preferentially found within LLSVPs or at their boundaries (Yu and Garnero, 2018) and may require density anomalies in excess of ~10% to explain (Rost et al., 2005).

Here, we show that body tide and Stoneley mode observations can indeed be reconciled by a DBL LLSVP model by generating conceptual mantle models in which only LLSVP density structure varies. These models are analyzed against both K2017 and L2017's datasets following the original procedures. Additionally, they are tested against a new set of observed Stoneley mode spectra, generated using wide-band coupling theory (using the code of Yang and Tromp, 2015) as opposed to the self-coupling, or pair-coupling theory used in the construction of K2017's splitting functions. We conclude that, within statistical significance, a model of LLSVP density, characterized by a dense, thermo-chemical, basal layer, overlain by a purely thermal structure, while accompanied by elevated CMB topography, is able to reconcile all three datasets, providing a consistent view of LLSVP density structure.

Methods

We construct four conceptual models of LLSVP density structure (Figure 4.1): (1) a purely thermal, buoyant, LLSVP model ("light" LLSVP; "L-LLSVP"), (2) a tall, dense, thermo-chemical LLSVP model ("D-LLSVP"), and (3,4) two thermal LLSVP models with DBLs ("DBL100km" and "DBL200km"). All four models are constructed with the V_s structure of S40RTS (Ritsema et al., 2011), with compressional wave-speeds (V_p) scaled by $\ln V_p/\ln V_s=0.5$ (Ritsema et al., 1999). The four models differ only in their density structure in the bottom 600 km above the CMB and are otherwise defined and parameterized identically. Density above any prescribed dense LLSVP region is scaled by S40RTS's original, purely thermal scaling factor of $\ln/\ln V_s=0.3$ (Figure 4.1a).

For the thermal model, L-LLSVP, the density structure is scaled uniformly everywhere by the purely thermal scaling factor, with a DBL height, h, of 0 km (Figure 4.1b). Meanwhile, in D-LLSVP, the total excess mass within the LLSVP of L2017's mean model (see Figure 4.4 of L2017) is distributed evenly throughout both LLSVPs via a uniform scaling factor, R_{LLSVP}, extending vertically upward to 600 km above the CMB (i.e., for D-LLSVP, h = 600 km). This excess mass is balanced by a scaling factor outside of the LLSVPs at the same depths, R_{OUT}, ensuring that the total mass in this depth range is conserved. The extent of the LLSVP is defined by the -0.65% $\ln V_s$ contour (Torsvik et al., 2006; L2017). For DBL100km and DBL200km, the same procedure is followed but with dense layer heights of 100 and 200 km respectively, concentrating the total excess mass from L2017's mean model into a narrower depth range (see Figure 4.1c-e).

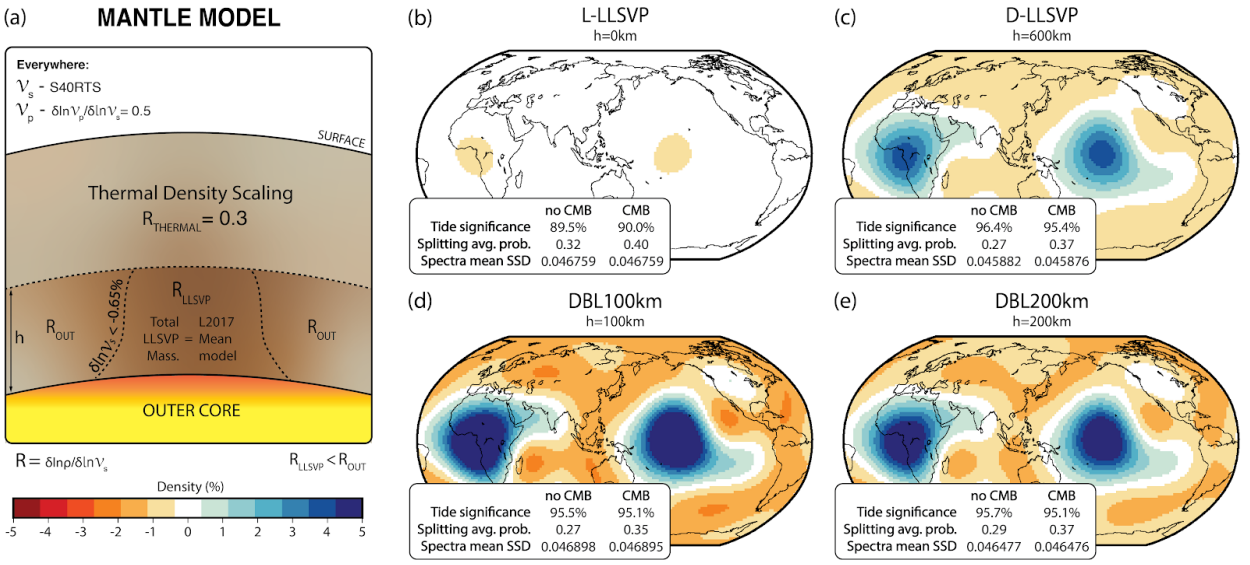

Figure 4.1 | Model cartoon and density maps. (**a**) Conceptual illustration of model construction (**b-e**) The density structure of each model at 50km above the CMB and the associated assessment metrics for each dataset in this study (see Table C1 in appendix for more information). Note, probabilities were calculated independently for spherical harmonic degrees 2, 4, and 6 as in K2017 and then combined in a weighted average using the number of splitting coefficients for each degree.

We assess these four models against three different observational datasets: (1) Stoneley mode splitting functions used by K2017, (2) body tide observations from L2017, and (3) a new dataset of observed Stoneley mode spectra.

Stoneley mode splitting functions

First, each model was assessed against the original Stoneley mode splitting functions (Koelemeijer et al., 2013), following the methodology of K2017. For each model, synthetic splitting functions were computed (Figure 4.2), and the probability that the splitting function measurements were optimally fit within their uncertainties was determined.

Second, given the trade-offs between deep mantle structure and CMB topography, we searched for a best-fitting CMB-topography associated with each density model. As in K2017, the spatial pattern of CMB topography followed the spatial pattern of density anomaly of each model with a scaling factor invoked. A grid search of this scaling factor was performed for each spherical harmonic degree and a most probable CMB topography model was constructed for each model (Appendix Figure C2) (See K2017 for further details).

Earth's body tides

We used the same GPS-derived measurements of the vertical body tide displacement, Δu, as in L2017 (Yuan et al., 2013; Figure 4.3d-g). We compared this to the synthetic responses predicted for each density model, and as per the original study, a confidence level was computed, describing the confidence that the model prediction improves the correlation to observations relative to calculations without 3D structure (See L2017 for further details). This process was performed for each density model, both with and without their associated best-fitting CMB topographies determined by the splitting functions, as discussed above.

Stoneley mode spectra

The dataset of Stoneley mode spectra used for the first time in this study was compiled from broadband vertical component seismograms for the May 24th, 2013 Sea of Okhotsk deep earthquake (Mw 8.3). This event provides excellent signal-to-noise ratio, while its depth (~598 km) provides favorable conditions for observing modes sensitive to deep mantle structure. Additionally, the absence of other large events in the following days makes comparisons to synthetics easier to interpret. Two points to note are that (1), this event provides a completely independent dataset relative to the splitting function measurements, as it is one of only a few suitable events that were not included in their construction; and (2), the construction of splitting functions is subject to assumptions and processing steps that may reduce the ability to make firm conclusions about density structure (Chapter 3, Akbarashrafi et al., 2018; Al-Attar et al., 2012). For more details on the data collection and processing see Appendix C3.

To address concerns about the validity of the isolated-mode/pair-of-modes coupling theory used in the development of splitting functions (Deuss and Woodhouse, 2001; Yang and Tromp, 2015), we generated either full-coupling or wide-band synthetic spectra (using the code of Yang and Tromp, 2015). After initial tests confirmed the presence of Stoneley modes in the observed spectra (Appendix Figure - C7), full-coupling synthetics were calculated up to a truncation frequency of 3.1 mHz and used for assessing the Stoneley modes within this frequency band: $_1S_{11}$, $_1S_{12}$, $_1S_{13}$ and $_1S_{14}$. Meanwhile, due to computational limitations, spectra for Stoneley modes $_2S_{15}$, $_2S_{16}$, $_2S_{17}$ were computed using wide-band coupling between 3.1 and 3.8 mHz, accounting for cross-coupling between 61 different modes, while spectra for modes $_2S_{25}$ and $_3S_{26}$ (also used in K2017) were not computed.

The overall ability of each LLSVP density model to explain observed Stoneley mode spectra was assessed via the mean sum of squared difference between the predicted and observed amplitude spectra across all (170) station-mode pairs.

Results

Although the purely thermal model (L-LLSVP) has the highest probability for the splitting function data, all four models have similar probabilities (Figure 4.1). In particular, the pattern of splitting functions is fit well by all models (Figure 4.2), though for the dense models the fit to amplitude is improved by including best-fitting CMB topography. In all cases, the CMB is deflected upward below the LLSVPs (Appendix Figure - C2) with maximum/minimum amplitudes of +13/-6, +11/-3, and +8/-2 km for models D-LLSVP, DBL200km, and DBL100km, respectively. As in K2017, one might discount the tall, dense D-LLSVP model on the basis that its best-fitting CMB topography is positive underneath the LLSVP regions. This seems dynamically implausible given the excess density extending for 600 km above the CMB. While the DBL models also have a positive CMB topography beneath the LLSVPs, this is more acceptable, given the small thickness of the dense layers, and the buoyant material above.

Again, similar to the original study (L2017), body tide observations do not favor a purely thermal LLSVP model (L-LLSVP) but are well-explained by the tall, dense model (D-LLSVP), with a significance level of over 95% - the cutoff for acceptable models in L2017 (Figure 4.1). This difference in fit can be better visualized in Figures 4.3a,b, which show the residuals between predictions and observations for each model with and without CMB topography. Both DBL models also exceed this cutoff and fit similarly well to the more evenly distributed, density excess

of D-LLSVP. This is expected given the coarse depth resolution offered by these long-wavelength data (Appendix Figure - C1). The inclusion of best-fitting CMB topography only slightly decreases significance values for the three dense models and generates modest improvement for the L-LLSVP model, though still well-below the 95% cutoff. This is in accord with the minimal sensitivity of the body tides to CMB topography (L2017).

Finally, synthetic spectra from all four models exhibit very similar fits to observations (Figures 4.4 and 4.1), both with and without the inclusion of best-fitting CMB topographies. A Kolmogorov–Smirnov test confirmed with high likelihood (>95%) that, given our available spectra, these models were statistically indistinguishable. Further, we note that the DBL models are often barely distinguishable from the purely thermal model in synthetics (Figure 4.4). This illustrates the low sensitivity of the Stoneley modes to the differing structure in the bottom 200 km of these models. However, whether the two higher-frequency Stoneley modes considered by K2017 (e.g. $_2S_{25}$, $_3S_{26}$) would show the same indifference, remains to be determined.

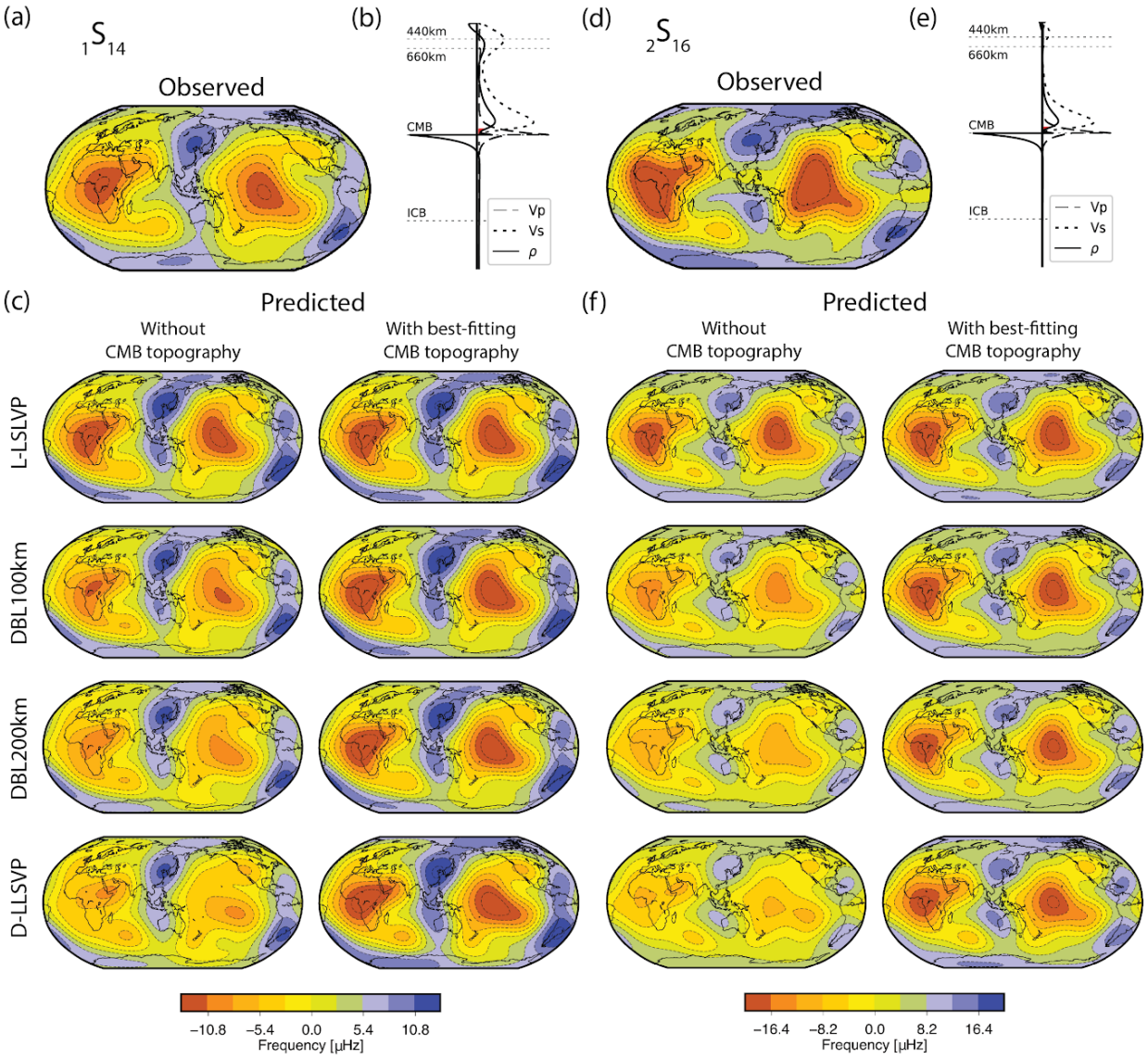

Figure 4.2 | Observed and predicted Stoneley mode splitting function maps. (**a,d**) Observed splitting for $_1S_{14}$ and $_2S_{16}$, respectively, plotted up to maximum structural degree s=6. (**b,e**) Associated sensitivity kernels for density (solid), shear wave-speed (dotted) and compressional wave-speed (dashed). The sensitivity to density in bottom 100 km of the mantle is filled red for emphasis. (**c,f**) Predicted splitting functions for each model with and without best-fitting CMB topographies included.

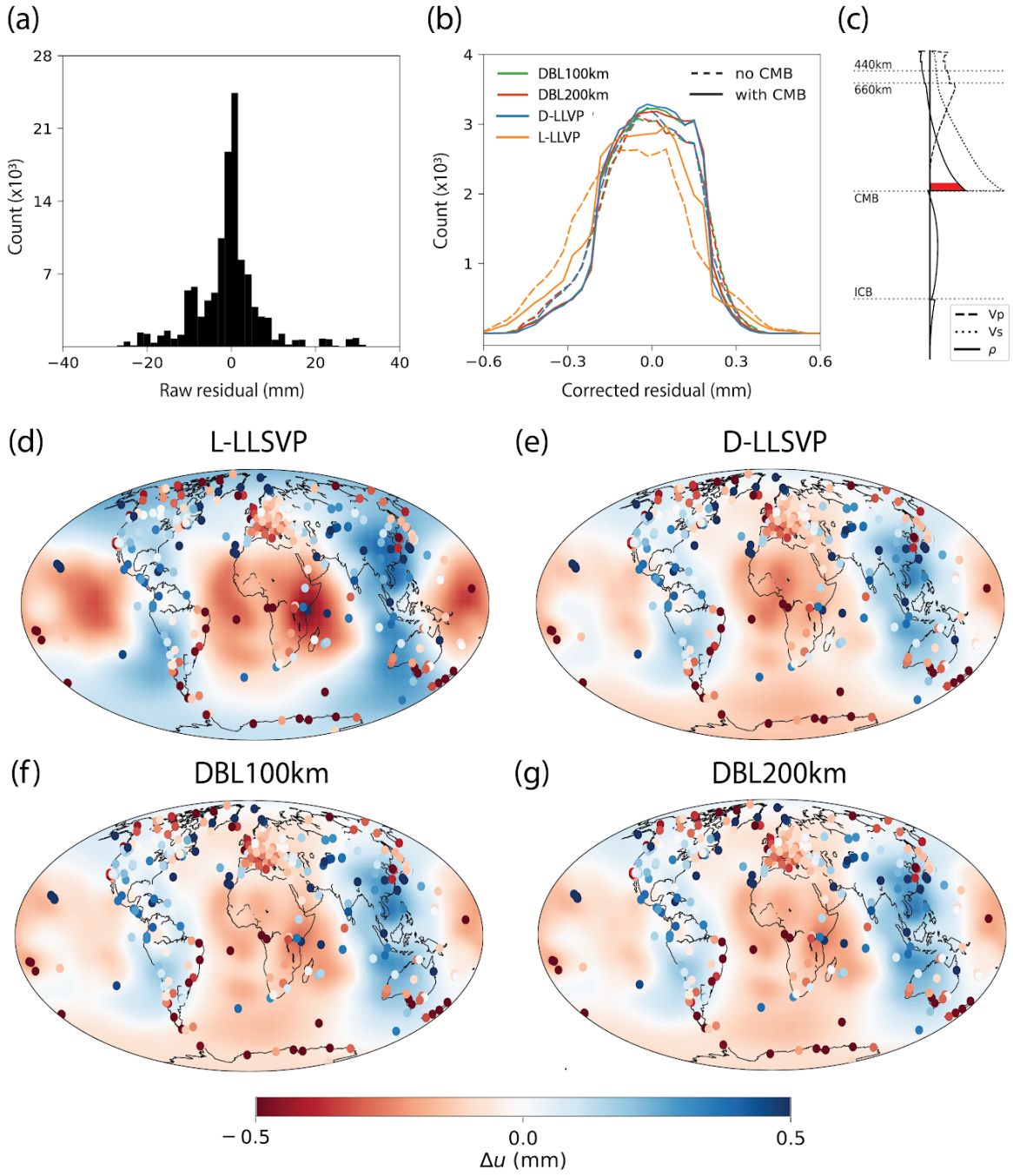

Figure 4.3 | Body tide residuals: distributions and maps. (**a**) Raw residuals: resampled GPS measurements of vertical displacement amplitude (with predictions from background 1D elastic and anelastic model removed). (**b**) Corrected residuals (Δu) Raw residuals minus predictions made by adopting each of our test models and predictions of ocean tidal loading. (**c**) Associated sensitivity kernels for density (solid), shear wave-speed (dotted) and compressional wave-speed (dashed). The density sensitivity of the bottom 100 km of the mantle is filled red for emphasis. (**d-f**) Maps: 3D-background model predictions of vertical displacement amplitude associated with each model. The colored circles indicate the GPS determined Δu. Note that the stations closest to coastal areas carry more uncertainty (see L2017 for full details).

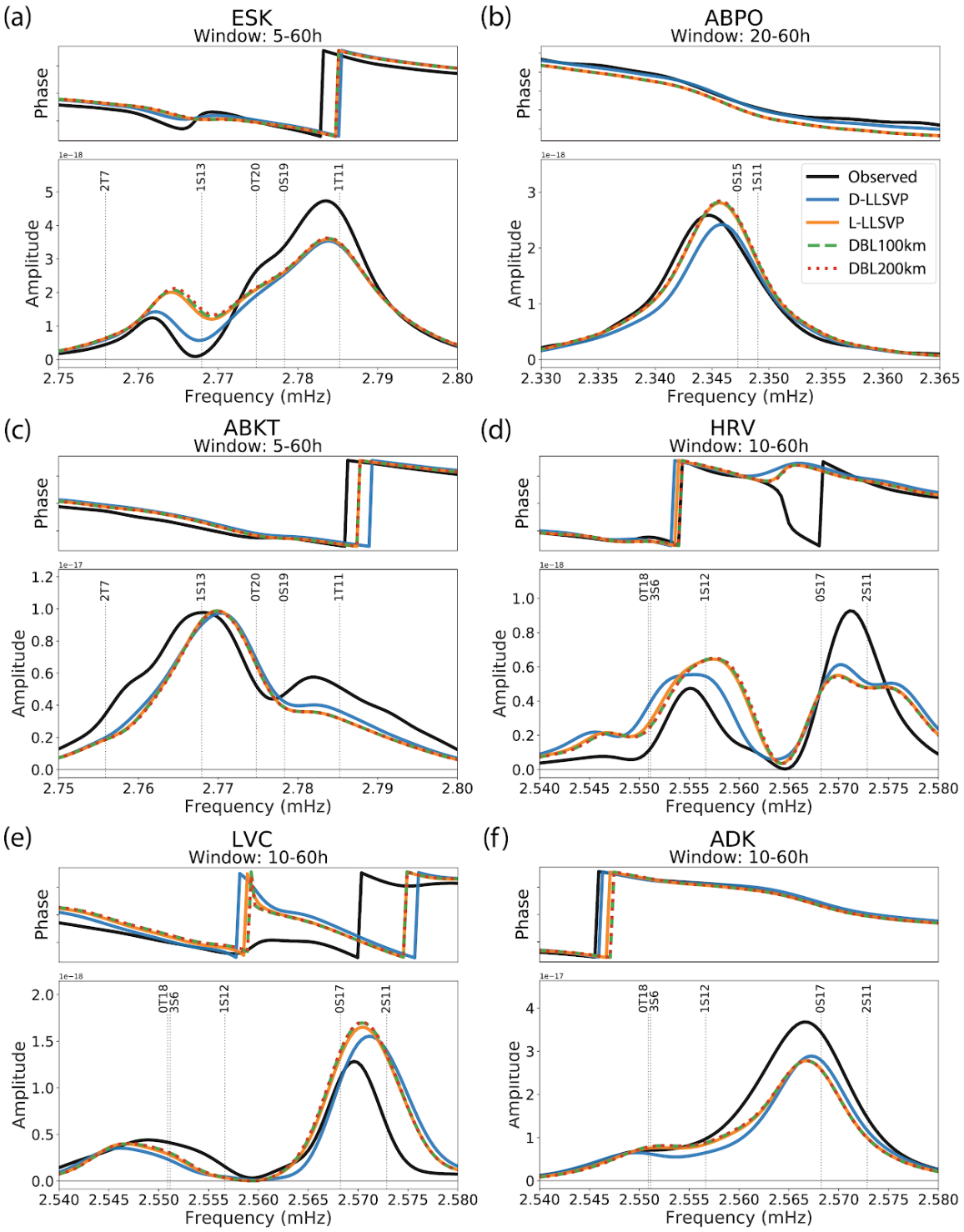

Figure 4.4 | Examples of observed and predicted spectra. (**a-f**) Full-coupled synthetics for each model (colored) compared to observed Stoneley mode spectra (black), providing a broad impression of the typical magnitude of differences between the four models and the fit to the observations. Spectral amplitudes are shown at the bottom with the phase at the top of each panel. Normal mode frequencies (as predicted in PREM (Dziewonski and Anderson, 1981)) within each frequency window are also marked (dotted vertical lines).

Discussion

The datasets considered in this study have different sensitivity to the density structure of the deep mantle, thus providing complementary information on the LLSVPs. For both body tide and splitting function observations, our results are consistent with the original studies of K2017 and L2017 - i.e., body tides do not favor a purely thermal LLSVP model, while splitting functions prefer it, particularly when underlain by positive CMB topography. We also show that density models with a dense basal layer are compatible with all datasets considered, with DBL model predictions fitting similarly well to each dataset's best-fitting model. This suggests that the excess density required to fit the tides may be located in the blind spot of the Stoneley mode sensitivity (i.e., the bottom 100-200 km of the mantle). This reduced sensitivity of the Stoneley modes to the density structure at the very base of the mantle is confirmed by their spectra. Indeed, noting that both DBL models and L-LLSVP are identical above the bottom 200 km of the mantle, spectra of these models are often barely distinguishable (Figure 4.4).

The Stoneley mode spectra considered here are also largely insensitive to the CMB topographies considered, though spectra may differ for other events. Similarly, body tide observations suggest that CMB topography alone is unable to match observations in a purely thermal LLSVP. An upward deflection of ~1.5 km below the LLSVPs improves the significance by only 0.5% in a thermal LLSVP model, still ~5% below the acceptable cutoff, while topography significantly larger than 3 km at long-wavelengths is not well-supported by observations (Koelemeijer, 2020). Meanwhile, to attain model probabilities close to those of K2017 (P-weighted ≈ 0.48) the splitting function dataset requires large CMB topographies, particularly for the three dense models (Figure 4.2), with maximum/minimum amplitudes of +13/-6, +11/-3, and +8/-2 km for D-LLSVP, DBL200km, and DBL100km, respectively. While the magnitude of these topographies is large relative to observations at these wavelengths (Koelemeijer, 2020), they likely result from the reduced number of free parameters explored in our study. While in K2017, CMB topography may trade-off with two density scaling factors, which were allowed to vary freely in the lower mantle, any residual misfit for our limited number of conceptual density models must be addressed via the CMB topography alone.

Though our conceptual DBL models reconcile all three datasets, the exact density structure and magnitudes are not well-constrained. For example, tides are primarily sensitive to degree two structure, while the Stoneley modes offer constraints on higher degrees. As such, the net density increases necessary to fit body tide observations would likely be reduced by placing lighter material at higher degrees, to which tides are effectively insensitive. Furthermore, since we did not directly explore the magnitude of density scaling in the basal layer, we offer only weak constraints on the magnitude of the density anomaly. We also acknowledge other limitations of our approach. Stronger constraints on the magnitude and extent of LLSVP density anomalies would likely be obtained by including measurements of the gravest normal mode 0S2, which has significant sensitivity to lowermost mantle density (Moulik and Ekström, 2016). Additionally, a more realistic V_p-V_s scaling could be utilized in the future, recognizing that $d\ln V_s/d\ln V_p$ increases to values in excess of 2.5 in the lowermost 500-1000 km of the mantle, which is incompatibly with a purely thermal origin of heterogeneity (Robertson and Woodhouse, 1995b; Romanowicz, 2001; W. Su and Dziewonski, 1997). However, since the scope of this study was to test conceptual models and assess their ability to reconcile the seemingly differing results of Lau et al., (2017), and Koelemeijer et al., (2017), using the original methodologies and datasets, these considerations were not implemented in our study so far.

As in L2017, we might rule out model L-LLSVP due to a poor fit with body tide observations, even when considering the density effect of a significant upward deflection of the CMB. Meanwhile, as in K2017, we might discount D-LLSVP due to the large positive CMB topography required to fit splitting function observations, a scenario which seems dynamically infeasible given the overlying, ~600km tall, dense LLSVP. While the DBL models also require large positive CMB topographies to fit splitting functions, this is arguably less problematic given the narrowness of the dense layers and the buoyant thermal material present immediately above. However, further dynamical simulations are required to test this scenario.

While the new Stoneley mode spectra are fit similarly by all models (Figure 4.1), the differences between models are of similar magnitude to the difference between model predictions and the observations (Figure 4.4). This implies that there are other, arguably more important issues with the models considered here than the differing models of LLSVP density. In particular, the adopted isotropic and anisotropic V_s and V_p mantle structure needs improvement (Appendix Figure - C9b). Uncertainties in source parameters also contribute to misfits between synthetics and observed spectra (Appendix Figure - C9c). This latter issue is naturally reduced via the construction of splitting functions due to the combination of solutions from numerous events. However, such an approach assumes truncated coupling theory of isolated-mode or pair-of-modes coupling, which is known to result in its own non-negligible inaccuracies in many cases (Deuss and Woodhouse, 2001; Al-Attar et al., 2012; Yang and Tromp, 2015). The inversion required to produce splitting functions is also inherently non-unique (Akbarashrafi et al., 2018). As a result, we propose — in addition to the continued efforts to construct higher resolution and more accurate mantle models and improved source solutions — that working directly with a significantly increased dataset of spectra may help enhance the density signal of the LLSVPs while minimizing theoretical uncertainty.

Our finding that Stoneley modes and body tide observations can indeed be reconciled by considering thermal LLSVPs with very dense, thin layers at their base is in good agreement with recent multi-observable studies. For example, Richards (2019) found that to simultaneously match Earth's long-wavelength geoid, CMB excess ellipticity, and new observations of long-wavelength dynamic topography, a thin, ~200 km-thick layer of dense material is likely needed at the base of LLSVPs. Meanwhile, Jones et al. (2019) proposed that a compositionally distinct, dense reservoir in the lowermost mantle was required to match the observed Tungsten-isotopic differences between LIPs and ocean island basalts. We do note, however, that the excess density in our DBL models exceeds those tested by Jones et al. (2019). However, their magnitudes may be consistent with the long-wavelength expression of a collection of Ultra-Low Velocity Zones (ULVZs), regions characterized by extreme reductions in shear wave-speed, which are preferentially found within LLSVPs or at their edges (e.g. McNamara et al., 2010; Yu and Garnero, 2018). ULVZs may require excess densities of ~10% (Rost et al., 2005) with mineral physics studies on candidate compositions suggesting similar magnitudes (e.g. Dobrosavljevic et al., 2019). The dense layer proposed may therefore not be continuous throughout the LLSVP's base. Moving forward, constraining the spatial variations, height and strength of such a dense LLSVP base likely requires refined constraints on other sources of uncertainty, such as the 3D wave-speed structure of the mantle.

Conclusions

Following the seemingly contradicting conclusions from two recent studies on deep mantle density structure, a body tide study (Lau et al., 2017), and Stoneley mode study (Koelemeijer et al., 2017), where the former preferred excess densities within the LLSVP regions and the latter preferred the opposite (paired with an associated elevated CMB), we have revisited this issue. By combining both these datasets and augmenting them further with the spectra of several Stoneley modes, we took advantage of the distinct depth sensitivities of each data type. We hypothesized that the excess density required by body tide data may be stored in the "blind spot" of Stoneley mode sensitivity, just above the CMB. We showed that if the excess density is confined to a thin basal layer within the LLSVPs, tidal data is fit just as well as when the density excess is distributed over a greater depth range. Meanwhile, such a model also fits both P2017's splitting functions, noting that the addition of elevated CMB topography helps improve the fit to the splitting function data, while new Stoneley mode spectra measurements are similarly well fit with a purely thermal LLSVP model.

We showed that if the excess density is confined to a thin basal layer within the LLSVPs we can fit the body tide data well, while for both Stoneley mode splitting functions and spectra including such a layer results in fits that are no worse than those obtained from models that don't include such a layer. We note that Stoneley mode observations are not particularly well fit by any models however, likely due to uncertainty in other factors, such as overlying mantle structure, source parameters etc. (see preceding chapter), which need to be better constrained before better-fitting spectra might be computed. While 0S2 is not classified as a Stoneley mode, it may well provide the additional information needed to definitively provide a resolution to the question addressed in this chapter, as advocated by Moulik and Ekström (2016). Adding mode 0S2 to our mode data collection is the subject of on-going work.

Along with an increasing number of geodynamical studies favoring a model in which thermochemical heterogeneity is stored at the very base of the mantle (e.g., Simmons et al., 2010; Richards et al., 2019; Jones et al., 2019, Lu et al., 2020) and the identification of other seismological features that require strong wave-speed and density contrasts (e.g., ULVZs, Garnero et al., 1993), a consistent picture of deep, spatially confined, compositional heterogeneity in the deep mantle is slowly emerging.

Chapter 5

Conclusions

This thesis represents a collected effort to better understand the density distribution within the Earth, a fundamental yet difficult property to constrain, partly due to inherent non-uniqueness presented by the physics of gravity. The approach is twofold: (i) we focus on the radial, or 1D, density profile across the most uncertain region of the Earth – the inner core (Chapter 2); and (ii), we turn to lateral, or 3D, density structure in the deepest part of the mantle – a subject of ongoing debate yet vital to understanding mantle convection (Chapters 3 and 4). In order to do all of this, we turn to a specific type of seismic data: normal modes, the standing wave limit of Earth's response to an earthquake. Normal modes, due to their low frequencies, have significant sensitivity to density within the Earth and we exploit this here to address some key issues.

1D Density Structure: Normal mode constraints on the inner core

Normal modes are characterized by distinct sensitivities to different regions within the earth and can thus be categorized by their sensitivity. By assembling a catalog of well-characterized inner core (IC)-sensitive normal mode center-frequencies based on the most up-to-date measurements, and simultaneously exploring variations in average V_s, V_p and ρ within the IC, we have shown that IC velocities are well-constrained by these data. These constraints are robust even with the choice of dataset, the mantle model, data uncertainty and IC radius.

While V_p is in good agreement with PREM, a minor (~1%) reduction in V_s with respect to PREM is favored. We additionally demonstrate that lowering V_s by as much as 2.5% (while keeping density fixed to PREM), as proposed by Tkalcic et al. (2018), is incompatible with normal mode center-frequency observations. Within our dataset, the sensitivity to density is significantly lower than the sensitivity to seismic velocity. Nevertheless, we find that our dataset favors a reduction in average density across the IC by 0.7—1.7% relative to PREM.

While normal mode data alone struggle to determine the detailed depth dependence of elastic and density parameters within the IC, by fine-tuning these best-fitting averages and their associated standard deviations, we have provided useful constraints for laboratory and *ab-initio* studies that aim to constraining IC composition. A lower density IC may require a reduction in the magnitude of the IC boundary density jump, associated with light element partitioning (by over half that compared to PREM), which may have further implications on the available power to drive the geodynamo, still an active area of research.

3D Density Structure: An evaluation of Stoneley mode methodology and sensitivity

Moving on to lateral structure, we focus on a special subset of normal modes, namely the core-mantle boundary (CMB) Stoneley modes, which are vibrations trapped along the CMB, only observable at the surface of the Earth through coupling with mantle modes by 3D structure. This newly discovered dataset presents much promise to determine deep mantle 3D structure (Koelemeijer et al., 2013), but first, an understanding of the relative importance of (i) approximations applied in simulating their spectra and (ii) various mantle structures and their uncertainties, is required to utilize them in the most advantageous manner.

First, we explore several typically adopted approximations used to determine their spectra (and associated splitting functions). We find that various levels of truncation (wide-band, group coupling, and pair-of-mode coupling) produce significant errors relative to the full-coupling calculations up to 3.1 mHz. In particular, the most inaccurate pair-of-mode coupling, has been used to generate Stoneley mode splitting functions (Koelemeijer et al., 2013), a derived data type that processes many spectra.

Second, we compare the effects of uncertainty in any *a-priori* assumptions, including the imposed mantle velocity structure, the source solution, CMB topography, and the radial attenuation model, and find that the uncertainty due to the first two of these significantly affects Stoneley mode spectra.

Our combined calculations show that significant error is introduced by truncated theory, especially the pair-of-mode coupling theory commonly applied in the generation of splitting functions. To better constrain the spatial distribution of density, and thus thermal and chemical heterogeneity, requires that we reduce uncertainty in mantle models, and suggests that tomographic models must attempt to independently constrain V_p, V_s, and density. Given Stoneley mode sensitivity to regions just above and just below the CMB, not only does density structure need to be constrained simultaneously in both regions (to avoid issues surrounding non-uniqueness), but if accomplished, important questions may be addressed surrounding the chemically distinct layer proposed at the top of the outer core (the so-called E' layer), and deep mantle density variations may be more accurately determined, the issue at the heart of Chapter 4.

3D Density Structure: Constraining LLSVP density

Lateral density structure in the deepest part of the mantle has recently gained renewed attention following two studies: a body tide study (Lau et al., 2017), and Stoneley mode study (Koelemeijer et al., 2017), where the former preferred excess densities within the Large Low Shear Velocity Province ("LLSVP") regions and the latter preferred the opposite (paired with an associated elevated CMB). Both studies applied completely new datasets for the first time, while the former used GPS measurements of body tides and found density within the LLSVP regions to be negatively buoyant, the latter used Stoneley mode splitting functions and concluded the opposite. We have revisited this issue by combining both these datasets and augmenting them further with the spectra of several Stoneley modes using the methodology developed in Chapter 3. Our motivation was to test several conceptual models of LLSVP density motivated by the distinct depth sensitivities of both data types. We hypothesized that the excess density required by body tide data may be stored in the "blind spot" of Stoneley mode sensitivity, extending ~100 km above the CMB. We confirmed that if the excess density found to be required to fit body tide data were

confined to a thin basal layer within the LLSVPs, tidal observations are well fit, while Stoneley mode observations are fit no worse than by a model lacking such a dense basal layer. Additionally, we show that fits to observed spectra from all models are inadequate to make strong inferences about LLSVP density structure and that improved constraints on other factors, such as the overlying mantle structure are necessary to distinguish between LLSVP density models in future.

While we do not necessarily suggest that these models represent the true density distribution of the Earth, the notion of a dense basal layer has received support from a growing number of independent studies. Geodynamical studies favor models in which thermochemical heterogeneity is stored at the very base of the mantle (e.g., Simmons et al., 2010; Richards et al., 2019; Jones et al., 2019, Lu et al., 2020) and the identification of several seismological features require strong wave-speed and density contrasts (e.g., ULVZs, Garnero et al., 1993). The work herein, and the studies listed, present a consistent picture of deep, spatially confined, dense, compositional heterogeneity within the base of the LLSVPs.

References

Abubakirov, I.R., Pavlov, V.M., Titkov, N.N., 2015. The mechanism of the deep-focus, Sea of Okhotsk earthquake of May 24, 2013 as inferred from static displacements and broadband seismograms. J. Volcanol. Seismol. https://doi.org/10.1134/S0742046315040028

Akbarashrafi, F., Al-Attar, D., Deuss, A., Trampert, J., Valentine, A.P., 2018. Exact free oscillation spectra, splitting functions and the resolvability of earth's density structure. Geophys. J. Int. https://doi.org/10.1093/gji/ggx539

Al-Attar, D., Woodhouse, J.H., Deuss, A., 2012. Calculation of normal mode spectra in laterally heterogeneous earth models using an iterative direct solution method. Geophys. J. Int. 189, 1038–1046. https://doi.org/10.1111/j.1365-246X.2012.05406.x

Alfè, D., Kresse, G., Gillan, M.J., 2000. Structure and dynamics of liquid iron under Earth's core conditions. Phys. Rev. B 61, 132–142. https://doi.org/10.1103/physrevb.61.132

Andrews, J., Deuss, A., Woodhouse, J., 2006. Coupled normal-mode sensitivity to inner-core shear velocity and attenuation. Geophys. J. Int. 167, 204–212. https://doi.org/10.1111/j.1365-246x.2006.03022.x

Antonangeli, D., Siebert, J., Badro, J., Farber, D.L., Fiquet, G., Morard, G., Ryerson, F.J., 2010. Composition of the Earth's inner core from high-pressure sound velocity measurements in Fe--Ni--Si alloys. Earth Planet. Sci. Lett. 295, 292–296. https://doi.org/10.1016/j.epsl.2010.04.018

Bazhanova, Z.G., Oganov, A.R., Gianola, O., 2012. Fe--C and Fe--H systems at pressures of the Earth's inner core. Physics-Uspekhi 55, 489–497. https://doi.org/10.3367/ufne.0182.201205c.0521

Beghein, C., 2003. Robust Normal Mode Constraints on Inner-Core Anisotropy from Model Space Search. Science (80-.). 299, 552–555. https://doi.org/10.1126/science.1078159

Belonoshko, A.B., Skorodumova, N. V, Davis, S., Osiptsov, A.N., Rosengren, A., Johansson, B., 2007. Origin of the Low Rigidity of the Earth's Inner Core. Science (80-.). 316, 1603–1605. https://doi.org/10.1126/science.1141374

Birch, F., 1964. Density and composition of mantle and core. J. Geophys. Res. 69, 4377–4388. https://doi.org/10.1029/jz069i020p04377

Birch, F., 1961. The velocity of compressional waves in rocks to 10 kilobars, part 2. J. Geophys. Res. 66, 2199–2224. https://doi.org/10.1029/sp026p0091

Birch, F., 1952. Elasticity and constitution of the Earth's interior. J. Geophys. Res. 57, 227–286. https://doi.org/10.1029/jz057i002p00227

Brodholt, J., Badro, J., 2017. Composition of the low seismic velocity E 0 layer at the top of Earth's core. Geophys. Res. Lett. 44, 8303–8310. https://doi.org/10.1002/2017GL074261

Buffett, B., 2014. Geomagnetic fluctuations reveal stable stratification at the top of the Earth's core. Nature 507, 484–487. https://doi.org/10.1038/nature13122

Buffett, B.A., Seagle, C.T., 2010. Erratum: Stratification of the top of the core due to chemical

interactions with the mantle (Journal of Geophysical Research (2011) 116 (B07405) DOI:10.1029/2011JB008376). J. Geophys. Res. Solid Earth. https://doi.org/10.1029/2009JB006751

Cammarano, F., Romanowicz, B., 2008. Radial profiles of seismic attenuation in the upper mantle based on physical models. Geophys. J. Int. 175, 116–134. https://doi.org/10.1111/j.1365-246X.2008.03863.x

Cao, A., 2005. An Observation of PKJKP: Inferences on Inner Core Shear Properties. Science (80-.). 308, 1453–1455. https://doi.org/10.1126/science.1109134

Cao, A., Romanowicz, B., 2004. Constraints on density and shear velocity contrasts at the inner core boundary. Geophys. J. Int. 157, 1146–1151. https://doi.org/10.1111/j.1365-246x.2004.02330.x

Caracas, R., 2015. The influence of hydrogen on the seismic properties of solid iron. Geophys. Res. Lett. 42, 3780–3785. https://doi.org/10.1002/2015gl063478

Chambat, F., Valette, B., 2001. Mean radius, mass, and inertia for reference Earth models. Phys. Earth Planet. Inter. https://doi.org/10.1016/S0031-9201(01)00200-X

Dahlen, F.A., 1968. The Normal Modes of a Rotating, Elliptical Earth. Geophys. J. R. Astron. Soc. https://doi.org/10.1111/j.1365-246X.1968.tb00229.x

Davaille, A., 1999. Simultaneous generation of hotspots and superwells by convetion in a heterogeneous planetary mantle. Nature 402, 756–760. https://doi.org/10.1038/45461

Davies, D.R., Goes, S., Davies, J.H., Schuberth, B.S.A., Bunge, H.P., Ritsema, J., 2012. Reconciling dynamic and seismic models of Earth's lower mantle: The dominant role of thermal heterogeneity. Earth Planet. Sci. Lett. 353–354, 253–269. https://doi.org/10.1016/j.epsl.2012.08.016

de Wit, R.W.L., Käufl, P.J., Valentine, A.P., Trampert, J., 2014. Bayesian inversion of free oscillations for Earth's radial (an)elastic structure. Phys. Earth Planet. Inter. 237, 1–17. https://doi.org/10.1016/j.pepi.2014.09.004

Deuss, A., 2008. Normal mode constraints on shear and compressional wave velocity of the Earth's inner core. Earth Planet. Sci. Lett. 268, 364–375. https://doi.org/10.1016/j.epsl.2008.01.029

Deuss, A., Ritsema, J., van Heijst, H., 2013. A new catalogue of normal-mode splitting function measurements up to 10 mHz. Geophys. J. Int. 193, 920–937. https://doi.org/10.1093/gji/ggt010

Deuss, A., Woodhouse, J.H., 2001. Theoretical free-oscillation spectra: the importance of wide band coupling. Geophys. J. Int.

Deuss, A., Woodhouse, J.H., Paulssen, H., Trampert, J., 2000. The observation of inner core shear waves. Geophys. J. Int. 142, 67–73. https://doi.org/10.1046/j.1365-246x.2000.00147.x

Dobrosavljevic, V. V., Sturhahn, W., Jackson, J.M., 2019. Evaluating the Role of Iron-Rich (Mg,Fe)O in Ultralow Velocity Zones. Minerals 9, 762. https://doi.org/10.3390/min9120762

Durek, J.J., Ekström, G., 1996. A radial model of anelasticity consistent with long-period surface-wave attenuation. Bull. Seismol. Soc. Am. 86, 144–158.

Durek, J.J., Romanowicz, B., 1999. Inner core anisotropy inferred by direct inversion of normal mode spectra. Geophys. J. Int. 139, 599–622. https://doi.org/10.1046/j.1365-246x.1999.00961.x

Dziewonski, A.M., 1984. Mapping the lower mantle: Determination of lateral heterogeneity in *P* velocity up to degree and order 6. J. Geophys. Res. Solid Earth 89, 5929–5952. https://doi.org/10.1029/JB089iB07p05929

Dziewonski, A.M., Anderson, D.L., 1981. Preliminary reference Earth model. Phys. Earth Planet. Inter. 25, 297–356. https://doi.org/10.1016/0031-9201(81)90046-7

Dziewonski Adam M., Gilbert, F., 1971. Solidity of the Inner Core of the Earth inferred from Normal Mode Observations. Nature 234, 465–466. https://doi.org/10.1038/234465a0

Edmonds, A.R., 1960. Angular Momentum in Quantum Mechanics. Princeton University Press. https://doi.org/10.2307/3610250

Ekström, G., Nettles, M., Dziewoński, A.M., 2012. The global CMT project 2004-2010: Centroid-moment tensors for 13,017 earthquakes. Phys. Earth Planet. Inter. 200–201, 1–9. https://doi.org/10.1016/j.pepi.2012.04.002

Forte, A.M., Mitrovica, J.X., 2001. Deep-mantle high-viscosity flow and thermochemical structure inferred from seismic and geodynamic data. Nature 410, 1049–1056. https://doi.org/10.1038/35074000

Fowler, C.M.R., 2005. The solid earth: an introduction to global geophysics. solid earth an Introd. to Glob. Geophys. https://doi.org/10.1029/90eo00309

Frost, D.A., Rost, S., 2014. The P-wave boundary of the Large-Low Shear Velocity Province beneath the Pacific. Earth Planet. Sci. Lett. 403, 380–392. https://doi.org/10.1016/j.epsl.2014.06.046

Garnero, E., McNamara, A.K., Shim, S.H.D., 2014. Llsvp. AGUFM 2014, DI33B-01.

Garnero, E.J., Grand, S.P., Helmberger, D. V., 1993a. Low P-wave velocity at the base of the mantle. Geophys. Res. Lett. 20, 1843–1846. https://doi.org/10.1029/93GL02009

Garnero, E.J., Helmberger, D. V., 1998. Further structural constraints and uncertainties of a thin laterally varying ultralow-velocity layer at the base of the mantle. J. Geophys. Res. Solid Earth 103, 12495–12509. https://doi.org/10.1029/98jb00700

Garnero, E.J., Helmberger, D. V., Grand, S.P., 1993b. Constraining outermost core velocity with *SmKS* waves. Geophys. Res. Lett. 20, 2463–2466. https://doi.org/10.1029/93GL02823

Gubbins, D., Masters, T.G., Jacobs, J.A., 1979. Thermal evolution of the Earth's core. Geophys. J. Int. 59, 57–99. https://doi.org/10.1111/j.1365-246x.1979.tb02553.x

Hager, B.H., O'Connell, R.J., 1981. A simple global model of plate dynamics and mantle convection. J. Geophys. Res. Solid Earth 86, 4843–4867. https://doi.org/10.1029/JB086iB06p04843

He, X., Tromp, J., 1996. Normal-mode constraints on the structure of the Earth. J. Geophys. Res. Solid Earth 101, 20053–20082. https://doi.org/10.1029/96jb01783

He, Y., Wen, L., 2012. Geographic boundary of the "Pacific Anomaly" and its geometry and

transitional structure in the north. J. Geophys. Res. Solid Earth 117. https://doi.org/10.1029/2012JB009436

Helffrich, G., Kaneshima, S., 2013. Causes and consequences of outer core stratification. Phys. Earth Planet. Inter. 223, 2–7. https://doi.org/10.1016/j.pepi.2013.07.005

Helffrich, G., Kaneshima, S., 2010. Outer-core compositional stratification from observed core wave speed profiles. Nature 468, 807–812. https://doi.org/10.1038/nature09636

Helmberger, D. V., Ni, S., 2005. Seismic modeling constraints on the South African super plume, in: Geophysical Monograph Series. Blackwell Publishing Ltd, pp. 63–81. https://doi.org/10.1029/160GM06

Hirose, K., Morard, G., Sinmyo, R., Umemoto, K., Hernlund, J., Helffrich, G., Labrosse, S., 2017. Crystallization of silicon dioxide and compositional evolution of the Earth's core. Nature 543, 99–102. https://doi.org/10.1038/nature21367

Houser, C., Masters, G., Shearer, P., Laske, G., 2008. Shear and compressional velocity models of the mantle from cluster analysis of long-period waveforms. Geophys. J. Int. 174, 195–212. https://doi.org/10.1111/j.1365-246X.2008.03763.x

Irving, J.C.E., Cottaar, S., Lekić, V., 2018. Seismically determined elastic parameters for Earth's outer core. Sci. Adv. 4, eaar2538. https://doi.org/10.1126/sciadv.aar2538

Irving, J.C.E., Deuss, A., 2011. Stratified anisotropic structure at the top of Earth's inner core : A normal mode study. Phys. Earth Planet. Inter. 186, 59–69. https://doi.org/10.1016/j.pepi.2011.03.003

Ishii, M., Tromp, J., 1999. Normal-mode and free-air gravity constraints on lateral variations in velocity and density of earth's mantle. Science (80-.). 285, 1231–1236. https://doi.org/10.1126/science.285.5431.1231

Jackson, M.G., Becker, T.W., Konter, J.G., 2018. Geochemistry and Distribution of Recycled Domains in the Mantle Inferred From Nd and Pb Isotopes in Oceanic Hot Spots: Implications for Storage in the Large Low Shear Wave Velocity Provinces. Geochemistry, Geophys. Geosystems 19, 3496–3519. https://doi.org/10.1029/2018GC007552

Jackson, M.G., Konter, J.G., Becker, T.W., 2017. Primordial helium entrained by the hottest mantle plumes. Nature 542, 340–343. https://doi.org/10.1038/nature21023

Jellinek, A.M., Manga, M., 2002. The influence of a chemical boundary layer on the fixity, spacing and lifetime of mantle plumes. Nature 418, 760–763. https://doi.org/10.1038/nature00979

Jephcoat, A., Olson, P., 1987. Is the inner core of the Earth pure iron? Nature 325, 332–335. https://doi.org/10.1038/325332a0

Jones, T.D., Davies, D.R., Sossi, P.A., 2019. Tungsten isotopes in mantle plumes: Heads it's positive, tails it's negative. Earth Planet. Sci. Lett. 506, 255–267. https://doi.org/10.1016/j.epsl.2018.11.008

Julian B R; Davies, D.S.R.M., 1972. PKJKP. Nature 235, 317–318. https://doi.org/10.1038/235317a0

Kaneshima, S., 2018. Array analyses of SmKS waves and the stratification of Earth's outermost core. Phys. Earth Planet. Inter. 276, 234–246. https://doi.org/10.1016/j.pepi.2017.03.006

Kaneshima, S., Matsuzawa, T., 2015. Stratification of earth's outermost core inferred from SmKS array data. Prog. Earth Planet. Sci. 2, 1–15. https://doi.org/10.1186/s40645-015-0046-5

Karato, S., 1993. Importance of anelasticity in the interpretation of seismic tomography. Geophys. Res. Lett. 20, 1623–1626. https://doi.org/10.1029/93GL01767@10.1002/(ISSN)1944-8007.GRL40

Kennett, B.L.N., Widiyantoro, S., van der Hilst, R.D., 1998. Joint seismic tomography for bulk sound and shear wave speed in the Earth's mantle. J. Geophys. Res. Solid Earth 103, 12469–12493. https://doi.org/10.1029/98jb00150

Koelemeijer, P., 2020. Towards consistent seismological models of the core-mantle boundary landscape. https://doi.org/10.1002/ESSOAR.10502426.1

Koelemeijer, P., Deuss, A., Ritsema, J., 2017. Density structure of Earth's lowermost mantle from Stoneley mode splitting observations. Nat. Commun. 8, 1–10. https://doi.org/10.1038/ncomms15241

Koelemeijer, P., Deuss, A., Ritsema, J., 2013. Observations of core-mantle boundary Stoneley modes. Geophys. Res. Lett. 40, 2557–2561. https://doi.org/10.1002/grl.50514

Koelemeijer, P., Ritsema, J., Deuss, A., van Heijst, H.-J., 2016. SP12RTS: a degree-12 model of shear- and compressional-wave velocity for Earth's mantle. Geophys. J. Int. 204, 1024–1039.

Kohler, M.D., Tanimoto, T., 1992. One-layer global inversion for outermost core velocity. Phys. Earth Planet. Inter. 72, 173–184. https://doi.org/10.1016/0031-9201(92)90200-F

Koper, K.D., Dombrovskaya, M., 2005. Seismic properties of the inner core boundary from PKiKP/P amplitude ratios. Earth Planet. Sci. Lett. 237, 680–694. https://doi.org/10.1016/j.epsl.2005.07.013

Kuo, C., Romanowicz, B., 2002. On the resolution of density anomalies in the earth's mantle using spectral fitting of normal-mode data. Geophys. J. Int. 150, 162–179. https://doi.org/10.1046/j.1365-246X.2002.01698.x

Kustowski, B., Ekström, G., Dziewoński, A.M., 2008. Anisotropic shear-wave velocity structure of the earth's mantle: A global model. J. Geophys. Res. Solid Earth 113, 1–23. https://doi.org/10.1029/2007JB005169

Laske, G., Masters, G., 1999. Limits on differential rotation of the inner core from an analysis of the Earth's free oscillations. Nature 402, 66–69. https://doi.org/10.1038/47011

Lau, H., Mitrovica, J.X., Davis, J.L., Tromp, J., Yang, H.Y., Al-Attar, D., 2017. Tidal tomography constrains Earth's deep-mantle buoyancy. Nature 551, 321–326. https://doi.org/10.1038/nature24452

Lay, T., Young, C.J., 1990. The stably-stratified outermost core revisited. Geophys. Res. Lett. 17, 2001–2004. https://doi.org/10.1029/GL017i011p02001

Lehmann, I., 1936. P'. Bur. Centr. Seism. Internat. Ser. A 14.

Lekic, V., Cottaar, S., Dziewonski, A., Romanowicz, B., 2012. Cluster analysis of global lower mantle tomography: A new class of structure and implications for chemical heterogeneity. Earth Planet. Sci. Lett. 357–358, 68–77. https://doi.org/10.1016/J.EPSL.2012.09.014

Lesur, V., Whaler, K., Wardinski, I., 2015. Are geomagnetic data consistent with stably stratified flow at the core–mantle boundary? Geophys. J. Int. 201, 929–946. https://doi.org/10.1093/gji/ggv031

Li, Y., Vočadlo, L., Brodholt, J.P., 2018. The elastic properties of hcp-Fe alloys under the conditions of the Earth's inner core. Earth Planet. Sci. Lett. 493, 118–127. https://doi.org/10.1016/j.epsl.2018.04.013

Loper, D.E., 1978. Some thermal consequences of a gravitationally powered dynamo. J. Geophys. Res. Solid Earth 83, 5961–5970. https://doi.org/10.1029/jb083ib12p05961

Mäkinen, A.M., Deuss, A., Redfern, S.A.T., 2014. Anisotropy of Earth's inner core intrinsic attenuation from seismic normal mode models. Earth Planet. Sci. Lett. 404, 354–364. https://doi.org/10.1016/j.epsl.2014.08.009

Martorell, B., Vocadlo, L., Brodholt, J., Wood, I.G., 2013. Strong Premelting Effect in the Elastic Properties of hcp-Fe Under Inner-Core Conditions. Science (80-.). 342, 466–468. https://doi.org/10.1126/science.1243651

Masters, G., Gubbins, D., 2003. On the resolution of density within the Earth. Phys. Earth Planet. Inter. 140, 159–167. https://doi.org/10.1016/j.pepi.2003.07.008

Masters, G., Laske, G., Bolton, H., Dziewonski, A., 2000. The relative behavior of shear velocity, bulk sound speed, and compressional velocity in the mantle: Implications for chemical and thermal structure, in: Geophysical Monograph Series. Blackwell Publishing Ltd, pp. 63–87. https://doi.org/10.1029/GM117p0063

McNamara, A.K., 2019. A review of large low shear velocity provinces and ultra low velocity zones. Tectonophysics 760, 199–220. https://doi.org/10.1016/j.tecto.2018.04.015

McNamara, A.K., Garnero, E.J., Rost, S., 2010. Tracking deep mantle reservoirs with ultra-low velocity zones. Earth Planet. Sci. Lett. 299, 1–9. https://doi.org/10.1016/j.epsl.2010.07.042

Megnin, C., Romanowicz, B., 2000. The three-dimensional shear velocity structure of the mantle from the inversion of body, surface and higher-mode waveforms. Geophys. J. Int. 143, 709–728. https://doi.org/10.1046/j.1365-246X.2000.00298.x

Mosca, I., Cobden, L., Deuss, A., Ritsema, J., Trampert, J., 2012. Seismic and mineralogical structures of the lower mantle from probabilistic tomography. J. Geophys. Res. Solid Earth 117. https://doi.org/10.1029/2011JB008851

Moulik, P., Ekström, G., 2016. The relationships between large-scale variations in shear velocity, density, and compressional velocity in the Earth's mantle. J. Geophys. Res. Solid Earth 121, 2737–2771. https://doi.org/10.1002/2015jb012679

Moulik, P., Ekström, G., 2014. An anisotropic shear velocity model of the Earth's mantle using normal modes, body waves, surface waves and long-period waveforms. Geophys. J. Int. 199, 1713–1738. https://doi.org/10.1093/gji/ggu356

Mulyukova, E., Steinberger, B., Dabrowski, M., Sobolev, S. V., 2015. Survival of LLSVPs for billions of years in a vigorously convecting mantle: Replenishment and destruction of chemical anomaly. J. Geophys. Res. Solid Earth 120, 3824–3847. https://doi.org/10.1002/2014JB011688

Mundl, A., Touboul, M., Jackson, M.G., Day, J.M.D., Kurz, M.D., Lekic, V., Helz, R.T., Walker, R.J., 2017. Tungsten-182 heterogeneity in modern ocean island basalts. Science (80-.). 356, 66–69. https://doi.org/10.1126/science.aal4179

Ni, S., Helmberger, D. V., 2003. Seismological constraints on the South African superplume: Could be the oldest distinct structure on earth. Earth Planet. Sci. Lett. 206, 119–131. https://doi.org/10.1016/S0012-821X(02)01072-5

Ni, S., Tan, E., Gurnis, M., Helmberger, D., 2002. Sharp sides to the African superplume. Science (80-.). 296, 1850–1852. https://doi.org/10.1126/science.1070698

Okal, E.A., Cansi, Y., 1998. Detection of PKJKP at intermediate periods by progressive multi-channel correlation. Earth Planet. Sci. Lett. 164, 23–30. https://doi.org/10.1016/s0012-821x(98)00210-6

Okal, E.A., Jo, B.G., 1990. Q measurements for Phase X overtones. Pure Appl. Geophys. PAGEOPH 132, 331–362. https://doi.org/10.1007/BF00874369

Oldham, R.D., 1906. The Constitution of the Interior of the Earth, as Revealed by Earthquakes. Q. J. Geol. Soc. 62, 456–475. https://doi.org/10.1144/gsl.jgs.1906.062.01-04.21

Poirier, J.-P., 1994. Light elements in the Earth's outer core: A critical review. Phys. Earth Planet. Inter. 85, 319–337. https://doi.org/10.1016/0031-9201(94)90120-1

Poirier, J.P., 2000. Introduction to the physics of the Earth's interior. Introd. to Phys. Earth's Inter. https://doi.org/10.1046/j.0956-540x.2000.01314.x

Reference Earth Model, n.d.

Resovsky, J., Trampert, J., 2003. Using probabilistic seismic tomography to test mantle velocity-density relationships. Earth Planet. Sci. Lett. 215, 121–134. https://doi.org/10.1016/S0012-821X(03)00436-9

Richards, F.D., 2019. Global Analysis of Predicted and Observed Dynamic Topography. University of Cambridge. https://doi.org/https://doi.org/10.17863/CAM.31532

Ritsema, J., Deuss, A., Van Heijst, H.J., Woodhouse, J.H., 2011. S40RTS: A degree-40 shear-velocity model for the mantle from new Rayleigh wave dispersion, teleseismic traveltime and normal-mode splitting function measurements. Geophys. J. Int. 184, 1223–1236. https://doi.org/10.1111/j.1365-246X.2010.04884.x

Ritsema, J., Garnero, E., Lay, T., 1997. A strongly negative shear velocity gradient and lateral variability in the lowermost mantle beneath the Pacific. J. Geophys. Res. Solid Earth 102, 20395–20411. https://doi.org/10.1029/97jb01507

Ritsema, J., Ni, S., Helmberger, D. V., Crotwell, H.P., 1998. Evidence for strong shear velocity reductions and velocity gradients in the lower mantle beneath Africa. Geophys. Res. Lett. 25, 4245–4248. https://doi.org/10.1029/1998GL900127

Ritsema, J., Van Heijst, H.J., Woodhouse, J.H., 1999. Complex shear wave velocity structure imaged beneath Africa and Iceland. Science (80-.). 286, 1925–1931. https://doi.org/10.1126/science.286.5446.1925

Rizo, H., Walker, R.J., Carlson, R.W., Horan, M.F., Mukhopadhyay, S., Manthos, V., Francis, D., Jackson, M.G., 2016. Geochemistry: Preservation of Earth-forming events in the tungsten

isotopic composition of modern flood basalts. Science (80-.). 352, 809–812. https://doi.org/10.1126/science.aad8563

Robertson, G.S., Woodhouse, J.H., 1995a. Evidence for proportionality of P and S heterogeneity in the lower mantle. Geophys. J. Int. 123, 85–116. https://doi.org/10.1111/j.1365-246X.1995.tb06663.x

Robertson, G.S., Woodhouse, J.H., 1995b. Evidence for proportionality of P and S heterogeneity in the lower mantle. Geophys. J. Int. 123, 85–116.

Romanowicz, B., 2017. Geophysics: The buoyancy of Earth's deep mantle. Nature 551, 308–309. https://doi.org/10.1038/551308a

Romanowicz, B., 2001. Can we resolve 3D density heterogeneity in the lower mantle? Geophys. Res. Lett. 28, 1107–1110. https://doi.org/10.1029/2000GL012278

Romanowicz, B.A., Mitchell, B.J., 2015. Deep Earth Structure: Q of the Earth from Crust to Core, in: Treatise on Geophysics: Second Edition. Elsevier Inc., pp. 789–827. https://doi.org/10.1016/B978-0-444-53802-4.00021-X

Rosat, S., 2005. High-resolution analysis of the gravest seismic normal modes after the 2004 Mw = 9 Sumatra earthquake using superconducting gravimeter data. Geophys. Res. Lett. 32, L13304. https://doi.org/10.1029/2005GL023128

Rost, S., Garnero, E.J., Williams, Q., Manga, M., 2005. Seismological constraints on a possible plume root at the core-mantle boundary. Nature 435, 666–669. https://doi.org/10.1038/nature03620

Roult, G., Roch, J., Clévédé, E., 2010. Observation of split modes from the 26th December 2004 Sumatra-Andaman mega-event. Phys. Earth Planet. Inter. 179, 45–59. https://doi.org/10.1016/j.pepi.2010.01.001

Rudolph, M.L., Lekić, V., Lithgow-Bertelloni, C., 2015. Viscosity jump in Earth's mid-mantle. Science (80-.). 350, 1349–1352. https://doi.org/10.1126/science.aad1929

Sakamaki, T., Ohtani, E., Fukui, H., Kamada, S., Takahashi, S., Sakairi, T., Takahata, A., Sakai, T., Tsutsui, S., Ishikawa, D., et al., 2016. Constraints on Earth's inner core composition inferred from measurements of the sound velocity of hcp-iron in extreme conditions. Sci. Adv. 2, e1500802. https://doi.org/10.1126/sciadv.1500802

Shearer, P.M., Rychert, C.A., Liu, Q., 2011. On the visibility of the inner-core shear wave phase PKJKP at long periods. Geophys. J. Int. 185, 1379–1383. https://doi.org/10.1111/j.1365-246x.2011.05011.x

Shen, Z., Ai, Y., He, Y., Jiang, M., 2016. Using pre-critical PKiKP--PcP phases to constrain the regional structures of the inner core boundary beneath East Asia. Phys. Earth Planet. Inter. 252, 37–48. https://doi.org/10.1016/j.pepi.2016.01.001

Simmons, N.A., Forte, A.M., Boschi, L., Grand, S.P., 2010. GyPSuM: A joint tomographic model of mantle density and seismic wave speeds. J. Geophys. Res. Solid Earth 115. https://doi.org/10.1029/2010JB007631

Souriau, A., Poupinet, G., 1991. A study of the outermost liquid core using differential travel times of the SKS, SKKS and S3KS phases. Phys. Earth Planet. Inter. 68, 183–199.

https://doi.org/10.1016/0031-9201(91)90017-C

Su, W., Dziewonski, A.M., 1997. Simultaneous inversion for 3-D variations in shear and bulk velocity in the mantle. Phys. Earth Planet. Inter. 100, 135–156.

Su, W.J., Dziewonski, A.M., 1997. Simultaneous inversion for 3-D variations in shear and bulk velocity in the mantle. Phys. Earth Planet. Inter. 100, 135–156. https://doi.org/10.1016/S0031-9201(96)03236-0

Tagawa, S., Ohta, K., Hirose, K., Kato, C., Ohishi, Y., 2016. Compression of Fe-Si-H alloys to core pressures. Geophys. Res. Lett. 43, 3686–3692. https://doi.org/10.1002/2016gl068848

Tanaka, S., 2007. Possibility of a low P-wave velocity layer in the outermost core from global SmKS waveforms. Earth Planet. Sci. Lett. 259, 486–499. https://doi.org/10.1016/j.epsl.2007.05.007

Tanaka, S., Hamaguchi, H., 1993a. Travel times and velocities in the outer core based on the global observation of SmKS seismic phases. Sci. reports Tohoku Univ. Fifth Ser. Tohoku Geophys. J. 34, 55–87.

Tanaka, S., Hamaguchi, H., 1993b. Velocities and Chemical Stratification in the Outermost Core. J. Geomagn. Geoelectr. 45, 1287–1301. https://doi.org/10.5636/jgg.45.1287

Tang, V., Zhao, L., Hung, S.H., 2015. Seismological evidence for a non-monotonic velocity gradient in the topmost outer core. Sci. Rep. 5, 1–5. https://doi.org/10.1038/srep08613

Thorne, M.S., Garnero, E.J., Grand, S.P., 2004. Geographic correlation between hot spots and deep mantle lateral shear-wave velocity gradients. Phys. Earth Planet. Inter. 146, 47–63. https://doi.org/10.1016/j.pepi.2003.09.026

Tkalčić, H., Kennett, B.L.N., Cormier, V.F., 2009. On the inner-outer core density contrast from PKiKP/PcP amplitude ratios and uncertainties caused by seismic noise. Geophys. J. Int. 179, 425–443. https://doi.org/10.1111/j.1365-246x.2009.04294.x

Tkalčić, H., Pham, T.S., 2018. Shear properties of Earth's inner core constrained by a detection of J waves in global correlation wavefield. Science (80-.). 362, 329–332. https://doi.org/10.1126/science.aau7649

To, A., Romanowicz, B., Capdeville, Y., Takeuchi, N., 2005. 3D effects of sharp boundaries at the borders of the African and Pacific Superplumes: Observation and modeling. Earth Planet. Sci. Lett. 233, 137–153. https://doi.org/10.1016/j.epsl.2005.01.037

Torsvik, T.H., Smethurst, M.A., Burke, K., Steinberger, B., 2006. Large igneous provinces generated from the margins of the large low-velocity provinces in the deep mantle. Geophys. J. Int. 167, 1447–1460. https://doi.org/10.1111/j.1365-246X.2006.03158.x

Trampert, J., Deschamps, F., Resovsky, J., Yuen, D., 2004a. Probabilistic tomography maps chemical heterogeneities throughout the lower mantle. Science (80-.). 306, 853–856. https://doi.org/10.1126/science.1101996

Trampert, J., Deschamps, F., Resovsky, J., Yuen, D., 2004b. Probabilistic tomography maps chemical heterogeneities throughout the lower mantle. Science (80-.). 306, 853–856. https://doi.org/10.1126/science.1101996

USGS, 2013. Sea of Okhotsk source mechanism [WWW Document]. URL

https://earthquake.usgs.gov/earthquakes/eventpage/usb000h4jh/moment-tensor?source=us&code=usb000h4jh_Mww (accessed 8.31.20).

van Tent, R., Deuss, A., Kaneshima, S., Thomas, C., 2020. The signal of outermost-core stratification in body-wave and normal-mode data. Geophys. J. Int. https://doi.org/10.1093/gji/ggaa368

Vočadlo, L., 2007. Ab initio calculations of the elasticity of iron and iron alloys at inner core conditions: Evidence for a partially molten inner core? Earth Planet. Sci. Lett. 254, 227–232. https://doi.org/10.1016/j.epsl.2006.09.046

Wang, Y., Wen, L., 2007. Geometry and P and S velocity structure of the "African Anomaly." J. Geophys. Res. 112, B05313. https://doi.org/10.1029/2006JB004483

Wang, Y., Wen, L., 2004. Mapping the geometry and geographic distribution of a very low velocity province at the base of the Earth's mantle. J. Geophys. Res. Solid Earth 109. https://doi.org/10.1029/2003JB002674

Waszek, L., Deuss, A., 2015. Anomalously strong observations of PKiKP /PcP amplitude ratios on a global scale. J. Geophys. Res. Solid Earth 120, 5175–5190. https://doi.org/10.1002/2015jb012038

Whaler, K.A., 1980. Does the whole of the earth's core convect? Nature 287, 528–530. https://doi.org/10.1038/287528a0

Widmer-Schnidrig, R., Laske, G., 2007. Theory and Observations – Normal Modes and Surface Wave Measurements, in: Schubert, G. (Ed.), Treatise on Geophysics. Elsevier B.V., pp. 67–125.

Widmer, R., Masters, G., Gilbert, F., 1991. Spherically symmetric attenuation within the Earth from normal mode data. Geophys. J. Int. https://doi.org/10.1111/j.1365-246X.1991.tb05700.x

Williams, C.D., Mukhopadhyay, S., Rudolph, M.L., Romanowicz, B., 2019. Primitive Helium Is Sourced From Seismically Slow Regions in the Lowermost Mantle. Geochemistry, Geophys. Geosystems 20, 4130–4145. https://doi.org/10.1029/2019GC008437

Woodhouse, J., Giardini, D., 1985. Inversion for the splitting functions of isolated normal mode multiplets. Eos (Washington. DC). 66, 301–301.

Woodhouse, J.H., 1998. The calculation of eigenfrequencies and eigenfunctions of the free oscillations of the Earth and the Sun. Seismol. Algorithms 321–370.

Woodhouse, J.H., Giardini, D., Li, X.-D., 1986. Evidence for inner core anisotropy from free oscillations. Geophys. Res. Lett. 13, 1549–1552. https://doi.org/10.1029/gl013i013p01549

Wookey, J., Helffrich, G., 2008. Inner-core shear-wave anisotropy and texture from an observation of PKJKP waves. Nature 454, 873–876. https://doi.org/10.1038/nature07131

Wu, W., Irving, J.C.E., 2020. Array-Based Iterative Measurements of Travel Times and Their Constraints on Outermost Core Structure. J. Geophys. Res. Solid Earth 125. https://doi.org/10.1029/2019JB018162

Yang, H.-Y., Tromp, J., 2015. Synthetic free-oscillation spectra: an appraisal of various mode-coupling methods. Geophys. J. Int. https://doi.org/10.1093/gji/ggv349

Yu, S., Garnero, E.J., 2018. Ultralow Velocity Zone Locations: A Global Assessment. Geochemistry, Geophys. Geosystems 19, 396–414. https://doi.org/10.1002/2017GC007281

Yu, S., Garnero, E.J., Shim, S.-H., Li, M., Tyburczy, J.A., Till, C.B., 2020. Extreme Seismic Anomalies near Earth's Core Mantle Boundary.

Yuan, L., Chao, B.F., Ding, X., Zhong, P., 2013. The tidal displacement field at Earth's surface determined using global GPS observations. J. Geophys. Res. Solid Earth 118, 2618–2632. https://doi.org/10.1002/jgrb.50159

Zhong, S., Rudolph, M.L., 2015. On the temporal evolution of long-wavelength mantle structure of the Earth since the early Paleozoic. Geochemistry, Geophys. Geosystems 16, 1599–1615. https://doi.org/10.1002/2015GC005782

Appendix

Part A

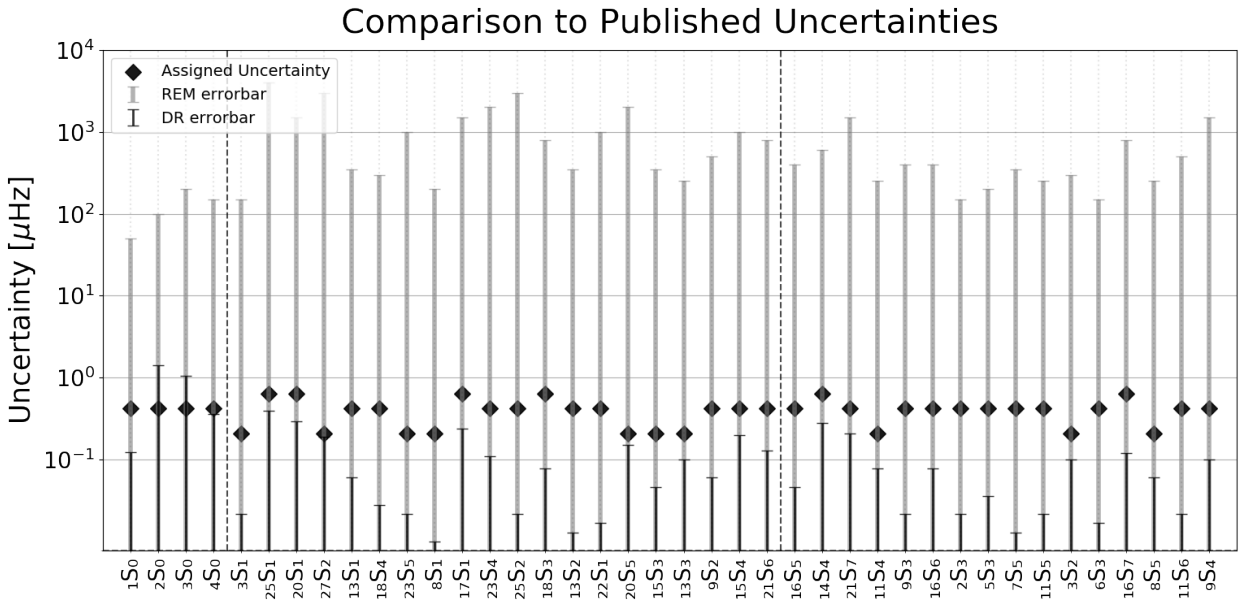

Figure A1: **Comparison of assigned 'uncertainties' to those published with the datasets** presented in logarithmic scale. Assigned uncertainties are predominantly greater than those of DR by roughly one order of magnitude but significantly smaller than those of the earlier REM catalog.

Part B

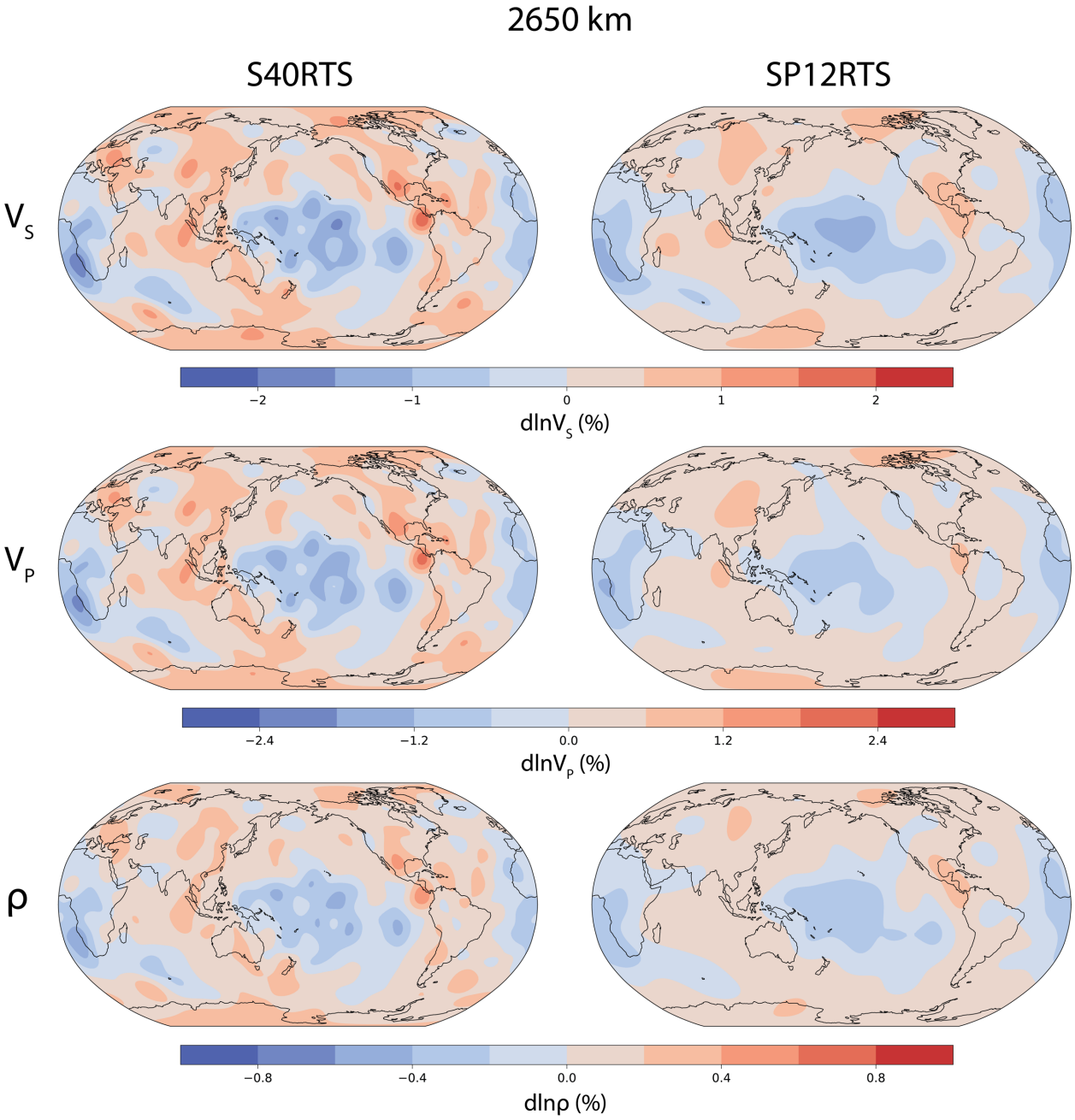

Figure B1 | Structure maps of both mantle models at 2650km depth relative perturbations (%) of each of the major parameters, V_s (top), V_p (middle), and density (bottom) of each model are shown with SP12RTS (right) and S40RTS (left) plotted on the same color scale for each parameter.

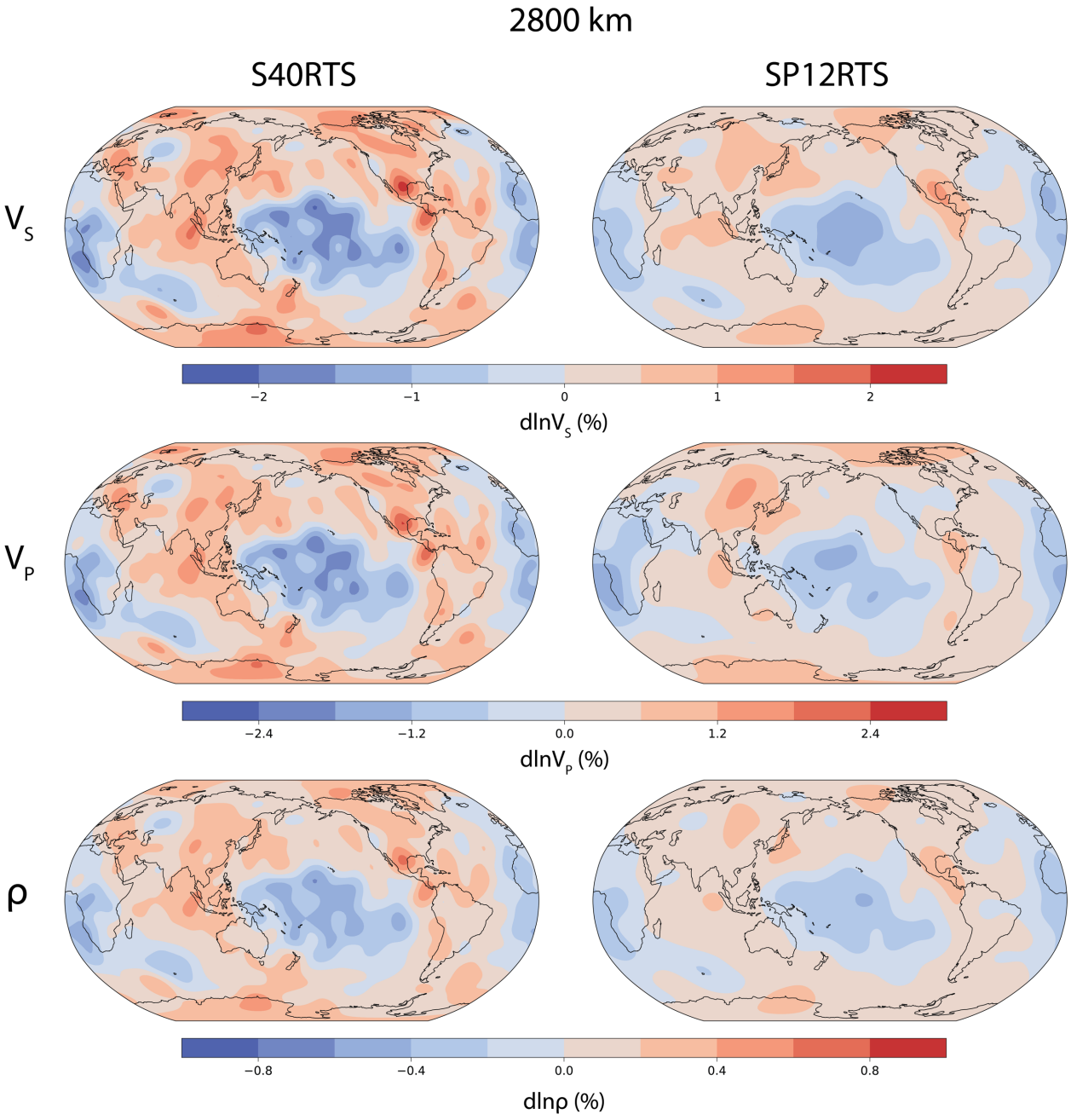

Figure B2 | Structure maps of both mantle models at 2800km depth relative perturbations (%) of each of the major parameters, V_s (top), V_p (middle), and density (bottom) of each model are shown with SP12RTS (right) and S40RTS (left) plotted on the same color scale for each parameter.

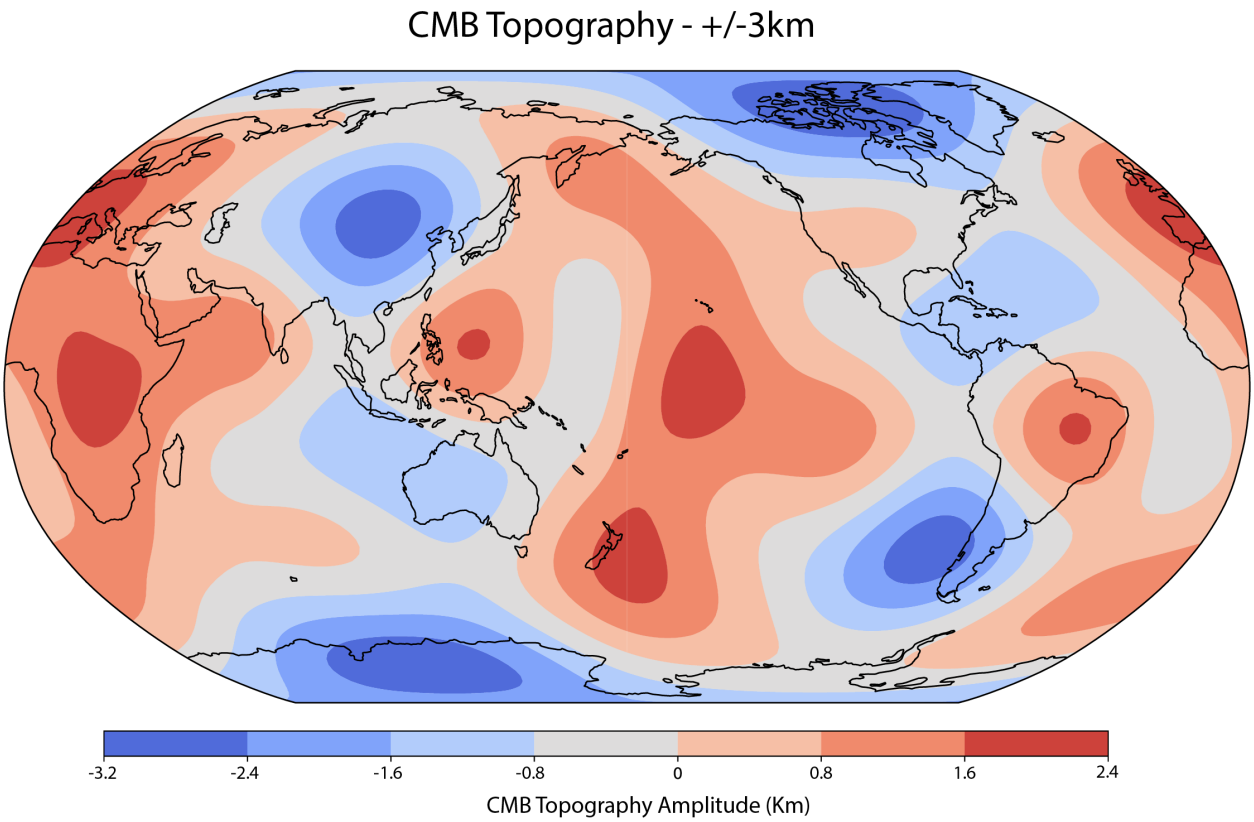

Figure B3 | **CMB topography model** linearly scaled from density at the base of S40RTS (Ritsema et al., 2011) at spherical harmonic degree 6, such the maximum amplitude of topography (positive or negative) is 3km. It can be seen that there is upwelling imposed under the LLSVPs which are assumed buoyant due to their reduced V_s.

	Half-duration [s]	Lat	Lon	Depth [km]	Mrr	Mtt	Mpp	Mrt	Mrp	Mtp
CMT	35.7	54.89	153.22	598.1	-1.67E+28	3.82E+27	1.28E+28	-7.84E+27	-3.57E+28	1.55E+27
USGS	35.7	54.89	153.22	598.1	-1.40E+28	3.10E+27	1.08E+28	-7.90E+27	-3.54E+28	8.00E+26
E35	16	54.89	153.22	640	-1.29E+28	4.10E+27	8.70E+27	-1.13E+28	-3.77E+28	6.00E+26

Table B1 | **Source solution parameters** for each of the three source solutions explored: the Harvard CMT reference solution (Ekström et al., 2012), the United States Geological Survey (USGS) solution (USGS, 2013), and solution E35 from Abubakirov et al., (2015)**.**

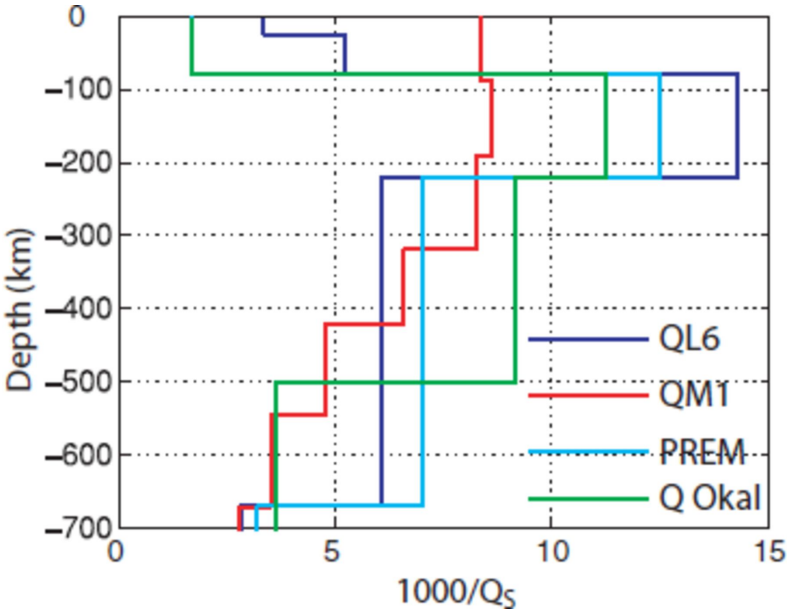

Figure B4: **Radial attenuation models in the upper mantle** Seismic attenuation 1-D profiles for the upper mantle. QL6 (Durek & Ekström 1996), QM1 (Widmer et al. 1991), PREM (Dziewonski & Anderson 1981) and Q Okal (Okal and Jo, 1990). Figure taken after Cammarano and Romanowicz (2008).

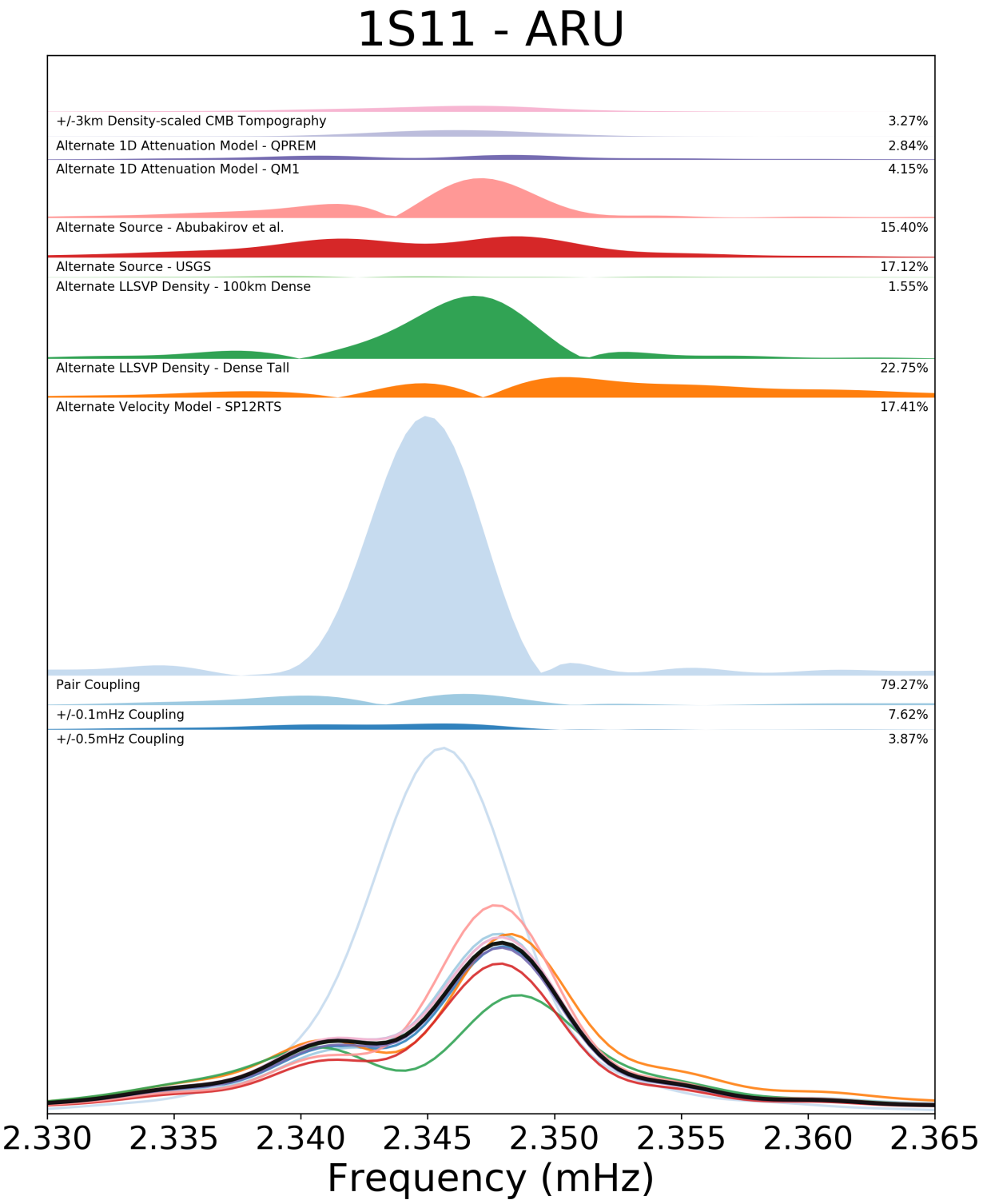

Figure B5 | ARU example C Stoneley mode spectra and residuals a comparison of test cases to the full-coupling ground truth (black line) for ${}_1S_{11}$ at station ARU, Arti, Russia. Other synthetics are shown, while absolute values of the residual between each test and the ground truth are shown filled, with label and a percentage describing the integral under the absolute residual relative to that of the ground truth.

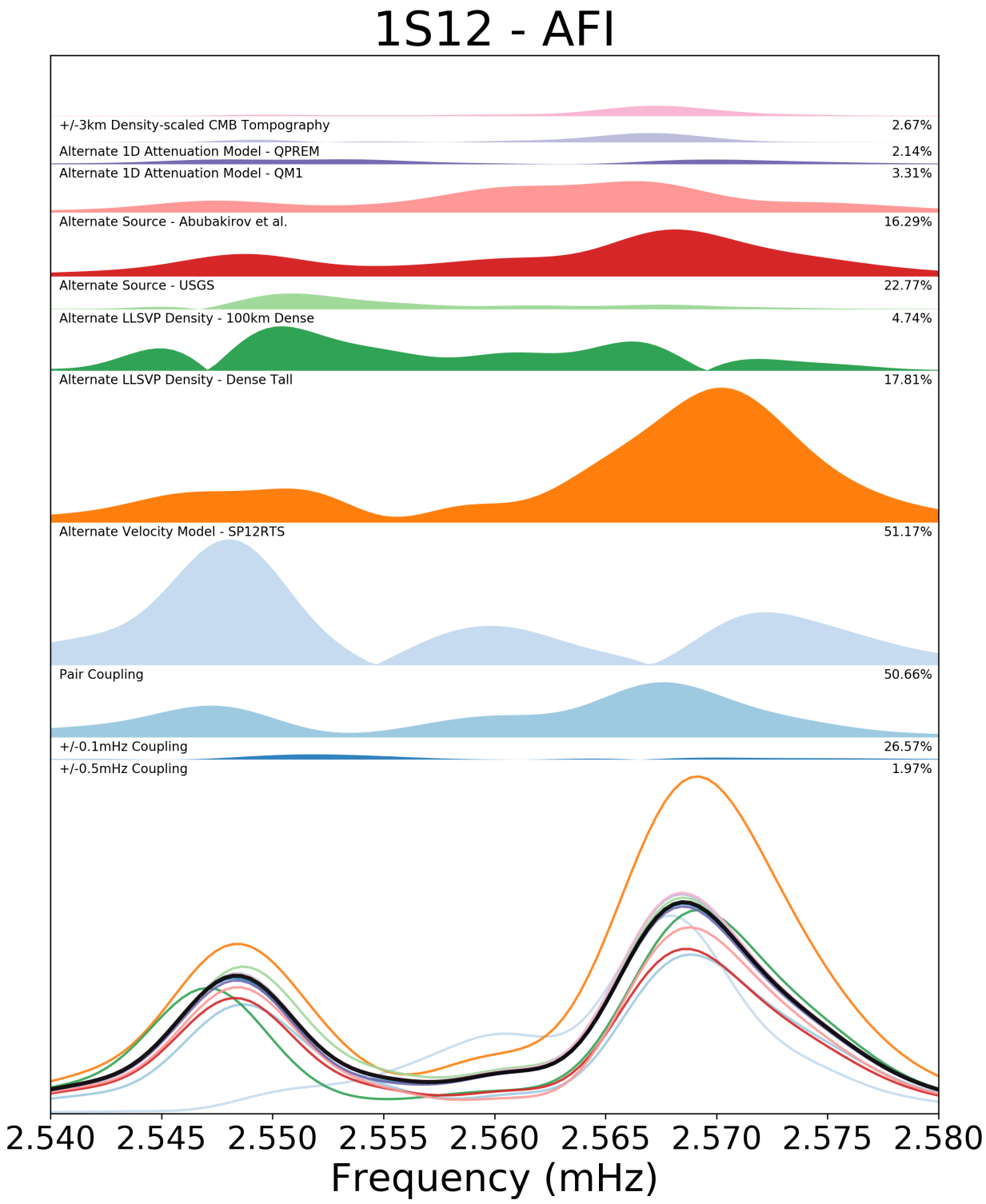

Figure B6 | AFI example Stoneley mode spectra and residuals a comparison of test cases to the full-coupling ground truth (black line) for ${}_1S_{11}$ at station AFI, Afiamalu, Samoa. Other synthetics are shown, while absolute values of the residual between each test and the ground truth are shown filled, with label and a percentage describing the integral under the absolute residual relative to that of the ground truth.

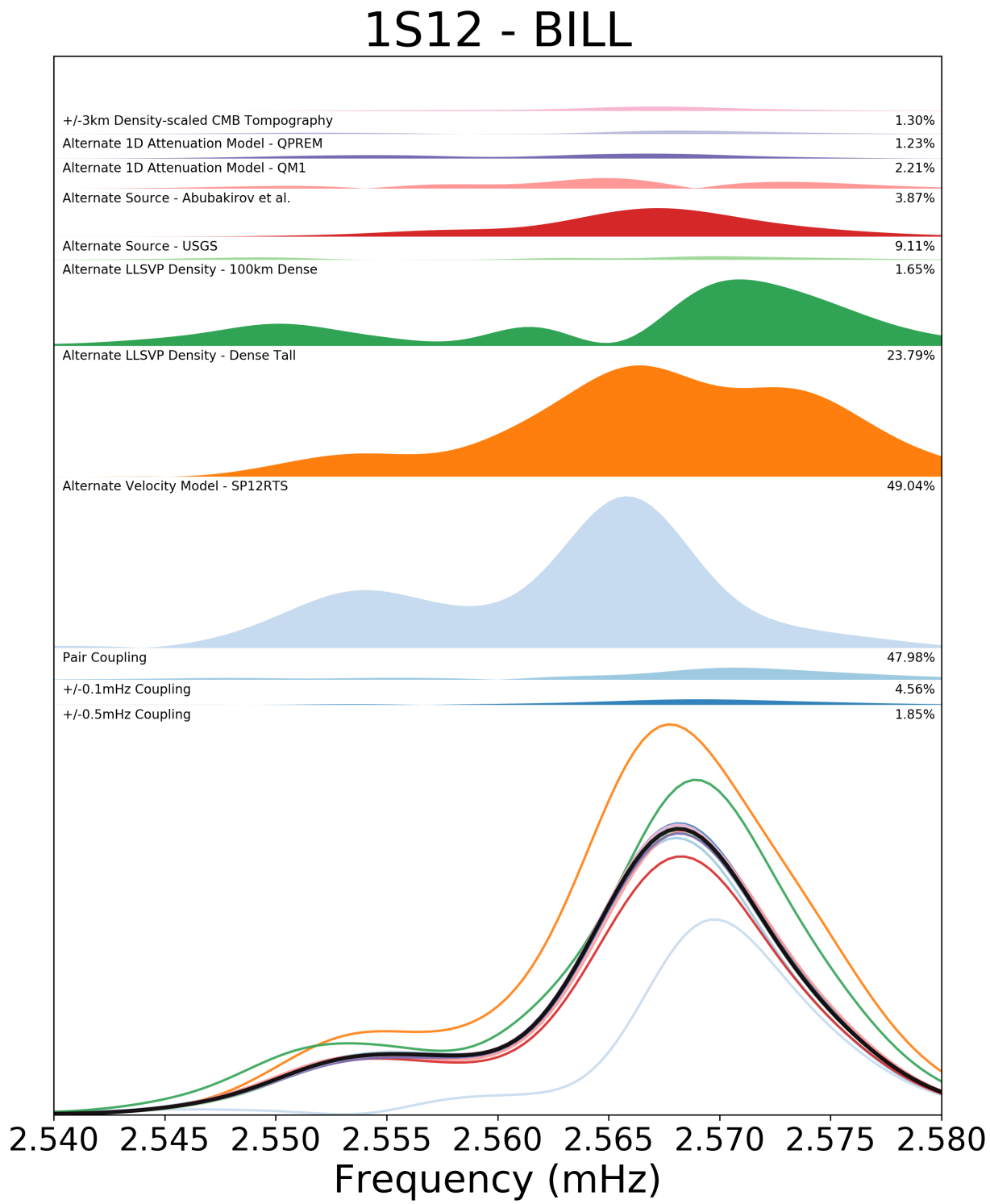

Figure B7 | BILL example Stoneley mode spectra and residuals a comparison of test cases to the full-coupling ground truth (black line) for ${}_1S_{12}$ at station BILL, Bilibino, Russia. Other synthetics are shown, while absolute values of the residual between each test and the ground truth are shown filled, with label and a percentage describing the integral under the absolute residual relative to that of the ground truth.

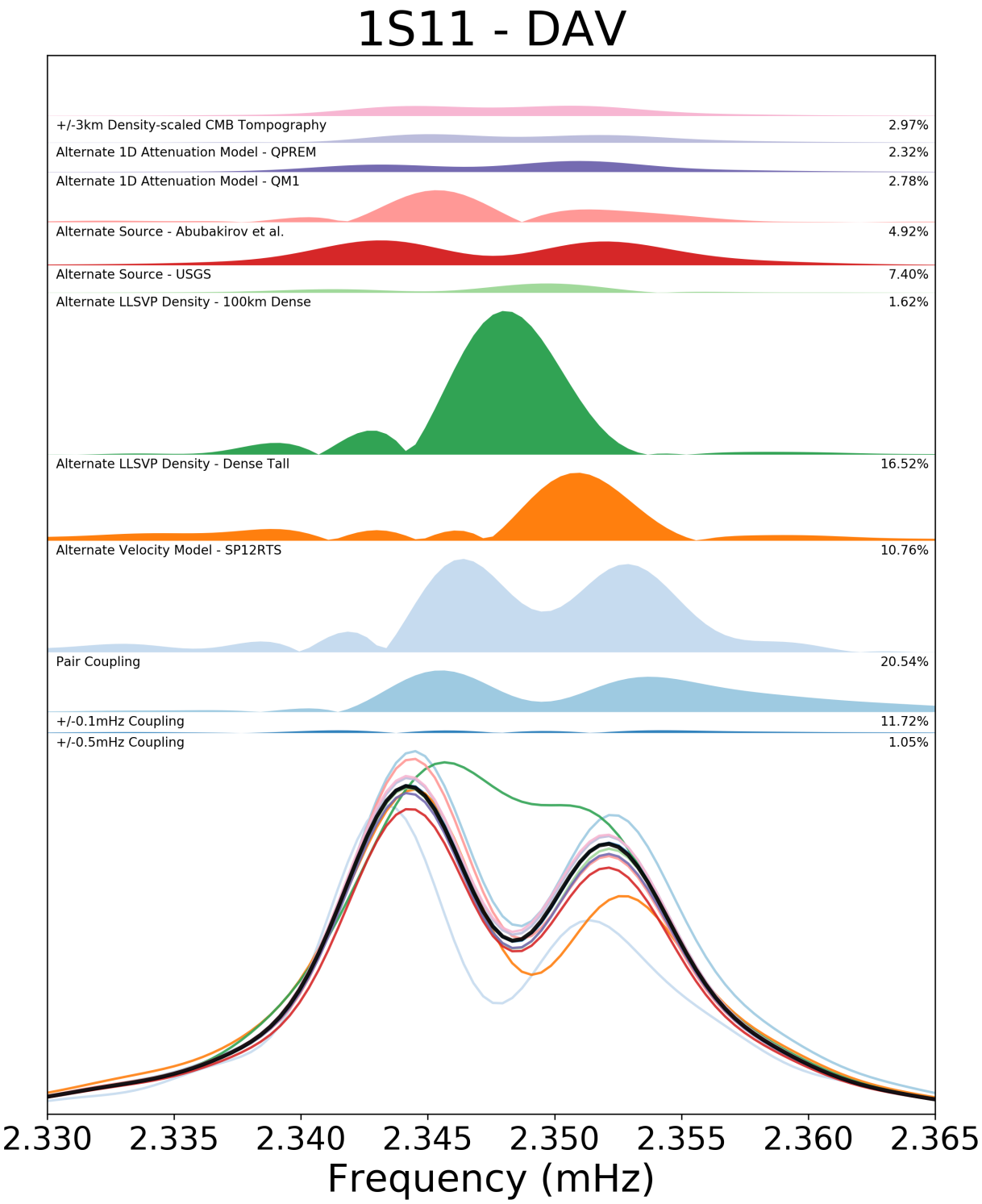

Figure B8 | DAV example Stoneley mode spectra and residuals a comparison of test cases to the full-coupling ground truth (black line) for ${}_1S_{11}$ at station DAV, Davao, Philippines. Other synthetics are shown, while absolute values of the residual between each test and the ground truth are shown filled, with label and a percentage describing the integral under the absolute residual relative to that of the ground truth.

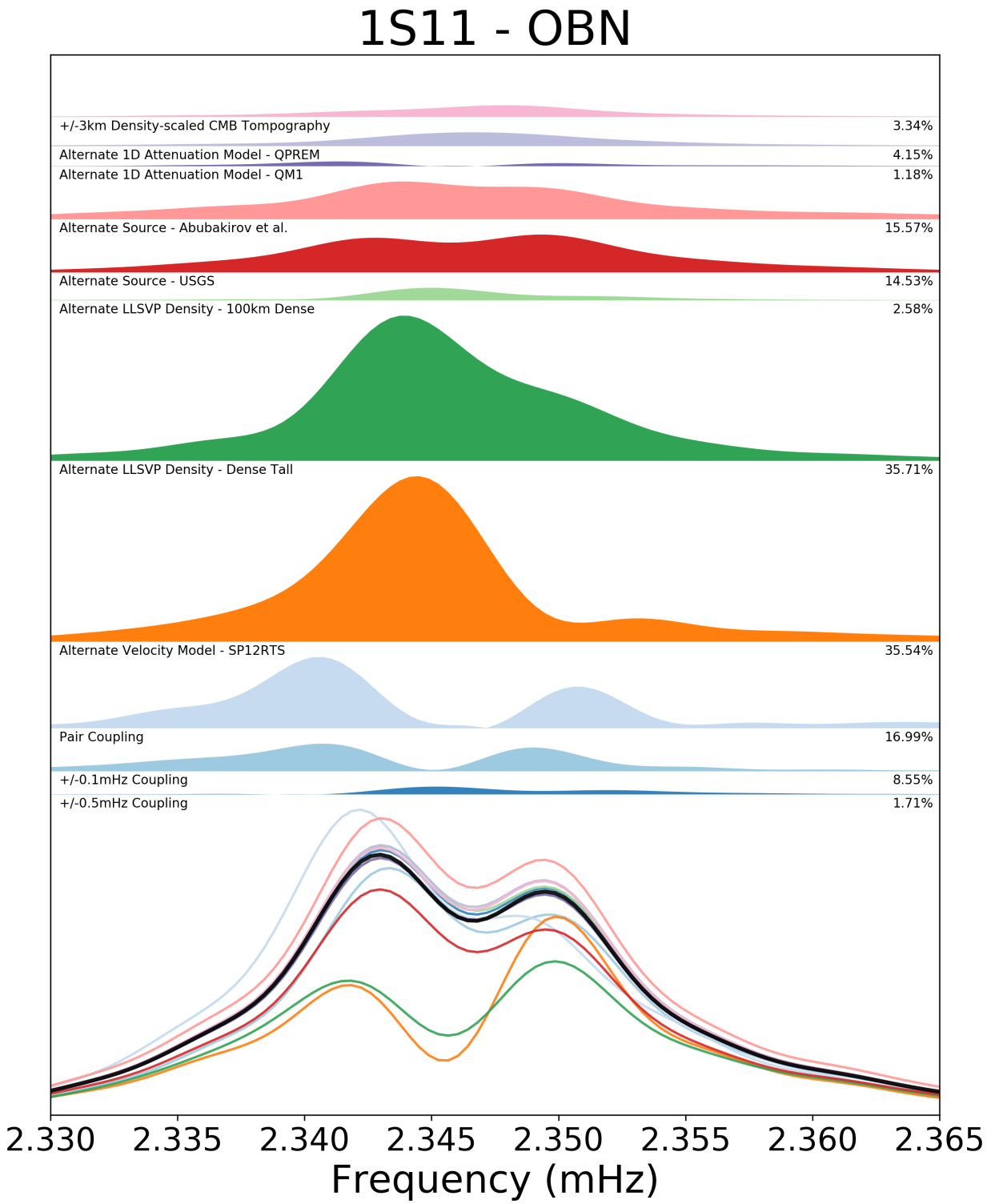

Figure B9 | OBN example Stoneley mode spectra and residuals a comparison of test cases to the full-coupling ground truth (black line) for ${}_1S_{11}$ at station OBN, Obninsk, Russia. Other synthetics are shown, while absolute values of the residual between each test and the ground truth are shown filled, with label and a percentage describing the integral under the absolute residual relative to that of the ground truth.

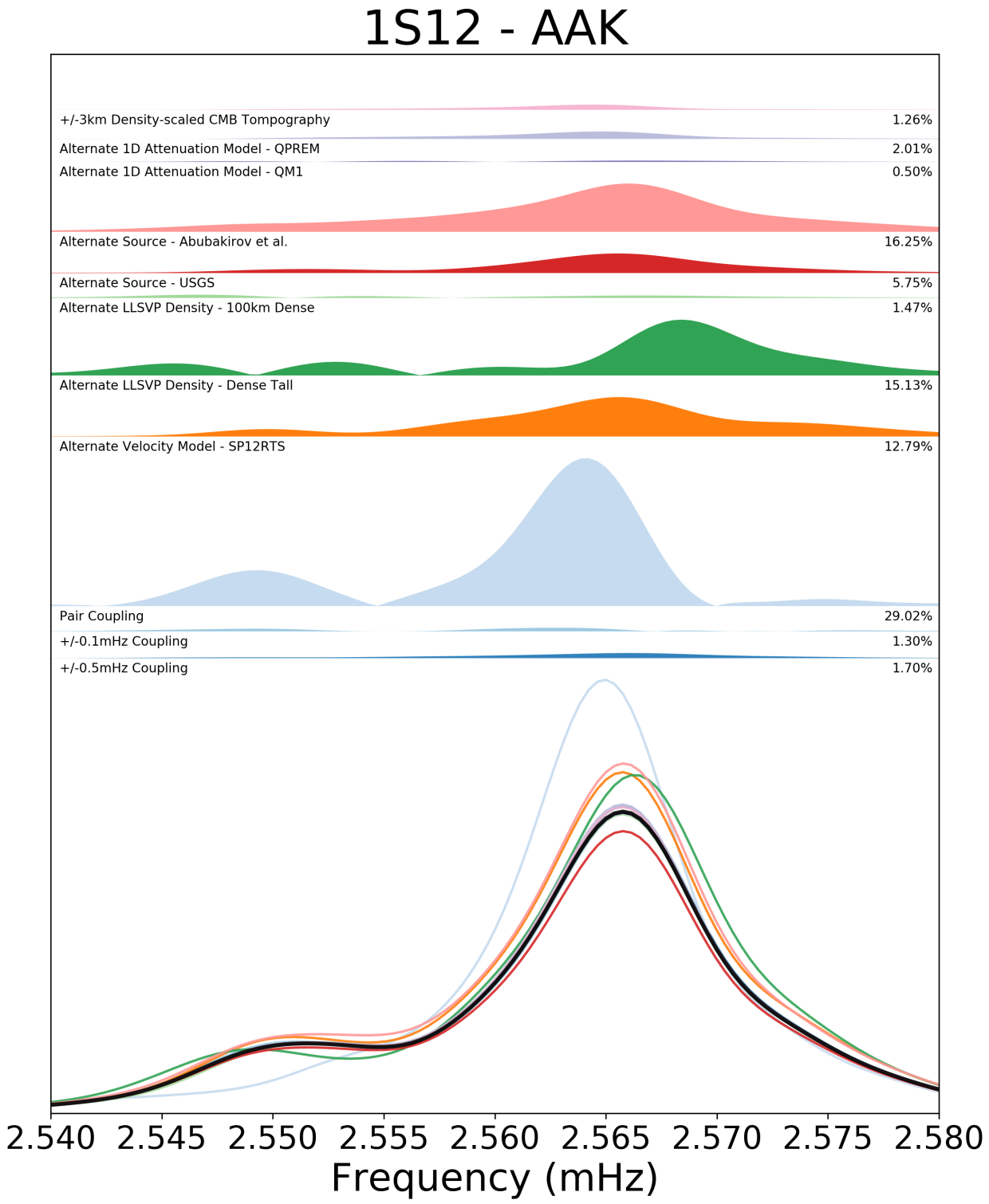

Figure B10 | AAK example Stoneley mode spectra and residuals a comparison of test cases to the full-coupling ground truth (black line) for ${}_1S_{12}$ at station AAK, Ala Archa, Kyrgyzstan. Other synthetics are shown, while absolute values of the residual between each test and the ground truth are shown filled, with label and a percentage describing the integral under the absolute residual relative to that of the ground truth.

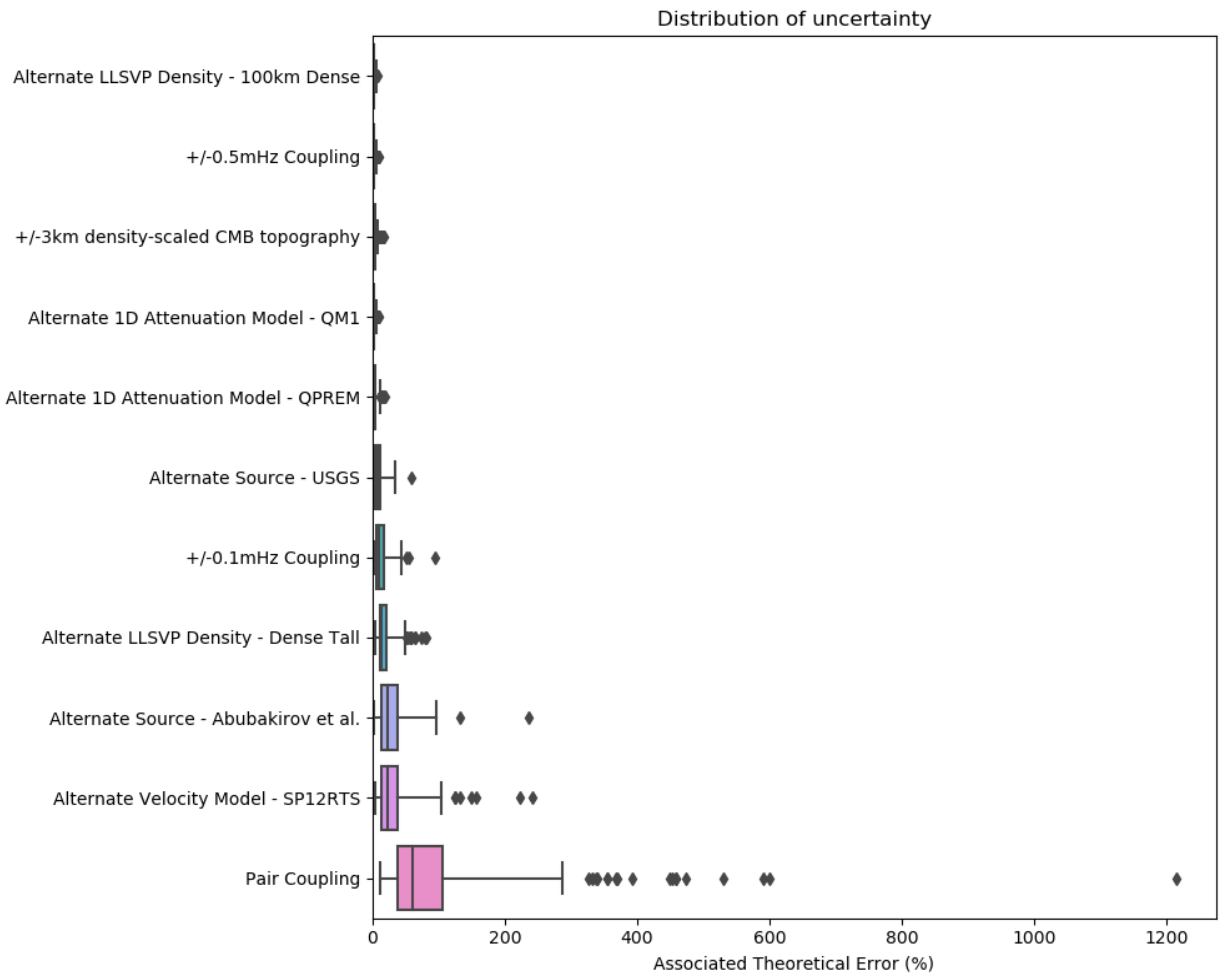

Figure B11 | Box and whisker diagram of the distribution residuals associated with each test case. Diamonds are outliers greater than five interquartile ranges from the median value.

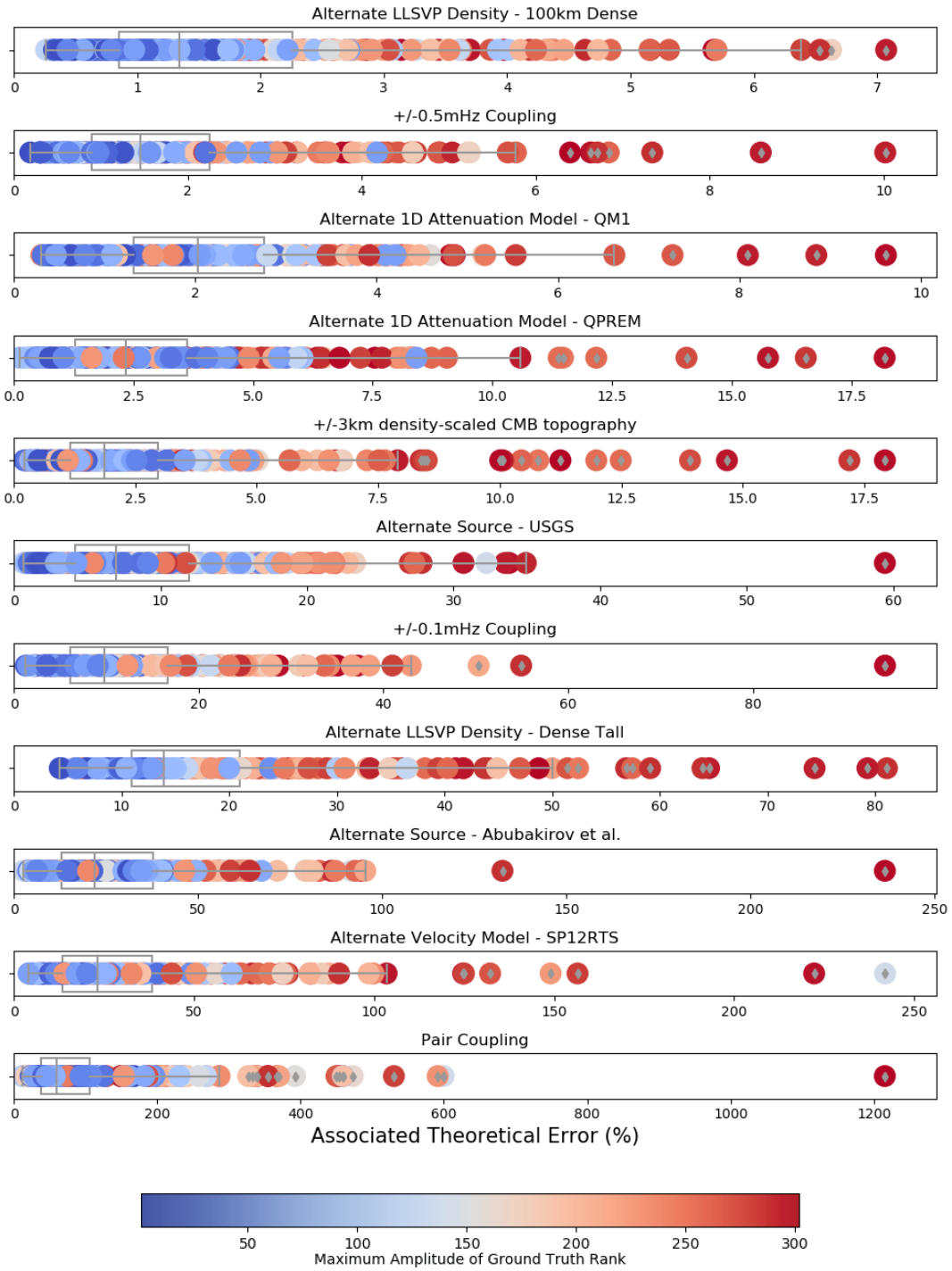

Figure B12 | **Individual residuals distributions** for each effect all station-mode pairs were ranked by the absolute amplitude of the reference spectra, their residual percentage plotted and colored by rank. It is easy to see that the outlier with very large residuals are commonly associated with the smallest amplitude observations. Note that x-axis scales differ.

Part C

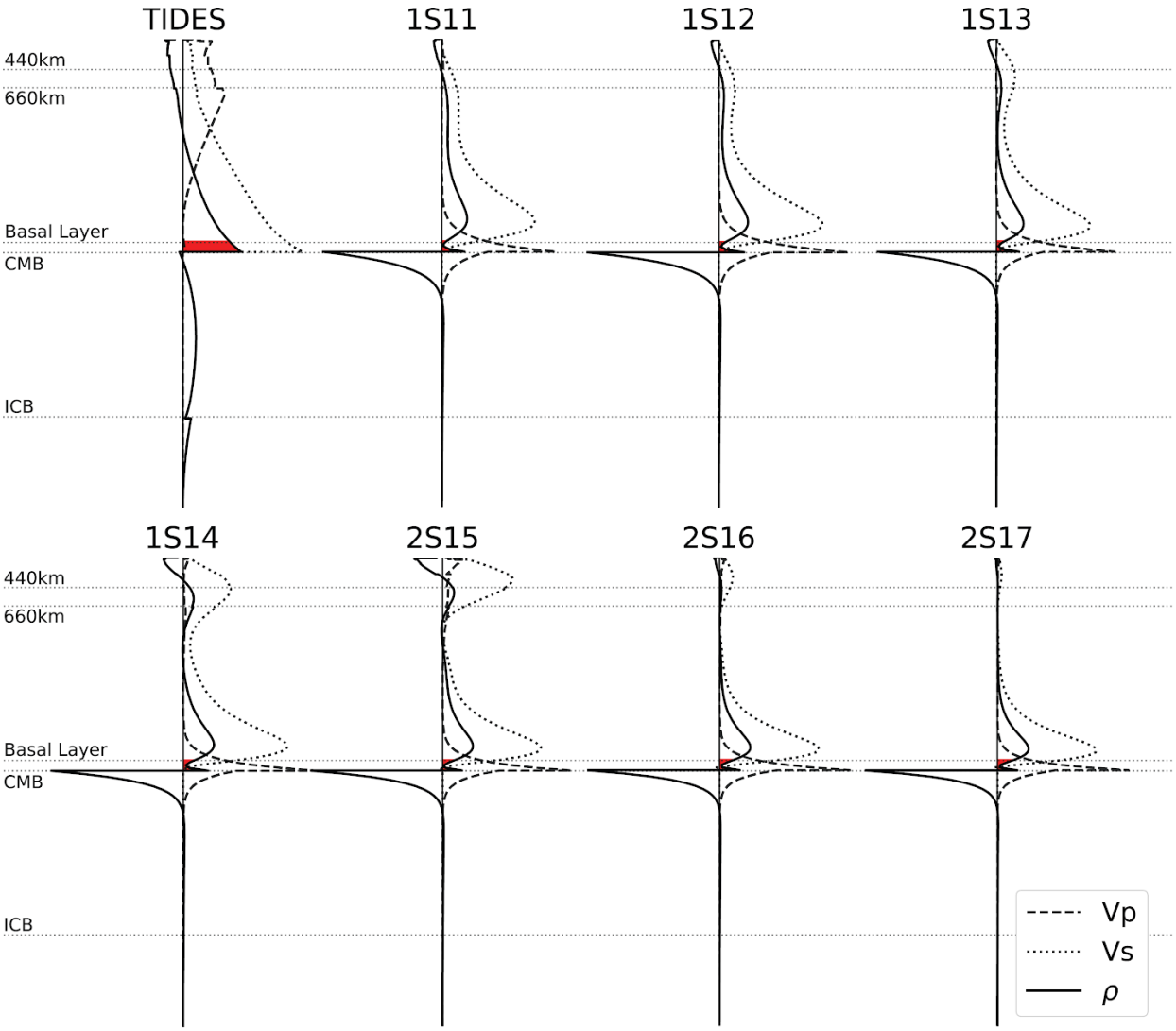

Figure C1 | Sensitivity Kernels Spherically symmetric sensitivity kernels for isotropic V_p, V_s, and density (ρ) as a function of depth, computed in the radially anisotropic Preliminary Reference Earth Model (PREM) (Dziewonski and Anderson, 1981) for the semi-diurnal tide (upper left) and for seven Stoneley modes (right and lower). Note the contrasting depth dependence of the sensitivity to density ρ of the body tide and the Stoneley modes. The red patches highlight the sensitivity to density in the lowermost 100km of the mantle. This sensitivity is very small in the case of the Stoneley modes.

				LLSVP Density Model			
Dataset	Metric	Degree	CMB Topo	L-LLSVP	D-LLSVP	DBL100km	DBL200km
Body Tides	Significance	<20	N	89.5%	96.4%	95.5%	95.7%
		<20	Y	90.0%	95.4%	95.1%	95.1%
Stoneley Mode spectra	mean S.S.D	<20	N	0.046759	0.045882	0.046898	0.046477
		<20	Y	0.046759	0.045876	0.046895	0.046476
Stoneley Mode Splitting Functions	Probability	2	N	0.25	0.17	0.17	0.20
		4	N	0.38	0.38	0.28	0.30
		6	N	0.30	0.24	0.31	0.32
		Avg	N	0.32	0.27	0.27	0.29
		2	Y	0.32	0.36	0.26	0.29
		4	Y	0.45	0.40	0.40	0.44
		6	Y	0.40	0.36	0.34	0.36
		Avg	Y	0.40	0.37	0.35	0.37

Table C1 | Model evaluation metrics Assessment of the ability of each model to explain body tide and splitting function observations are presented in the form of their original metric (L2017 and K2017), significance level and probability, respectively. Probabilities (close to 1 for a good fit; ~0.5 for best-fitting models in K2017) were calculated independently for spherical harmonic degrees 2, 4, and 6. The average presented here is a sum weighted by the number of splitting coefficients for each degree.

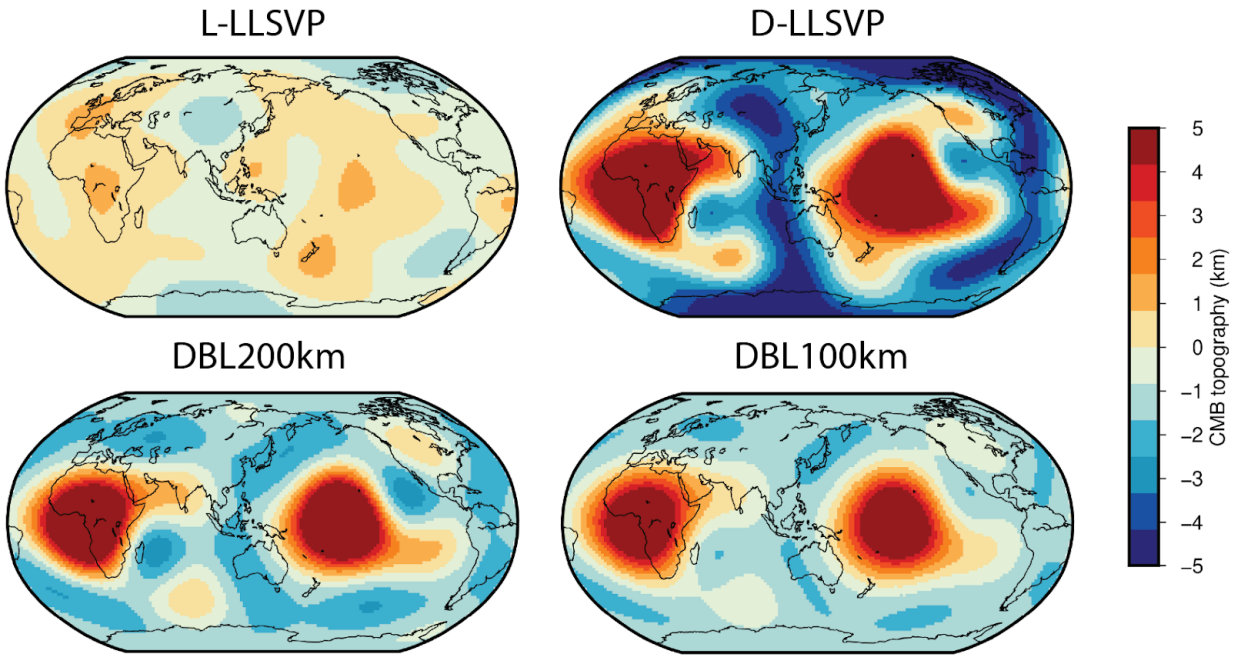

Figure C2 | Best-fitting CMB topography Best-fitting, scaled-to-density, CMB topography for each density model, resulting from a grid search performed separately for each structural degree (as in K2017), to match Stoneley mode splitting function observations. Note that in all cases the CMB topography is deflected upward below the LLSVPs. The amplitude of the CMB topography increases substantially for the D-LLSVP and DBL models compared to the L-LLSVP model.

Text C3 | Stoneley mode spectra data and processing

All seismograms available from Streckeisen STS-1 broadband seismometers for a period of 96 hours after the event were collected, individually inspected, and seismograms with glitches and/or excessive noise (Fig C4) were removed. The records from the remaining 55 stations were kept (Fig C5) and processed (Fig C6, Table C2) for comparison to synthetics.

To maximize the sensitivity of the spectral dataset, a data-tuning step was performed to remove station-mode pairs for which all four models poorly fit the observations (e.g. Fig C8). The resulting final spectra dataset consists of 170 observations.

The overall ability of each LLSVP density model to explain observed Stoneley mode spectra was assessed via the mean sum of squared difference (S.S.D.) between the predicted and observed amplitude spectra across all station-mode pairs.

$$Mean\ S.S.D. = \frac{1}{P}\frac{1}{N}\sum_{p=1}^{p=P}\sum_{i=1}^{i=N}\left(\frac{Y^{i}_{obs}}{Y_{max}} - \frac{Y^{i}_{syn}}{Y_{max}}\right)^2$$

Where N, is the total number of points within the frequency window, Y^i_{obs} is the amplitude of the ith point in the observed spectra, and Y^i_{syn} is the corresponding amplitude in the synthetics, while Y_{max} is the maximum observed spectral amplitude within the frequency window, and serves to normalize amplitudes between different stations. P is the total number of observations (170 in this case), and p is the index of the mode-station pair.

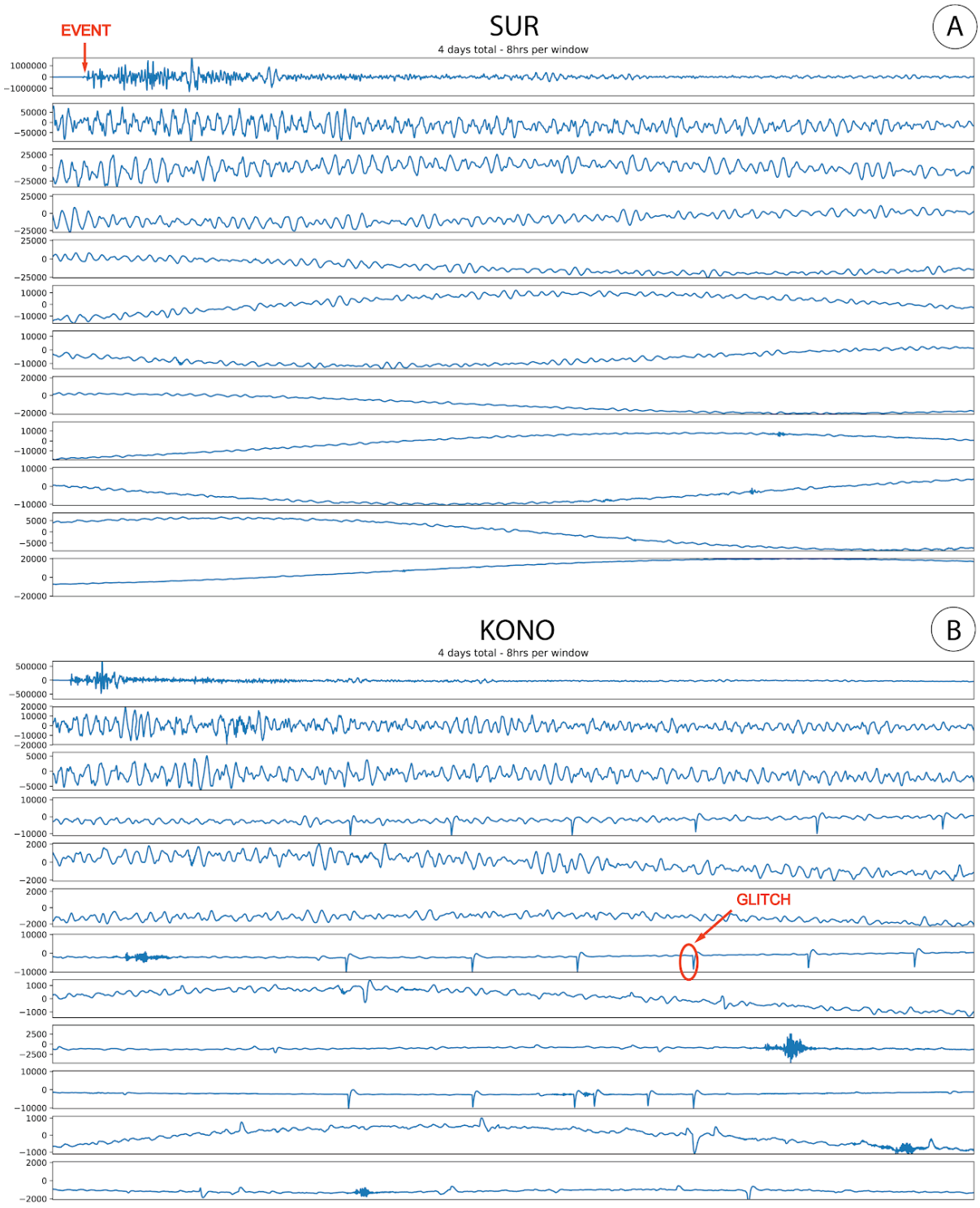

Figure C4 | Examples of raw data inspection for spectra 96h of raw unprocessed signal from the broadband STS-1 seismometers in Sutherland, South Africa (A) and Kongsberg, Norway (B). Each row is 8h and the event can be seen in the upper left. The upper panel (A) shows a trace that passed manual inspection, with low noise and no obvious glitches, while data from KONO (B) was discarded in the manual inspection step due to glitches.

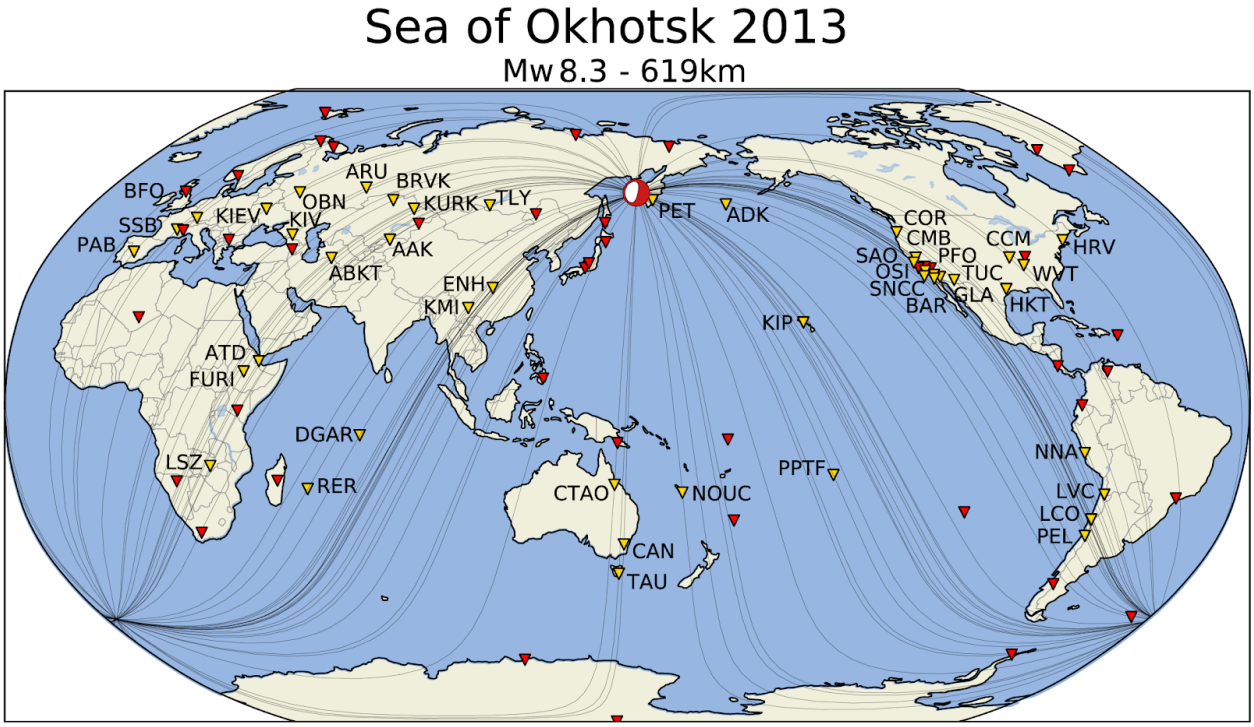

Figure C5 | Data map The distribution of all stations (yellow triangles) contained in the CMB Stoneley mode spectra dataset and their great circle paths (grey), alongside the location and mechanism of the Sea of Okhotsk 2013 deep earthquake (red and white beach ball). Red triangles are stations manually discarded due to noise and/or glitches

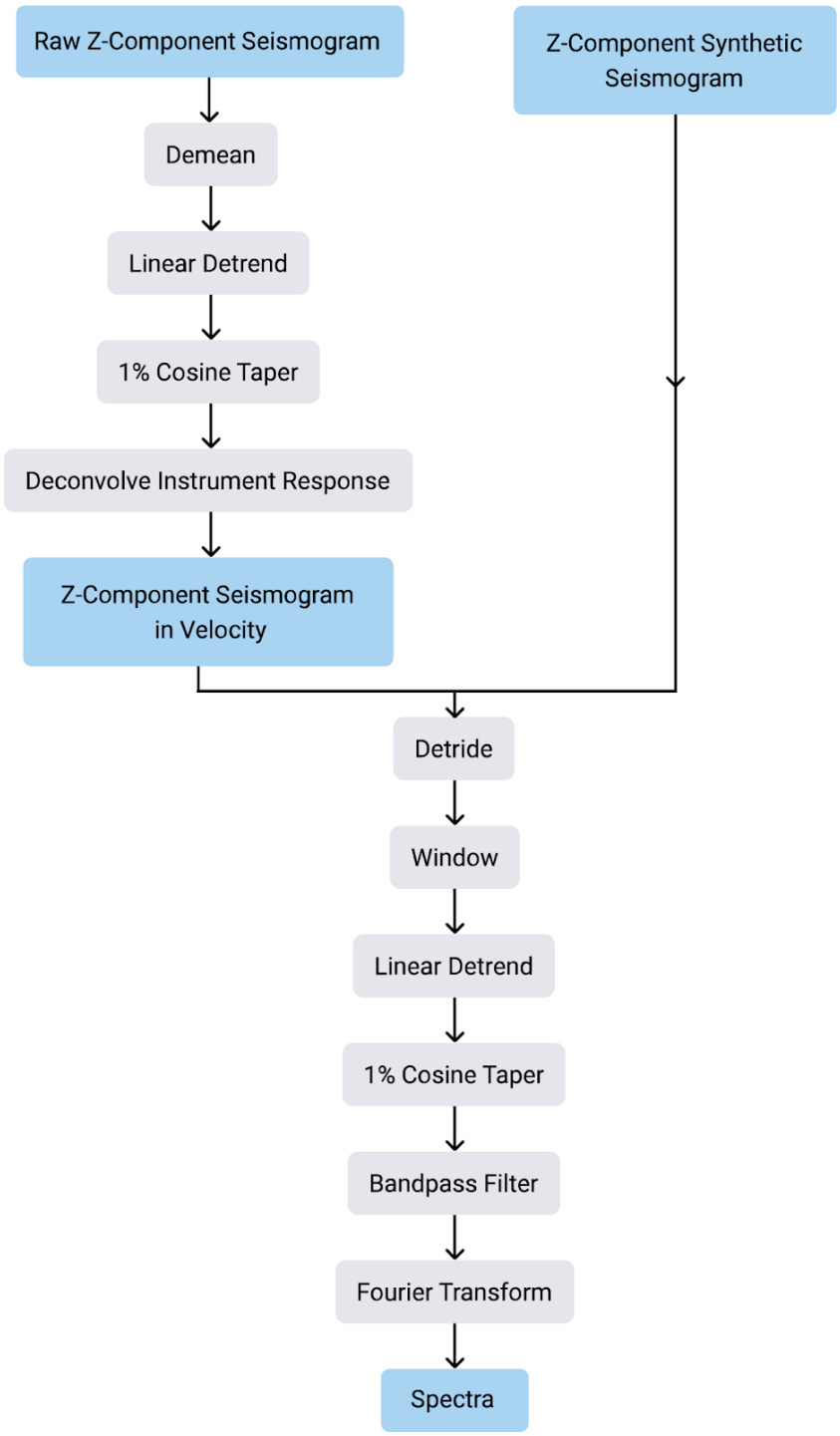

Figure C6 | Processing flowchart for spectra Data processing applied to the observed (left) and synthetic seismograms (right) to attain the spectra analyzed in this study. More detailed processing parameters can be found in Table C1.

Stoneley Mode	Observed Center Frequency (mHz)	Bandpass Filter (mHz)		Window (h after event)		no. observations after tuning
		Low Corner	High Corner	Start	Stop	
$_1S_{11}$	2.34565	2.330	2.365	20	70	27
$_1S_{12}$	2.55255	2.540	2.580	10	70	32
$_1S_{13}$	2.76432	2.750	2.800	5	65	34
$_1S_{14}$	2.97373	2.945	2.995	5	60	30
$_2S_{15}$	3.23869	3.235	3.255	5	65	16
$_2S_{16}$	3.44080	3.430	3.470	5	65	28
$_2S_{17}$	3.65623	3.645	3.675	10	70	13

Table C2 | Stoneley mode spectra filtering parameters Stoneley mode data table, showing the observed center frequency (Koelemeijer et al., 2013), frequency window, time window, and final number of observations associated with each Stoneley mode that remain from the original 55 stations.

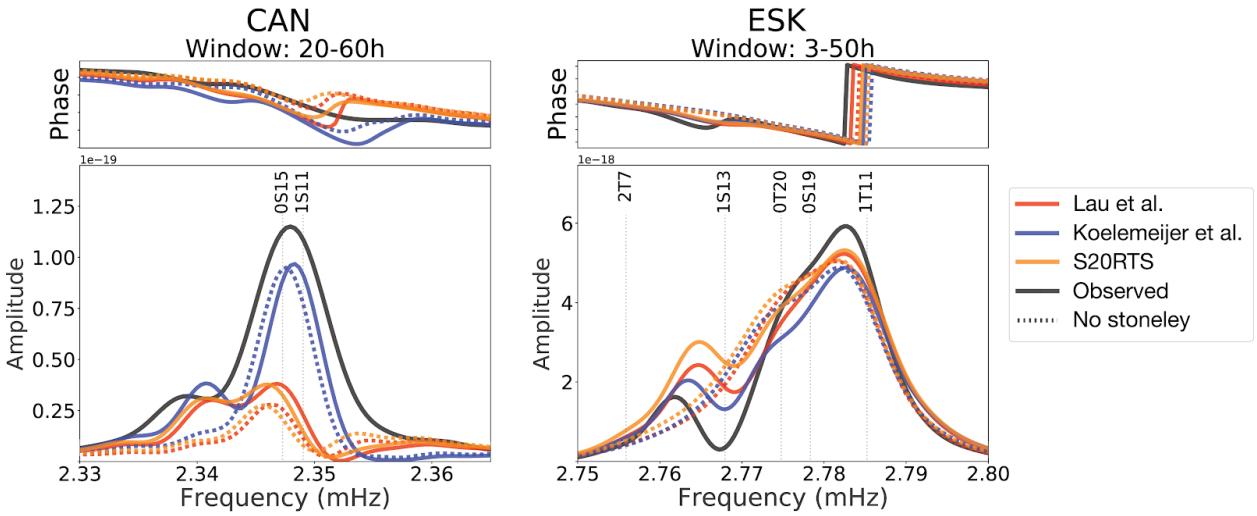

Figure C7 | Preliminary Stoneley mode test Stoneley modes $_1S_{11}$ and $_1S_{13}$ as seen in observed spectra (black) at stations CAN (Canberra, Australia) and ESK (Eskdalemuir, Scotland), respectively. Synthetic spectra generated using full-coupling (<3.1mHz) are shown for S20RTS and the preferred models of Lau et al. (2017) and Koelemeijer et al. (2017). A secondary peak to the left of the fundamental mode can be seen in both the data and all three synthetics when coupling with the Stoneley modes is included in the generation of synthetics (solid). Conversely, when all other modes are coupled but the Stoneley modes are not (dotted), this secondary peak, observed in the data, disappears from all synthetics.

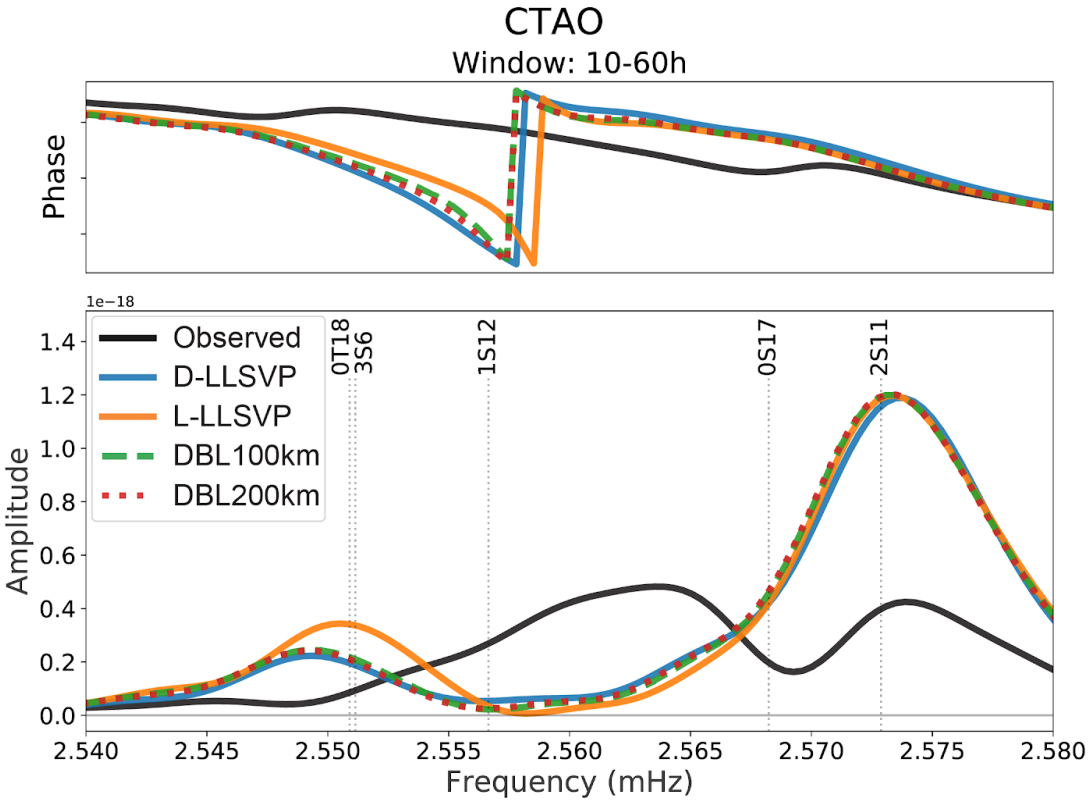

Figure C8 | Poorly fit data example An example for ${}_1S_{12}$ at station CTAO (Charters Towers, Australia), which despite passing manual inspection for glitches and noise, shows much larger differences between each model and the observed spectra than between the models themselves. As a result, this spectral window can only provide minimal constraints on LLSVP density structure, and so was removed from the data to be assessed, in a second step.

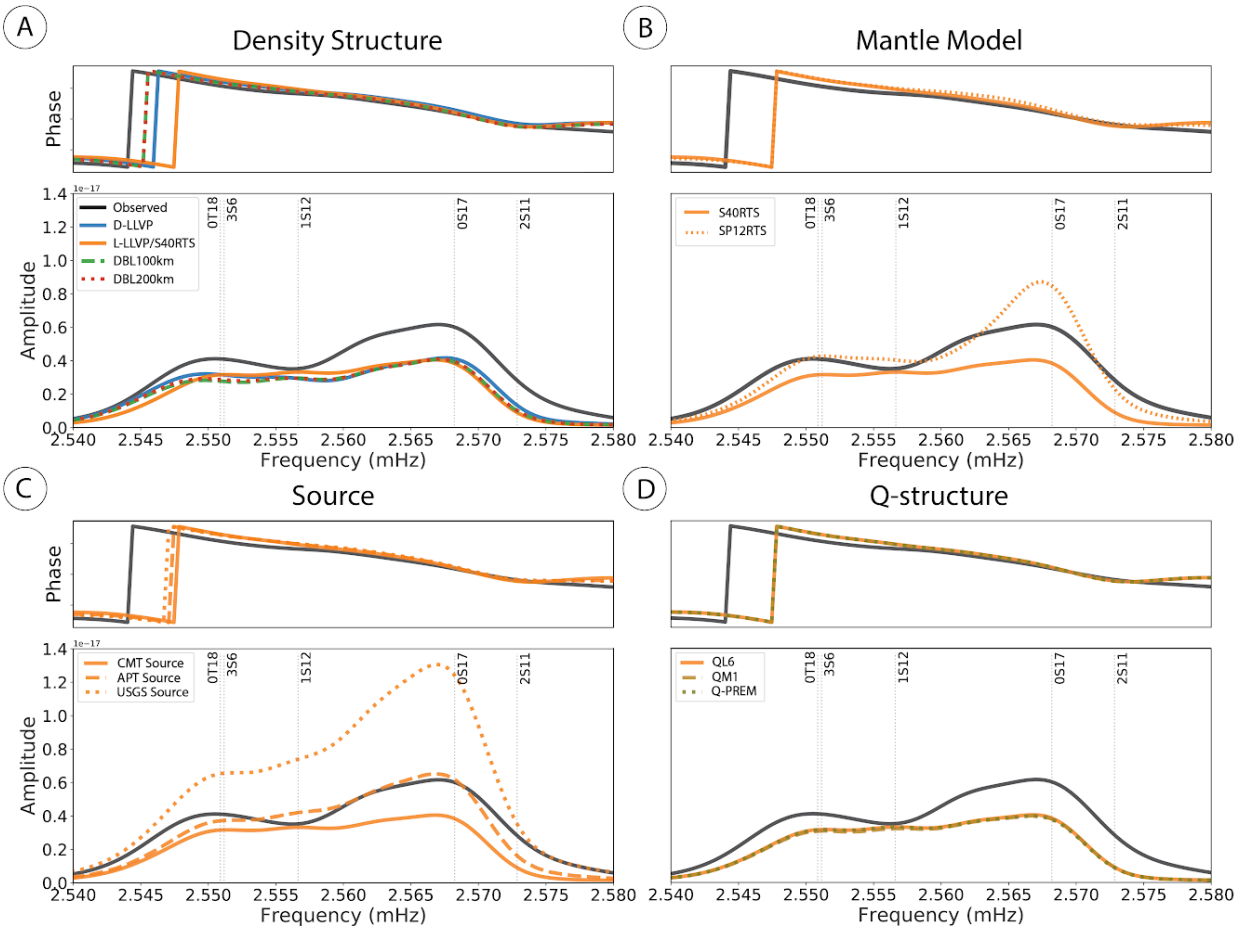

Figure C9 | Sources of uncertainty in the spectra A comparison of the relative magnitudes of different sources of uncertainty. (**a**) shows the ${}_1S_{12}$ frequency window at station BRVK (Borovoye, Kazakhstan); the synthetics for each model are shown alongside the data. The other three panels show the effect and resulting uncertainty in the spectra due to (**b**) changes in the mantle model, (**c**) earthquake source solution, and (**d**) the 1D Q-model used. (**b**) compares otherwise identical synthetics for mantle models S20RTS and SP12RTS (Koelemeijer et al., 2016). It can be seen that the magnitude of change in the synthetics is much greater than that due to the LLSVP density structure in (**a**). Panel (**c**) compares the effect of different source solutions including the Harvard CMT (CMT) (used for all other runs), the USGS preferred solution (USGS), and solution E35 from Abubakirov et al., (2015) (APT). Again, differences are larger than those seen due to LLSVP density structure in the top left panel. Panel (**d**) compares the effect of using different 1-D Q models showing spectra for QM1 (Widmer et al., 1991), PREM (Dziewonski and Anderson, 1981), and QL6 (Durek and Ekström, 1996) (used for all other runs), which have a negligible effect.